

THEORETICAL INVESTIGATIONS OF MAGNETIC PROPERTIES OF MRI CONTRAST AGENTS AND CARBON NANOSTRUCTURES

THÈSE N° 3771 (2007)

PRÉSENTÉE LE 30 MARS 2007

À LA FACULTÉ DES SCIENCES DE BASE

laboratoire de chimie inorganique et bioinorganique

PROGRAMME DOCTORAL EN CHIMIE ET GÉNIE CHIMIQUE

ÉCOLE POLYTECHNIQUE FÉDÉRALE DE LAUSANNE

POUR L'OBTENTION DU GRADE DE DOCTEUR ÈS SCIENCES

PAR

Oleg YAZYEV

Chimiste diplômé, M. V. Lomonosov Moscow State University, Moscou, Russie
et de nationalité ukrainienne

acceptée sur proposition du jury:

Prof. U. Röthlisberger, présidente du jury

Prof. L. Helm, directeur de thèse

Prof. L. Forro, rapporteur

Prof. H. Huber, rapporteur

Dr V. Malkin, rapporteur



ÉCOLE POLYTECHNIQUE
FÉDÉRALE DE LAUSANNE

Suisse
2007

To Yuliya

Table of Contents

Acknowledgements	4
Abstract	6
Version abrégée	8
1 Introduction	11
1.1 MRI contrast agents for biomedical diagnostics	11
1.2 Carbon based materials for future technologies	18
1.3 Outline of the thesis	23
2 Hyperfine interactions in gadolinium aqua complexes	25
2.1 Introduction	25
2.2 Hyperfine interactions and nuclear spin relaxation	27
2.3 Computational approach	30
2.4 Results and Discussion	35
2.4.1 Hyperfine couplings in gadolinium aqua complex	35
2.4.2 Hyperfine couplings in GdDOTA	41
2.5 Practical conclusions	43
3 ^{17}O quadrupole couplings in gadolinium aqua complexes	45
3.1 Introduction	45
3.2 Calculation of ^{17}O quadrupole couplings	46
3.2.1 Theoretical foundations	46
3.2.2 Computational methodology	47
3.2.3 Calibration of ^{17}O quadrupole moment	48
3.3 Quadrupole couplings in model aqua complexes	50

3.4	Quadrupole couplings of gadolinium aqua ions in solution	54
3.4.1	Liquid water and gadolinium aqua complex	54
3.4.2	GdDOTA aqua complex	56
3.5	Implications for ^{17}O NMR relaxation studies	57
4	Pseudopotential calculations of hyperfine interactions	59
4.1	Introduction	59
4.2	Valence contribution to hyperfine coupling constants	60
4.2.1	Isotropic hyperfine coupling constants	60
4.2.2	Dipolar hyperfine coupling constants	62
4.3	Core spin-polarization correction	64
4.3.1	Methodology	64
4.3.2	Benchmarks	67
4.3.3	Trends across the periodic table	70
5	Paramagnetic ions in water: <i>ab initio</i> molecular dynamics	75
5.1	Introduction	75
5.2	Methodology	76
5.3	Discussion and results	78
5.3.1	Aqueous solution of Cr^{3+} : a test case	78
5.3.2	Hyperfine interactions in aqueous solution of Gd^{3+}	82
6	Hyperfine interactions in carbon nanostructures	87
6.1	Introduction	87
6.2	Isotropic Knight shift of metallic carbon nanotubes	89
6.2.1	Computational methods	91
6.2.2	Results	92
6.3	Hyperfine interactions in graphenic nanostructures	96
7	Point defects in carbon nanostructures	105
7.1	Introduction	105
7.2	Magnetism induced by single atom defects	106
7.3	Radiation-induced defect formation	113
7.3.1	Simulations	114
7.3.2	Off-plane recoils	115

7.3.3 In-plane recoils	118
8 Conclusions	121
8.1 Overview of results	121
8.2 Perspectives	123
A Si 2<i>p</i> photoelectron spectra at silicon surfaces and interfaces	125
Bibliography	135
Curriculum vitae	157
Publications	158

Acknowledgements

First of all, I am grateful to my thesis supervisor Prof. Lothar Helm, an excellent scientist and a man of generous soul. His advises and explanations were always helpful for me. His laugh and smile create a very warm and pleasant atmosphere in the group. He gave me a unique chance to realize my own scientific ideas. Many thanks for this!

I'm also indebted to Prof. André Merbach who welcomed me in his group and provided me the conditions I could only imagine. The way his large group was organized amazed me since my first days in the group: a truly Swiss quality mark.

I'm very grateful to Prof. Ursula Röthlisberger and all members of her group. I actually often felt myself as being a member of this group. My very special thanks go to Dr. Ivano Tavernelli for showing me the world of *ab initio* molecular dynamics and making chemistry alive.

I would like to thank Dr. Vladimir Malkin and Dr. Olga Malkina for helping me to do the first steps of my Ph.D. project and for their true Russian hospitality during my stay in Bratislava.

I'm very much indebted to Prof. Alfredo Pasquarello, an excellent teacher and scientist, for showing me how a simple idea can be turned into successful and completed research project. I really enjoyed working with him and I'm glad that our collaboration will continue.

I would like to thank the two other members of my thesis jury, Prof. László Forró and Prof. Hanspeter Huber, who so enthusiastically accepted the invitation.

I'm grateful to adorable secretaries of our group, Mme Emanuela Mancianti and Mme Maria Szuman, for their help with documents, trips, etc. and to our technician Patrick Favre for printing my posters and solving all possible hardware problems. I also wish to thank people from le Magasin-BCH et la Bibliothèque.

I'm also thankful to a number of professors who teach doctoral courses I followed at the EPFL: Prof. Jean-Philippe Ansermet, Prof. Claude Daul, Dr. Jacques Van

Der Klink, Prof. Alfredo Pasquarello (again), Dr. Tomasz Wesolowski, Prof. Pierre Stadelmann, Dr. Ivano Tavernelli (and again). It turned out that all the knowledge I acquired during these courses found an application in my thesis work.

I would like to thank all past and present members of our group: Dr. Pascal Grundler, Dr. Fabrice Riblet, Dr. Genadyi Novitchi, Dr. João Bruno Livramento, Dr. Robert Ruloff, Dr. Caroline Cannizzo, Gabriella Bodizs, Dr. Petra Lebduskova, Dr. Angélique Sour, Dr. Eva Tóth, Dr. László Burai, Dr. Edina Balogh, Dr. Zoltán Jászberényi, Dr. Sabrina Laus. I'm particularly thankful to Dr. Alain Borel and Dr. Fabrice Yerly, the (rare) theoreticians of our group, who shared their knowledge and experience. I would like to mention specially Dr. Meriem Benmelouka and Loïck Moriggi, my pleasant office-mates.

I'm grateful to my new friends Ivan, Kirill, Alena, Petr and Audrius, whom I met in Lausanne. It may sound surprising, but Lausanne became a place of frequent gatherings of our small but solid Moscow-group. The visits of Dmytro, Evgenyi, Natasha and Andrei were always very much expected.

I would like to thank my parents, Valerii and Olga, and my grandparents, ded Misha and babushka Yulya, for their love and worries. I'm also grateful to Yuliya's family: Tonya, Volodya, Lena, Dima and Busya.

Finally, I would like to thank Yuliya for her continuous support, patience, inspiration and love during these years. I dedicate this work to her!

Abstract

The phenomenon of magnetism is one of the key components of today's technological progress. Magnetic interactions and magnetic materials are essential for the scientific disciplines of physics, chemistry and biology, making this subject truly multidisciplinary. This thesis is devoted to magnetic properties of two classes of substances. The first class represents the complexes of the ions of paramagnetic metals, primarily of the gadolinium(III) ion. These molecular compounds have an important application as magnetic resonance imaging (MRI) contrast agents for medical diagnostics. The design of more efficient MRI contrast agents requires a detailed knowledge of their magnetic properties. The other part of the thesis considers the broad class of recently discovered carbon nanostructures and materials. Their extraordinary physical properties foretell future applications of these materials in electronics, medicine and other fields. For instance, carbon nanotubes loaded with gadolinium(III) ion clusters are highly efficient MRI contrast agents.

By using accurate density functional theory calculations in combination with classical molecular dynamics simulations, we determine hyperfine and quadrupole coupling constants on the nuclei of a first coordination sphere water molecule in gadolinium(III) aqua complexes. These parameters play a crucial role in the description of the key function, relaxivity, of MRI contrast agents. We found that the spin-polarization effect induced by the paramagnetic gadolinium(III) ion results in a Fermi contact hyperfine coupling of both the ^1H and ^{17}O nuclear spins and affects the dipole hyperfine coupling of the ^{17}O nuclear spin of the inner coordination sphere water molecule. The ^{17}O quadrupole coupling parameters of a coordinated water molecule are found to be very similar to that of neat water. We also apply the methodology of first principles molecular dynamics in order to perform realistic simulations of paramagnetic metal ions in water solution. This allows us to assess structure, dynamics and hyperfine interactions on the water molecules in the inner and outer coordination spheres of two metal ions: chromium(III)

and gadolinium(III). In order to perform such calculations, we develop a novel approach for the evaluation of hyperfine coupling constants in pseudopotential electronic structure techniques. Our method takes into account the contribution of core electrons.

In the second part of the thesis, we consider magnetic properties of a broad class of carbon nanostructures derived from two-dimensional graphene. We find that in metallic carbon nanotubes, an isotropic Knight shift, a hyperfine contribution to the nuclear magnetic resonance chemical shift, shows a regular dependence on the nanotube diameter. By using a more general approach, we reveal systematic dependences of magnetic interactions between arbitrarily distributed spin-polarized conduction electrons and nuclear spins in the carbon nanostructures derived from graphene. This knowledge is important for interpreting the results of magnetic resonance experiments and for evaluating the performance of carbon nanostructures as materials for alternative approaches in electronics, spintronics and quantum information processing based on electron and nuclear spins. In addition, we study magnetism in graphene induced by single-atom defects. The predicted itinerant magnetism due to the defect-induced states in graphenic materials may account for the experimental observations of ferromagnetism in irradiated graphite which has potential applications in technology. Finally, our first principles molecular dynamics study reveals the mechanisms of the irradiation-induced defect formation. We show that certain defect structures in layered carbon materials can be created selectively by irradiation at predefined conditions.

Keywords: magnetism, hyperfine interactions, magnetic resonance imaging, contrast agent, Gd(III) complexes, carbon nanotubes, graphene, graphite, defects

Version abrégée

Le phénomène de magnétisme est une des composantes clé du progrès technologique d'aujourd'hui. Interactions magnétiques et matériaux magnétiques sont essentiels pour les disciplines scientifiques de physique, chimie et biologie et rendent ainsi ce sujet vraiment multidisciplinaire. Cette thèse est consacrée à l'étude des propriétés magnétiques de deux classes de substances. La première représente des complexes de ions métalliques paramagnétiques, principalement du gadolinium(III). Ces composées moléculaires trouvent une application importante comme agents de contraste pour l'imagerie par résonance magnétique (IRM) pour le diagnostic médical. Le design des agents de contraste pour l'IRM plus efficace exige une connaissance détaillée de leurs propriétés magnétiques. La deuxième partie de la thèse considère la large classe des nanostructures et des matériaux de carbone récemment découverts. Leurs propriétés physiques extraordinaires laissent prédire des applications futures importants, entre autre, dans l'électronique et la médecine. Par exemple, les nanotubes de carbone chargés par des clusters de gadolinium(III) sont des agents de contraste extrêmement efficaces pour l'IRM.

En utilisant la théorie de la fonctionnelle de la densité en combinaison avec les simulations de dynamique moléculaire classique, nous déterminons les constantes de couplage hyperfine et quadripolaire des noyaux des molécules d'eau de la première sphère de coordination des complexes de gadolinium(III). Ces paramètres jouent un rôle crucial dans la description de la fonction clé, la relaxivité, des agents de contraste pour l'IRM. Nous avons constaté que l'effet de polarisation par spin incité par le gadolinium(III) paramagnétique aboutit à des interactions hyperfines de contact de Fermi tant du spin nucléaire du proton que de l'oxygène-17 et affecte les interactions hyperfines dipolaires du spin de l'oxygène-17 de la molécule d'eau de la sphère de coordination interne. Les paramètres de l'interaction quadripolaire de l'oxygène-17 d'une molécule d'eau coordonnée se trouvent être très semblables à ceux de l'eau pure. Nous appliquons aussi la méthodologie de la dynamique moléculaire *ab initio* pour effectuer des simulations réalistes d'ions de métaux

paramagnétiques dans des solutions aqueuses. Cela nous permet d'évaluer la structure, la dynamique et les interactions hyperfines sur les molécules d'eau dans les sphères de coordination internes et externes de deux ions, le chrome(III) et le gadolinium(III). Nous développons une approche originale pour l'évaluation des constants hyperfines dans les techniques de structure électroniques pseudopotentielles qui nous permet de effectuer ces calculs. Notre méthode tient compte de la contribution des électrons de cœur des atomes.

Dans la deuxième partie de la thèse, nous considérons des propriétés magnétiques d'une large classe des nanostructures de carbone construits de graphène bi-dimensionnel. Nous constatons une dépendance régulière de la contribution au déplacement chimique de la résonance du spin nucléaire, le Knight-shift isotropique, avec le diamètre dans le cas des nanotubes de carbone métalliques. En utilisant une approche plus générale, nous révélons des dépendances systématiques d'interactions magnétiques entre les spins des électrons de conduction arbitrairement distribués et les spins nucléaires dans les nanostructures de carbone dérivés de graphène. La connaissance de cette dépendance est importante pour l'interprétation des résultats d'expériences de résonance magnétiques et pour l'évaluation de la performance des nanostructures de carbone comme matériaux pour les approches alternatives dans l'électronique, spintronics et le traitement de l'information quantique basé sur les spins d'électrons et de noyaux. En plus, nous étudions le magnétisme dans le graphène incité par les défauts monoatomiques. Le magnétisme itinérant, prédit en raison des états incités par défauts dans les matériaux dérivés de graphène, peut être la source d'observations expérimentales de ferromagnétisme dans le graphite irradié ayant des applications potentielles en technologie. Finalement, nos études de dynamique moléculaire *ab initio* révèlent les mécanismes de la formation de défauts incités par l'irradiation. Nous montrons que certaines structures de défaut dans les matériaux de carbone laminaires peuvent être créés de manière sélective par irradiation aux conditions prédéterminées.

Mots clé: magnétisme, interactions hyperfines, imagerie par résonance magnétique, agents de contraste, complexes de Gd(III), nanotubes de carbone, graphène, graphite, défauts

Chapter 1

Introduction

The topics covered in my thesis link different scientific disciplines: medical diagnostics, chemistry, and physics, under the common theory of magnetic interactions in matter. This chapter will introduce an unprepared reader to the fields of my thesis with the emphasis on landmark discoveries. Its first part explains the basic principles of magnetic resonance imaging (MRI) and how it can be improved using MRI contrast agents. The second part introduces the reader into the world of carbon-based materials and nanostructures. It explains the importance of magnetic interactions and defects in these systems. To some extent, there exists a linkage between the two: carbon nanostructures can be used in biomedical applications, including MRI.

1.1 MRI contrast agents for biomedical diagnostics

Magnetic resonance imaging is a powerful technique for medical diagnostics and for many fields of research ranging from biology to material science. As a diagnostic tool, it combines several unique advantages over other techniques. Firstly, it is a non-invasive technique and it does not utilize ionizing radiation. In other words, it is harmless for patients. Secondly, MRI is able to provide very detailed information about soft tissues in the form of three-dimensional images. Finally, this technique is able to characterize and discriminate tissues by their physical and biochemical properties, evaluate blood flow, contraction and relaxation of organs.

The physical principle behind MRI is nuclear magnetic resonance (NMR). NMR was discovered by Felix Bloch and Edward Purcell back in 1946 [1–3]. Both of them were awarded the Nobel Prize in Physics as early as in 1952 for their discovery. The NMR

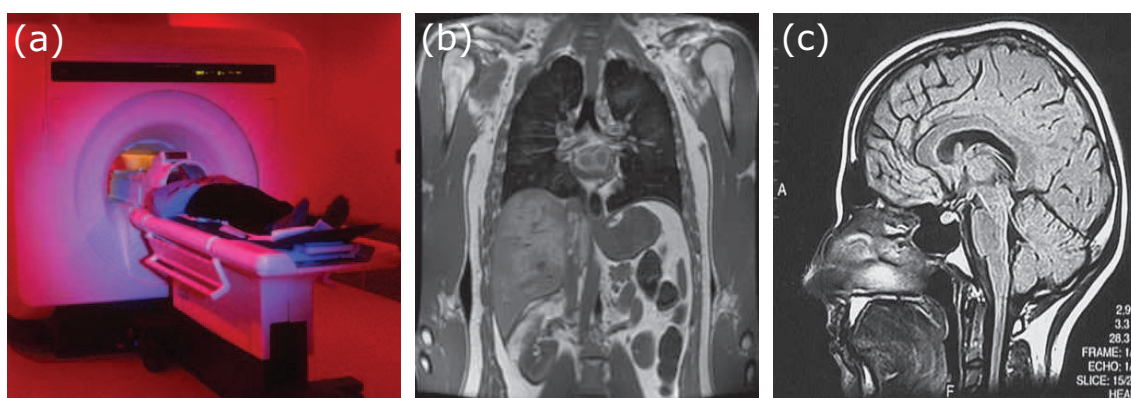


Figure 1.1: A clinical MRI scanner (a) and MRI images of torso (b) and brain (c).

phenomenon is based on the fact that the atomic nuclei which possess a spin angular momentum interact with magnetic fields. Nuclear spins behave as small magnets: their orientations are no longer energetically equivalent once an external magnetic field has been applied. This creates a non-zero equilibrium magnetization of the ensemble of nuclear spins. A short radiofrequency pulse can perturb this equilibrium. After the pulse, nuclear spins start relaxing to equilibrium and emit a detectable radiofrequency signal. The spectrum of this signal is the NMR spectrum. Individual resonance frequencies reflect the magnitude of the applied magnetic field, the nature of nuclear spins and their local chemical environment. Apart from being the underlying principle of MRI, NMR has also made an enormous impact on the other fields of science and technology: NMR spectroscopy has become the most important analytical tool in organic chemistry; elementary quantum computers based on this phenomenon have been built; NMR is used for detecting geological structures, etc.

It took two decades until MRI was developed from the physical principles underlying NMR. In 1971 Raymond Damadian published his finding that tumor tissue has longer NMR relaxation time than normal tissue [4]. Two years later, Paul Lauterbur came out with the idea that magnetic field gradients can be used for spatial localization of the NMR signal [5]. He demonstrated this concept using a setup with two test tubes. The same year, Peter Mansfield also suggested the use of field gradients for spatial localization [6] and suggested so-called “echo-planar imaging” [7]. In 1977, Raymond Damadian performed the first MRI scan of the human body [8] and Richard Ernst, awarded the Nobel Prize in Chemistry in 1991, suggested the use of phase and frequency encoding and Fourier transform [9] which is routinely used in today’s MRI. Very recently, in 2003,

the works of Lauterbur and Mansfield in the field of MRI were recognized by the Nobel Prize in Physiology or Medicine.

Nowadays, over 1 million MRI scans are performed in the world every week. Most commercial MRI scanners utilize magnetic fields of 0.3–3 Tesla. Such machines have become affordable even for small hospitals. The spatial resolution is better than 1 mm and three-dimensional scans of the whole human body can be performed. The resonance of water protons is primarily used for diagnostic purposes since water constitutes about 63% of our bodies and the natural abundance of ^1H isotope is 99.9%. However, high natural abundance isotopes like ^{23}Na and ^{31}P can also be used. Inhaled hyperpolarized ^3He and ^{129}Xe are used for the MRI of lungs.

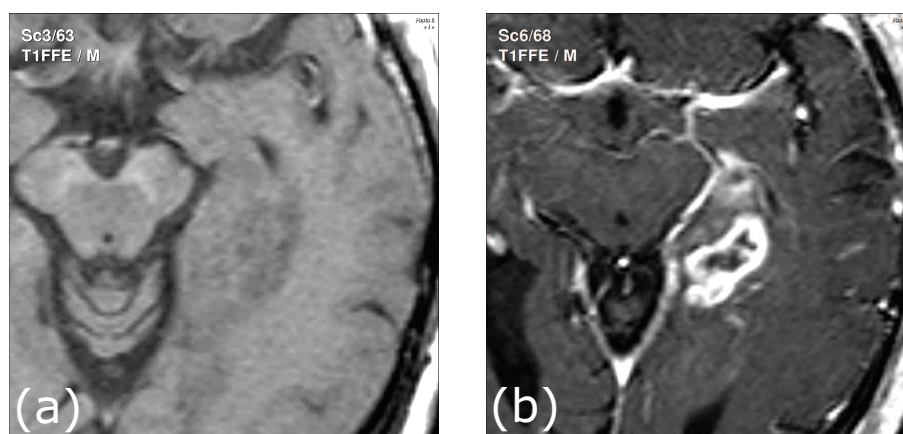


Figure 1.2: T_1 -weighted MRI images of the brain before (a) and after (b) the injection of MRI contrast agent.

More advanced MRI techniques have been developed in last years. So-called functional MRI (fMRI) permits measurements of signal changes in the brain due to changing neural activity [10]. Magnetic resonance spectroscopy imaging (MRSI) permits one to obtain a full NMR spectrum from a selected region in the human body, i.e. the contents of individual chemical compounds in human organs can be investigated [11]. Diffusion tensor imaging (DTI) allows for mapping of fiber directions in brain for the study and diagnostics of diseases [12]. This list of specialized MRI techniques is far from complete.

Magnetic resonance imaging contrast agents are chemical compounds that enhance the contrast between healthy and diseased tissue. Therefore, MRI contrast agents are able to increase accuracy and sensitivity of MRI diagnoses. The contrast created is due to the non-uniform decrease of the relaxation times of proton spins in tissue by means

of the fluctuating magnetic interaction, the hyperfine interaction, with the electron spins of magnetic contrast media. Two types of MRI contrast agents are currently used in practice: stable complexes of paramagnetic metal ions, typically of the Gd^{3+} ion, and superparamagnetic contrast agents based on iron oxide nanoparticles. The gadolinium-based contrast agents are advantageous in many cases since they provide bright contrast in T_1 -weighted images (Fig. 1.2).

The gadolinium-based MRI contrast agents are complexes containing a Gd^{3+} ion, a chelating ligand and, typically, one or two water molecules in the inner sphere of the Gd^{3+} ion. The choice of Gd^{3+} as a paramagnetic ion is for several reasons. First of all, this ion situated in the middle of the lanthanide series is characterized by a large magnetic moment due to the half-filled $4f$ shell (7 unpaired electrons!). Secondly, due to the symmetric S state this ion has a relatively long electron spin relaxation time which is one of the necessary requirements for efficient paramagnetic relaxation enhancement (PRE). The bare Gd^{3+} ion has a considerable drawback – toxicity. For this reason the paramagnetic Gd^{3+} ion is used in the form of inert complexes with chelating ligands. In complexes with such ligands the ion is normally nine-coordinate, with seven or eight coordination sites occupied by the ligand. The majority of commercial MRI contrast agents use poly(amino carboxylates) as ligands. Chemical structures of some of these ligands are shown in Figure 1.3. One or two sites in the coordination sphere of the ion are occupied by water molecules. The role of this water molecule is crucial for the efficiency of MRI contrast agent since its nuclear spins are strongly influenced by the magnetic moment of the neighbor Gd^{3+} ion.

Development of more efficient novel MRI contrast agents is one of the important goals of the research in this field. The efficiency of an MRI contrast agent can be quantified by its relaxivity, r_1 , which is defined as the increase of the longitudinal relaxation rate of the water protons per mM of the paramagnetic compound,

$$\frac{1}{T_{1,obs}} = \frac{1}{T_{1,d}} + r_1[Gd^{3+}], \quad (1.1)$$

where $1/T_{1,obs}$ and $1/T_{1,d}$ are the longitudinal relaxation rates in the presence and in the absence of the MRI contrast agent, respectively. The relaxivity can be divided into the contributions of the inner and outer coordination spheres, $r_1=r_1^{IS}+r_1^{OS}$.

Modeling the relaxivities of contrast agents is by no means a simple task. A number of theories have been developed, e.g. the Solomon-Bloembergen-Morgan theory [14–17] which describes the relaxation of the inner sphere water molecule in paramagnetic

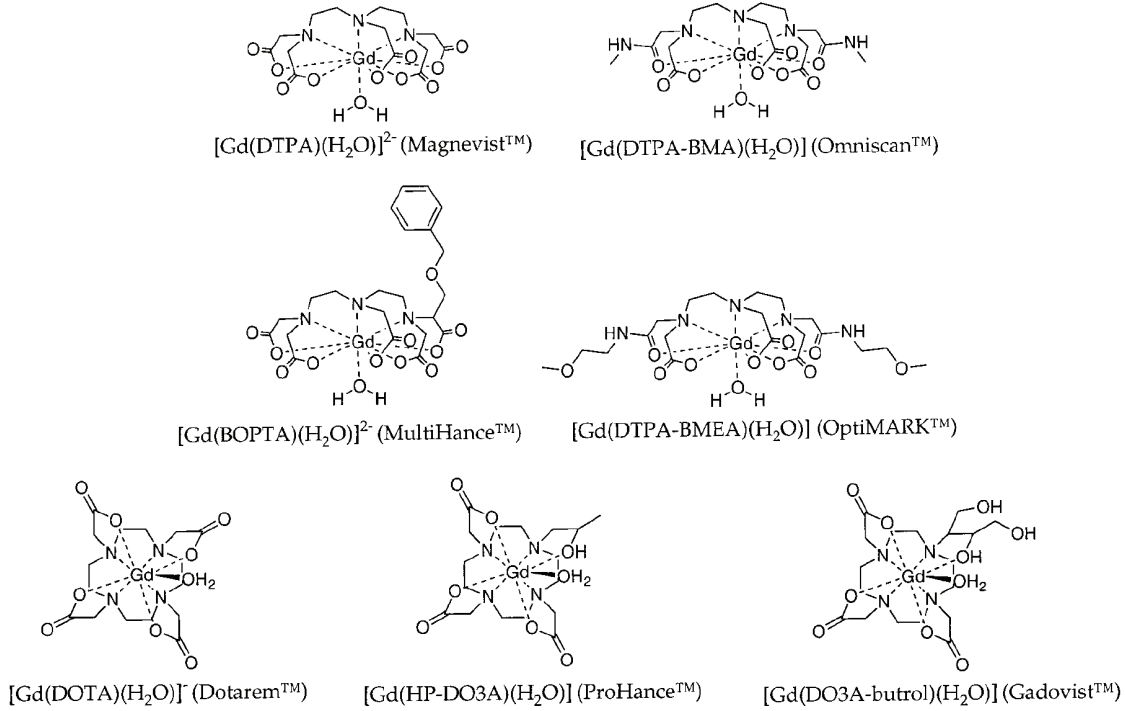


Figure 1.3: Chemical structures of some commercially available Gd-based MRI contrast agents (adopted from Ref. [13]).

complexes. I will refrain from going into details of these theories in this preliminary introduction. More detail can be found in Chapters 2 and 3 and in original references. However, in the most general form the relaxivity can be written as a function of two sets of parameters

$$r_1 = f(\{A_{iso}, \overleftrightarrow{T}, \overleftrightarrow{Q}, \dots\}, \{k_{ex}, T_{1e}, T_{2e}, \tau_R, \dots\}). \quad (1.2)$$

The first set of parameters is responsible for interactions of nuclear spins with electron surrounding. Regarding the paramagnetic relaxation enhancement, the most important here are the Fermi contact (A_{iso}) and the dipolar (\overleftrightarrow{T}) hyperfine interactions (HFIs), i.e. the magnetic interaction between the spins of nuclei and electrons. The interactions of nuclear quadrupoles with the electric field gradient (EFG) described by the quadrupole coupling tensor \overleftrightarrow{Q} are important for the description of relaxation of nuclei with a spin number larger than 1/2, like ¹⁷O nuclei. The second set of parameters in eq. (1.2) is responsible for the dynamic part of the problem. The most important parameters here are the exchange rate between the bound water molecules and the bulk water, k_{ex} , the longitudinal and transverse electronic relaxation times, T_{1e} and T_{2e} , and the rotational

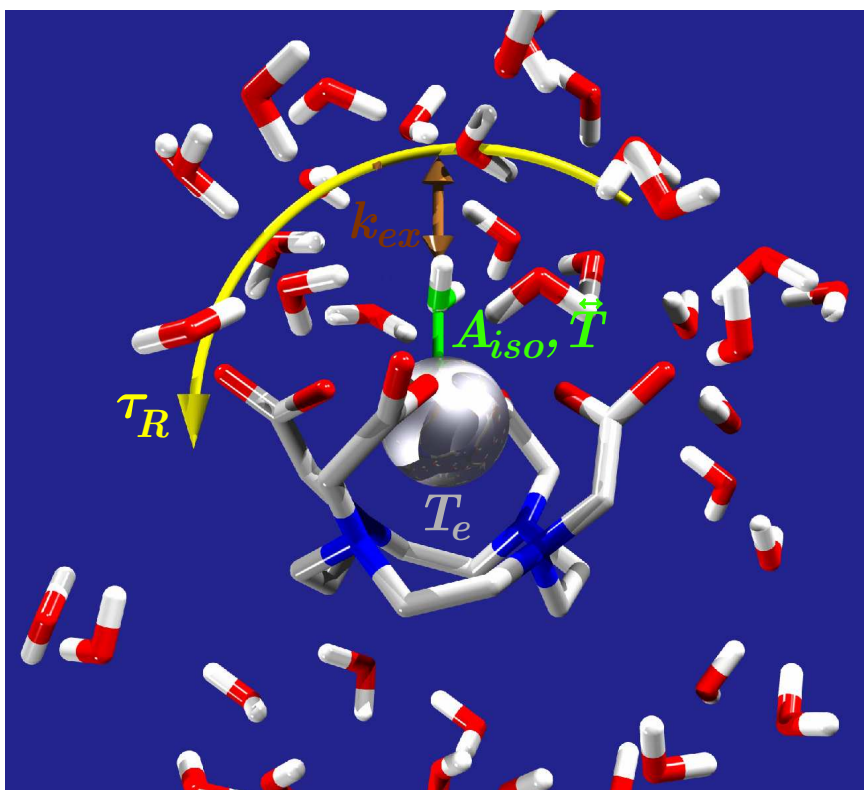


Figure 1.4: Scheme showing important interaction (A_{iso} , \vec{T}) and dynamic (T_e , k_{ex} and τ_r) parameters defining the efficiency of an MRI contrast agent (GdDOTA on this figure).

correlation time τ_R which describes the tumbling of the vector connecting the Gd ion and the inner sphere protons. These parameters are schematically summarized in Figure 1.4. The dynamic parameters, primarily k_{ex} and τ_R , can be tuned by tailoring the structure of chelating ligand. For instance, high relaxation rates of the inner sphere water protons are favored by long rotational correlation times. Such large τ_R values have been recently achieved by the synthesis of higher molecular weight ligands through the attachment of the poly(amino carboxylate) ligands to proteins, micelles or dendrimers. Figure 1.5 illustrates how the inner sphere ^1H relaxivity changes as a function of k_{ex} and τ_R with the rest of external parameters being fixed.

Development of novel efficient MRI contrast agents requires detailed knowledge of the underlying parameters. Thus, a question naturally rises: How to assess these parameters?

An evident way is to use experimentally available data. Several techniques can provide such data. First, there are the nuclear magnetic resonance dispersion (NMRD) profiles, where the relaxivity is measured as a function of the external magnetic field. Another

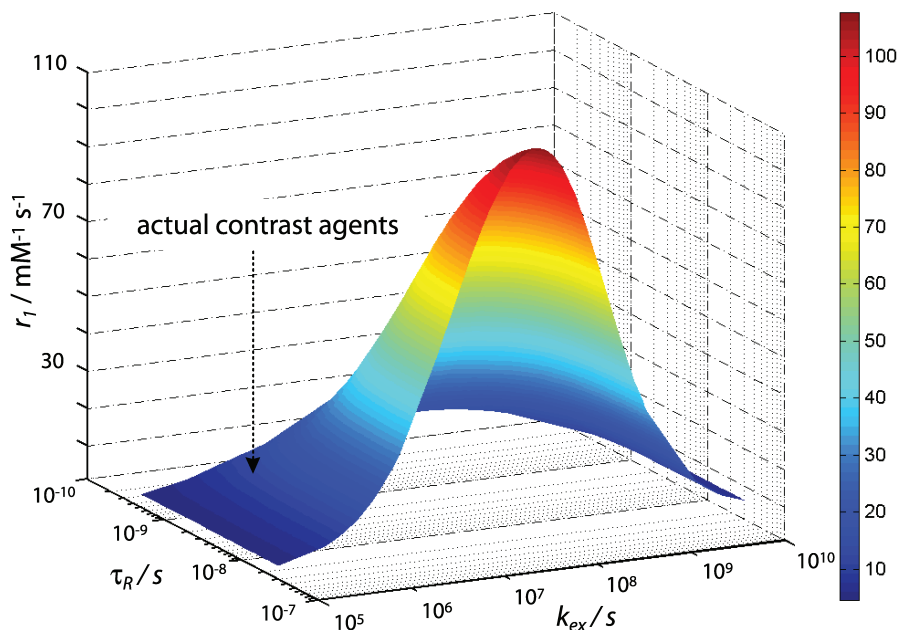


Figure 1.5: Inner sphere ^1H relaxivities, calculated as function of k_{ex} and τ_R at 20 MHz. ($\Delta^2 = 0.03 \times 10^{20} \text{ s}^{-2}$ and $\tau_v = 15 \text{ ps}$)

useful technique is ^{17}O NMR. Although the relaxation of proton spins is of primary importance, probing the ^{17}O nuclei provides important information about the dynamics of the inner sphere water molecule. Variable temperature measurement of the ^{17}O chemical shifts and relaxation rates help to determine k_{ex} and τ_R . Electron spin relaxation can be assessed by means of electron spin resonance (ESR) spectroscopy. The large amount of experimental data collected using these techniques is then fitted to known physical models and provides the whole set of parameters [18].

Another way to assess these parameters is performing *in silico*, i.e. computational, virtual, experiments. Interaction parameters, hyperfine and quadrupolar coupling constants, can be obtained from electronic structure calculations. Molecular dynamics simulations can provide information about correlation times. A large part of this thesis is dedicated to such computational experiments for the rational design of efficient MRI contrast agents.

1.2 Carbon based materials for future technologies

Carbon is the basis of organic life on planet Earth due to its ability to form a huge number of molecular frameworks with itself and other elements. However, until about 20 year ago only two distinct carbon allotropes were known: diamond and graphite. Very recently this situation has changed dramatically. A wide range of all-carbon nanostructures have been discovered and the definition of a distinct carbon allotrope became vague.

Graphite, a naturally occurring form of carbon, is composed of two-dimensional layers of sp^2 carbon atoms bound to each other by only weak Van der Waals forces (Fig. 1.6). The anisotropy of the three-dimensional graphite lattice results in anisotropy of electric and thermal conductance, mechanical properties. Graphite is used as marking material in pencils and as lubricant due to this mechanic anisotropy.

In 1985 a zero-dimensional form of carbon called fullerene has been discovered [19]. Individual fullerene molecules are hollow structures obtained by wrapping a single graphite layer over a closed surface with some number of topological defects (five-membered rings) introduced. The most common representative is the C_{60} molecule. Its nearly spherical shape closely resembles a soccer ball. For their discovery Harald Kroto, Robert Curl and Richard Smalley were awarded the Nobel Prize in Chemistry in 1996.

In 1991, Sumio Iijima discovered one-dimensional forms of carbon which are now called carbon nanotubes [20]. Like fullerenes, carbon nanotubes are closely related to graphite. Single-walled carbon nanotubes can be obtained by rolling-up a single graphite sheet to form cylindrical surfaces. More complex superstructures, bundles of nanotubes and multiwalled carbon nanotubes, in which individual single-walled carbon nanotubes are bound together by the weak Van der Waals interactions, are often produced. Presently, carbon nanotubes are routinely synthesized by carbon-arc discharge, laser ablation of carbon, or chemical vapor deposition on catalytic particles [21].

A two-dimensional single graphite sheet, named graphene, was isolated only in 2004 by researchers from Manchester and Moscow [22]. Ironically, monoatomic layers of graphene were produced by simple mechanical exfoliation of graphite. In other words, graphene was found in a pencil trace. The same year, graphene was also produced by the thermal sublimation of silicon from a silicon carbide surface [23]. Discoveries of unusual physical properties of graphene, such as the anomalous quantum Hall effect and the absence of localization [24, 25], have fueled enormous interest to this simple honeycomb-like structure.

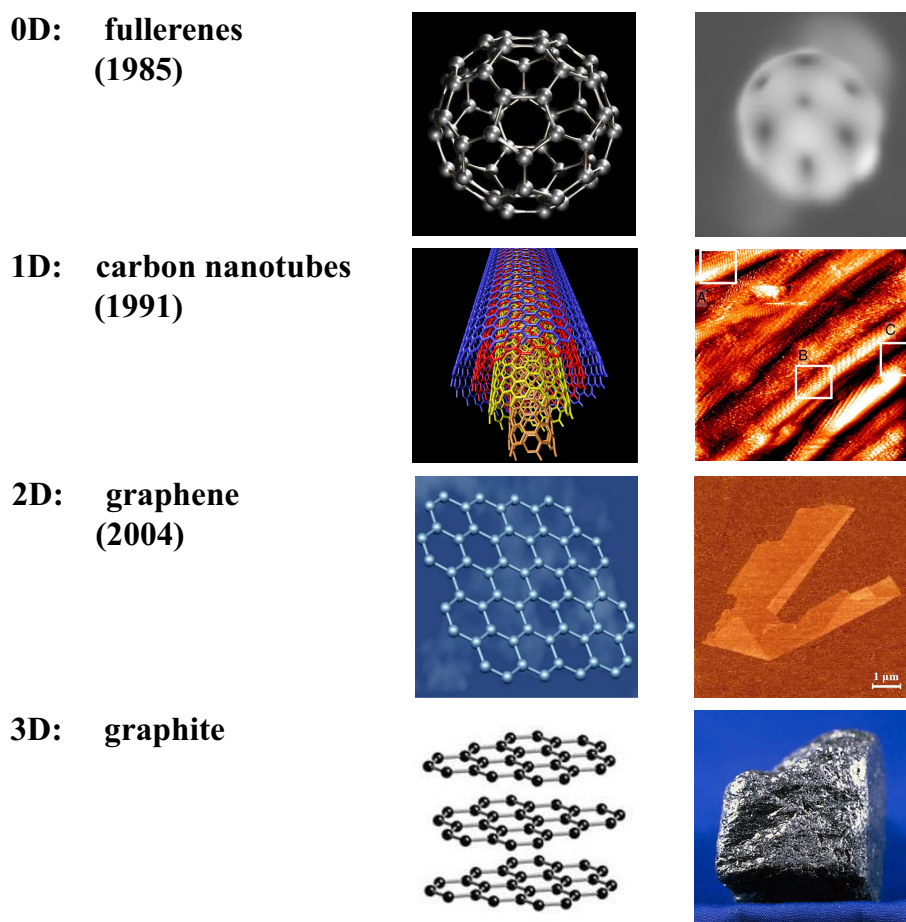


Figure 1.6: Carbon materials of different dimensionalities. The columns show their atomic structures and natural appearance. The images of the single C_{60} molecule and of the bundle of carbon nanotubes were obtained using scanning tunneling microscopy (STM). The image of the graphene flake was obtained with the help of atomic force microscopy (AFM).

The electronic structure of graphene can be deduced from a simple nearest-neighbor tight binding model [26]. Its band structure is schematically shown in Figure 1.7. Valence and conduction bands form two conical intersections in the Brillouin zone at K points with the electron energy linearly dependent on the wave vector. Graphene is a semimetal. In other words, it is a metal with zero density of states at the Fermi level, or a gapless semiconductor. The unusual spectrum in the vicinity of the Fermi level resembles the Dirac spectrum of massless fermions, relativistic quantum particles with spin $1/2$. The role of the speed of light in the Dirac-like equation plays the Fermi velocity $v_F \approx c/300$. This similarity has led to a popular paradigm of relativistic physics of graphene. In any

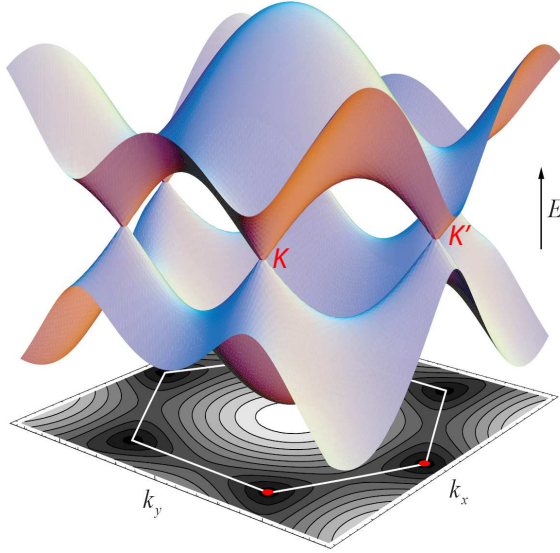


Figure 1.7: Band structure of graphene. Conduction and valence bands form conical intersections at points K and K' . The Brillouin zone of graphene is shown on the projection plane.

case, the behavior of charge carriers in graphene is expected to be different from that in normal metals and semiconductors with parabolic dispersion of electron energies.

The electronic properties of carbon nanotubes are another interesting topic. Carbon nanotubes can have different atomic structures depending on the orientation of the circumference vector with respect to the graphene lattice and on the nanotube diameter (Fig. 1.8a). Carbon nanotubes are commonly classified by the pair of chiral indices, (n, m) , which relate the circumference vector $\vec{C} = n\vec{a}_1 + m\vec{a}_2$ to the unit vectors of the graphene lattice. (n, n) carbon nanotubes are called armchair nanotubes, $(n, 0)$ are zigzag nanotubes while the rest are chiral carbon nanotubes (Fig. 1.8b). Deriving the band structures of carbon nanotubes from the graphene band structure using the zone folding approximation [27] one finds surprising regularities confirmed by experimental observations. All nanotubes with $n - m = 3l$ (l – integer number) are metals, the rest are semiconductors. In reality, all $n - m = 3l$ carbon nanotubes except armchair nanotubes possess tiny band gaps due to the curvature effect. Band gaps of semiconducting nanotubes are inversely proportional to their diameters. These enviable regularities would permit one to control the characteristics of an electronic device based on carbon nanotubes by tailoring its atomic structure – a paradigm for the next generation engineering.

Although carbon nanotubes are anticipated as a component of next generation materials with extreme mechanical properties, in my thesis I focus primarily on electronic properties of carbon based materials. A quick review of the current achievements and a

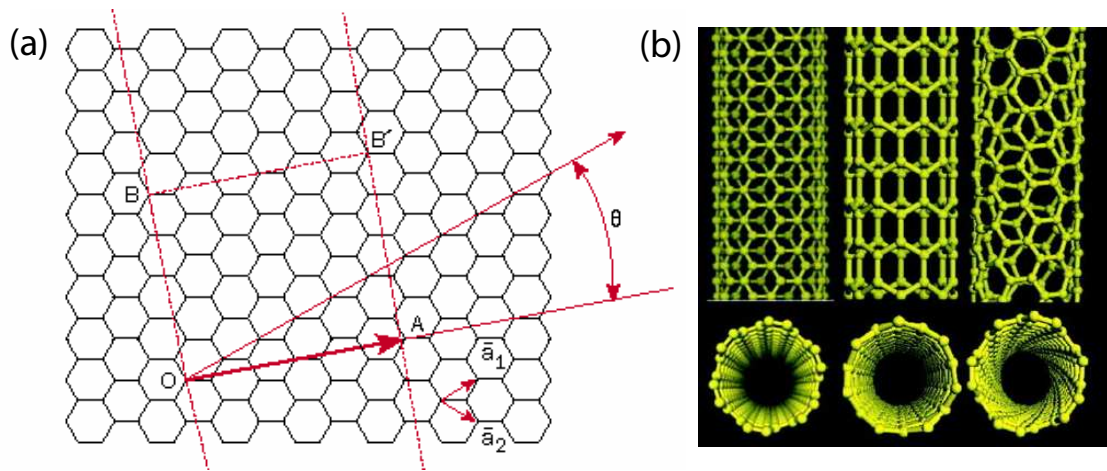


Figure 1.8: (a) Rolling-up a graphene sheet along different choices of the circumference vector (red arrow) produces different nanotube structures. (b) Geometries of armchair, zigzag and chiral single wall carbon nanotubes.

forecast for the nearest future provide motivation for the work described in the second part of my thesis.

First of all, carbon nanotubes and graphene display exceedingly high carrier mobilities [28]. This makes them potential successors to silicon in manufacturing future electronic devices. Working prototypes of field effect transistors based on carbon nanotubes have been manufactured [29]. However, no technology for the production of complicated large-scale electronic devices based on carbon nanotubes has been developed yet. Graphene, however, allows nanopatterning by lithographic techniques [30] which makes it very promising for manufacturing electronic devices using existing technologies. An implementation of field-effect transistor based graphene nanoribbons has been reported very recently [31].

Carbon based nanostructures are also viewed as building blocks for alternative directions of electronics, e.g. spintronics [32]. Spintronics anticipates the use of the spin of an electron in addition to its charge, which is the basis of traditional electronics. It is predicted that spintronics will bring in the advantages of nonvolatility of data storage, faster data processing, higher storage density and lower energy consumption. One has to distinguish spintronics from magnetoelectronics which uses electron spins only for storing information. This is widely used in current data storage technology (e. g. read-write heads of hard drives). Spintronics devices use spin-polarized currents also for transport-

ing data. Here lies one of the problems of spintronics – the preservation of spin-polarized currents in conducting materials. In a typical non-magnetic metal, a non-equilibrium current of spin-polarized electrons relaxes to the equilibrium state with zero magnetization after traveling few tens of nanometers. This relaxation is driven by spin-orbit and hyperfine interactions. The use of carbon nanotubes and graphene, in which spin-orbit interaction is negligible and hyperfine interactions are reduced, extends the spin diffusion length scale by at least one order of magnitude (to sub-micrometer lengths) [33, 34]. A spin diffusion length of $1.5 \mu\text{m}$ has been achieved very recently [35]. Can we extend this length further by minimizing hyperfine interactions, and how?

The question of possible long-range magnetic ordering in all-carbon materials now rises naturally. In current technological applications, magnetic materials are based exclusively on d and f elements. Carbon-based magnetic materials would bring a new prospective to technologies relying on magnetism. Such materials may have low density, be transparent or environment-friendly. Surprisingly, the first organic ferromagnet, the γ -phase p -nitrophenyl nitronyl nitroxide (p -NPNN) was discovered only in 1991 [36]. The ferromagnetic transition temperature (or Curie temperature, T_c) above which the long-range magnetic ordering is suppressed was only 0.65 K. Since that time a great number of similar crystalline stable free radicals have been studied, but all have Curie temperatures too low for practical applications. In 2001 Makarova *et al.* reported the ferromagnetism of rhombohedral C_{60} under high pressure [37] with a Curie temperature near 500 K. Although this discovery was refuted recently (refer to the paper retraction notice [38]) because the magnetic signal observed in [37] was attributed to the cementite (iron carbide Fe_3C) impurity, the paper initiated a new wave of search for magnetism in light element compounds. The high temperature ferromagnetism in graphite induced by the radiation treatment [39, 40] seems to be undoubted. It is believed that the radiation-induced defects (see Fig. 1.9) play a crucial role in explaining ferromagnetism of irradiated graphite, but detailed knowledge of the underlying physical mechanism remains unknown.

Point defects created by irradiation do not only modify the electronic structure of carbon materials. Irradiation treatment can also be used for a purposeful modification of mechanical properties of carbon materials. A striking example is the reinforcement of carbon nanotube bundles by an 80 keV electron beam irradiation. Individual carbon nanotubes are held together in a bundle only by weak Van der Waals forces which results in a low shear modulus, an undesired property. The irradiation with electrons of moderate energies produces defects linking neighbor carbon nanotubes by strong covalent bonds.

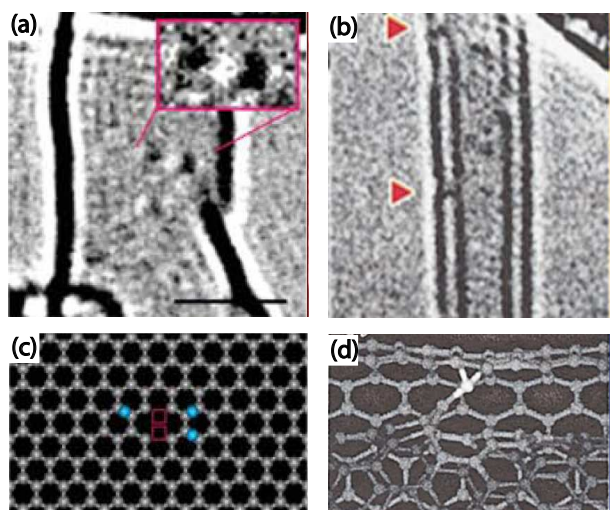


Figure 1.9: Transmission electron microscopy (TEM) images of the defects in (a) carbon nanohorns [41] and (b) double-wall carbon nanotubes [42] produced by the electron irradiation. These experimental images were interpreted as a cluster of the vacancies and adatoms (c) and as intimate interlayer defects (d).

A 30-fold increase of the bending modulus has been observed for irradiated nanotube bundles [43]. However, the atomic structure of these covalent links is unknown. An important question is: can one control irradiation effects in carbon nanostructures and create certain defect structures selectively?

1.3 Outline of the thesis

The thesis focuses on theoretical investigations of magnetic properties of the above mentioned magnetic systems. The method of choice is the density functional theory in our theoretical studies. The outline of the consequent chapters is as follows:

In Chapter 2 and Chapter 3 we study, respectively, hyperfine and quadrupole interactions on the nuclei of a first coordination sphere water molecule of gadolinium(III) aqua complexes. The gadolinium(III) aqua ion, $[\text{Gd}(\text{H}_2\text{O})_8]^{3+}$, and the $[\text{GdDOTA}(\text{H}_2\text{O})]^-$ complex used in real-world clinical diagnostics will serve as prototypical models.

In Chapter 4 we present a methodology for calculating the hyperfine interaction parameters in electronic structure techniques using pseudopotentials.

Chapter 5 describes the results of *ab initio* molecular dynamics simulations of two paramagnetic metal ions in water solutions. The chromium(III) ion serves as a test case, while the results for gadolinium(III) ion have direct relevance to the class of complexes used as MRI contrast agents.

Hyperfine interactions in carbon nanostructures are studied in Chapter 6. The investigation of Knight shifts in metallic carbon nanotubes is presented in the first part.

Afterwards, a more general theory of hyperfine interactions in carbon nanostructures is described.

In Chapter 7 we present our viewpoint on the phenomenon of magnetism induced by point defects in carbon nanostructures. The first principles molecular dynamics study of the irradiation-induced defect formation in layered carbon nanostructures is presented in the second part of the chapter.

Chapter 8 concludes the key results of my thesis and gives perspectives for future studies in the field.

In the Appendix I describe work on the theory of X-ray photoemission spectroscopy of silicon surfaces and interfaces which was performed during my doctoral studies.

Chapter 2

Hyperfine interactions in gadolinium aqua complexes

2.1 Introduction

The ligand hyperfine interactions, the hyperfine interactions of distant (ligand) nuclei in paramagnetic *d*-transition metal and lanthanide complexes, are the driving force of NMR relaxation of solvent nuclei in solutions of paramagnetic species [44]. The paramagnetic relaxation enhancement (PRE) phenomenon found an important practical application in medical diagnostics. It is the underlying physical principle beyond the contrast agents for magnetic resonance imaging (MRI) [13, 45–48]. Currently, typical representatives of MRI contrast agents are gadolinium(III) complexes because of their high spin state (8S state, half-filled *f*-shell) and slow electron spin relaxation. Gd(III) based MRI contrast agents are probably one of the most striking examples where the purely quantum nature of HFI directly leads to a diagnostic tool, namely, increase in contrast in an MRI image, which cannot be described by means of any kind of classical theory.

Furthermore, paramagnetic *d*-transition metal and lanthanide ions are used as natural or artificial probes to study structure of biological objects using experimental techniques mentioned above [49]. For instance, paramagnetic relaxation enhancement (PRE) studies of systems containing highly paramagnetic Mn^{2+} and Gd^{3+} ions can provide ultimate long-range structural constraints up to 40 Å for determination of the structure of biological objects [44, 50–53].

In the case of gadolinium aqua ions, the main contribution to the paramagnetic enhancement of longitudinal relaxation comes from dipolar contribution to HFI. The

PRE for first coordination sphere water molecules is commonly described by Solomon-Bloembergen-Morgan (SBM) equations [14–17]. In the original formulation, these equations suggest the point-dipole approximation in which unpaired electrons are considered as localized at the position of the paramagnetic metal center. Any spin distribution effects over the system are therefore neglected. Due to this approximation the dipolar contribution to HFI can be described by using only information on the distance between the nucleus of interest and the nucleus of the paramagnetic center. This information can be obtained from diffraction experiments, for example. It is also worth mentioning that full knowledge of the dipolar HFI tensor is not easily accessible with existing experimental techniques and therefore the point-dipole approximation is inevitable.

Quantum chemical calculations can provide some a priori knowledge of dipolar HFI. The first step in this direction was made by Kowalewski *et al.* [54–56] in early studies of model aqua complexes of first row transition metal ions using the unrestricted Hartree-Fock (UHF) method. Their results clearly demonstrated the limitations of the point-dipole approximation. Later UHF studies of Das *et al.* [57–59] and density functional theory (DFT) calculations of *Clostridium pasteurianum* iron- (III) rubredoxin protein model system by Wilkens *et al.* [60] confirmed this conclusion. Quantum chemical description of the system makes it possible to generalize the Solomon-Bloembergen-Morgan equations and to avoid the point-dipole approximation even at the estimative level. The origin of ligand HFI in complexes containing a paramagnetic lanthanide ion is different from that of *d*-transition metal ions. Due to the core character of the *f*-shell any significant contribution of ligand atomic orbitals to singly occupied molecular orbitals (SOMOs) is improbable [61]. However, the effect called spin-polarization [62] may manifest in lanthanide complexes. A more detailed knowledge about the mechanisms of HFI in lanthanide complexes is required to obtain reliable parameters for structural and dynamic investigations.

In this Chapter, we study isotropic and dipolar HFI on ^1H and ^{17}O nuclei of a first coordination sphere water molecule in Gd(III) complexes. The main purpose of this part of our work is to show the limitations of point-dipole approximation for dipolar contributions to HFI of first coordination sphere water molecules in Gd(III) complexes and to propose corrections if possible. The deep understanding of underlying physical phenomena in this class of chemical compounds is a necessary element for future development of effective MRI contrast agents for medical and other applications.

2.2 Hyperfine interactions and nuclear spin relaxation

Hyperfine interactions are magnetic interactions between nuclear and electron spins. The corresponding spin-Hamiltonian of this interaction can be written as

$$\hat{\mathbf{H}} = \mathbf{S} \cdot \overleftrightarrow{\mathbf{A}} \cdot \mathbf{I} \quad (2.1)$$

where $\overleftrightarrow{\mathbf{A}}$ is the 3×3 HFI tensor and \mathbf{S} and \mathbf{I} are the vectors of the electron and the nuclear spin, respectively. The HFI tensor can be split into isotropic and anisotropic parts,

$$\overleftrightarrow{\mathbf{A}} = A_{iso} \overleftrightarrow{\mathbf{1}} + \overleftrightarrow{\mathbf{T}} \quad (2.2)$$

where A_{iso} is the isotropic hyperfine coupling constant (scalar); $\overleftrightarrow{\mathbf{1}}$ is the 3×3 unit matrix, and $\overleftrightarrow{\mathbf{T}}$ is the traceless matrix of the anisotropic contribution. Within the commonly used Breit-Pauli approximation [63], the scalar isotropic (Fermi contact) hyperfine coupling constant on nucleus N is

$$A_{iso}(N) = \frac{4\pi}{3S} \beta_e \beta_N g_e g_N \rho^s(\vec{R}_N) \quad (2.3)$$

and a matrix element of the anisotropic (dipolar) contribution is

$$T_{ij}(N) = \frac{1}{2S} \beta_e \beta_N g_e g_N \int \rho^s(\mathbf{r}) \frac{(\mathbf{r} - \mathbf{R}_N)^2 \delta_{ij} - 3(r_i - R_{Ni})(r_j - R_{Nj})}{(\mathbf{r} - \mathbf{R}_N)^5} d\mathbf{r} \quad (2.4)$$

where β_e and β_N are Bohr and nuclear magnetons, respectively, g_e and g_N are free-electron and nuclear g -values, and S is the total electronic spin of the atom, ion, or molecule. Thus, both contributions depend only on the distribution of the electron spin density, the difference between the majority spin density and the minority spin density, $\rho^s(\mathbf{r}) = \rho^\uparrow(\mathbf{r}) - \rho^\downarrow(\mathbf{r})$, of the system in the spin state S and physical constants.

The physical interpretations of the two contributions to $\overleftrightarrow{\mathbf{A}}$ are as follows. The isotropic contribution (Fermi contact), A_{iso} , is proportional to the value of the spin density at the position of nucleus N , therefore it possesses a local character. Physically this contribution represents a magnetic field generated at the point of nucleus by the presence of the electron magnetic moment itself. On the contrary, the anisotropic contribution, $\overleftrightarrow{\mathbf{T}}$, is the dipolar integral over the whole space and has therefore a nonlocal character. It

represents the dipole-dipole type of magnetic interaction between the magnetic moments of nuclear and electron spins. The dipolar contribution vanishes if the spin density is highly symmetric when observed from the point of nucleus N .

In many cases the spin density distribution is determined by the shapes of singly occupied molecular orbitals (SOMOs). This contribution is usually called spin-delocalization and it is always positive, if one follows the above-mentioned convention for spin-up and spin-down electron densities. A second part of spin density comes from so-called spin-polarization effects, which originate from nonequal potentials experienced by spin-up and spin-down electrons and orthogonality constraints imposed on MOs: this leads to different shapes of spin-up and spin-down MOs (which otherwise would be doubly occupied). This contribution can be positive as well as negative at the location of nucleus N , but it always integrates to zero. Spin-polarization effects can be described in short as “an effective attraction”: the localized unpaired electrons “attract” the nearby ones of the same spin. This can result in a negative spin density in the vicinity of SOMO nodes and where SOMO density is vanishing and in a slight increase of positive spin density, produced by the spin-delocalization effect. Spin-polarization is often referred to as a second-order effect [64]. The superposition of these two effects will be referred to as spin-distribution from now on.

In chemical systems involving paramagnetic metal ions it is common to separate the notions of hyperfine coupling constants on the metal nucleus and on ligand nuclei. In this work we discuss only ligand hyperfine interactions which are often referred to as superhyperfine coupling. The simplest possible model for ligand HFI is the point-dipole approximation [56]. Within this approximation spin-distribution effects are neglected and the dipolar ligand HFI tensor $\overleftrightarrow{\mathbf{T}}^{PD}$ depends only on the distance between the metal and ligand nuclei, r_{MX} . Thus, $\overleftrightarrow{\mathbf{T}}^{PD}$ can be written in the form

$$\overleftrightarrow{\mathbf{T}}^{PD} = \beta_e \beta_N g_e g_N \frac{1}{r_{MX}^3} \begin{pmatrix} 2 & 0 & 0 \\ 0 & -1 & 0 \\ 0 & 0 & -1 \end{pmatrix} \quad (2.5)$$

assuming that the metal-ligand nucleus vector is $(r_{MX}, 0, 0)$. It is also worth mentioning that this approximation results in a zero isotropic hyperfine coupling constant on all ligand nuclei since all the spin density is located on the metal ion. Thus, nonzero ligand isotropic hyperfine coupling constants (which are often experimentally measurable) tell us immediately about the deficiency of the point-dipole approximation. The sign of the ligand hyperfine coupling constant provides the sign of the spin density at the position

of ligand nuclei and thus gives the important information about the relative magnitude of spin-delocalization and spin-polarization effects.

Hyperfine interaction results in a shift of NMR resonance frequency and in an enhancement of nuclear spin relaxation. The SBM equations [14–17] describe the increase of longitudinal, $1/T_1$, and transverse, $1/T_2$, relaxation rates of ligand nuclei in the inner coordination sphere of a paramagnetic complex due to the time-dependent interaction with the electron spin. As in the general case of hyperfine interactions, relaxation rates can also be split into a scalar (Fermi contact) $1/T_i^{SC}$ and a dipolar $1/T_i^{DD}$ contribution,

$$\frac{1}{T_1^{SC}} = \frac{2S(S+1)}{3} \left(\frac{A}{\hbar} \right)^2 \left[\frac{\tau_{s2}}{1 + \omega_S^2 \tau_{s2}^2} \right] \quad (2.6)$$

$$\frac{1}{T_2^{SC}} = \frac{2S(S+1)}{3} \left(\frac{A}{\hbar} \right)^2 \left[\frac{\tau_{s2}}{1 + \omega_S^2 \tau_{s2}^2} + \tau_{s1} \right] \quad (2.7)$$

$$\frac{1}{T_1^{DD}} = \frac{2}{15} \frac{(\beta_e \beta_N g_e g_N)^2}{r_{MX}^6} S(S+1) \left(\frac{\mu_0}{4\pi} \right)^2 \left[7 \frac{\tau_{d2}}{1 + \omega_S^2 \tau_{d2}^2} + 3 \frac{\tau_{d1}}{1 + \omega_I^2 \tau_{d1}^2} \right] \quad (2.8)$$

$$\frac{1}{T_2^{DD}} = \frac{1}{15} \frac{(\beta_e \beta_N g_e g_N)^2}{r_{MX}^6} S(S+1) \left(\frac{\mu_0}{4\pi} \right)^2 \left[13 \frac{\tau_{d2}}{1 + \omega_S^2 \tau_{d2}^2} + 3 \frac{\tau_{d1}}{1 + \omega_I^2 \tau_{d1}^2} + 4\tau_{d1} \right] \quad (2.9)$$

where ω_S and ω_I are the electron and nuclear Larmor frequencies in $\text{rad}\cdot\text{s}^{-1}$, r_{MX} is the distance between the nucleus of the paramagnetic ion and the ligand nucleus under observation, and τ_{si} and τ_{di} are characteristic correlation times of scalar and dipolar relaxation processes which in turn depend on the correlation times of molecular rotation, τ_R , on the residence time of the ligand in the inner coordination sphere of the paramagnetic ion, τ_M , and on electron spin relaxation times, T_{1e}, T_{2e} . Note that A/\hbar in SBM equations is equal to $2\pi A_{iso}$ as defined in eq. 2.3.

Once the principal values (two independent parameters) of the dipolar HFI tensor $\overleftrightarrow{\mathbf{T}}$ are known (from quantum-chemical calculations, for example), it is possible to overcome the point-dipole approximation. One can rewrite the ‘‘HFI factor’’ in the dipolar SBM equations in a generalized form introducing the notation of an ‘‘effective’’ distance r_{eff} [54–56] for the dipole-dipole interaction,

$$r_{eff} = \left(\frac{S}{\beta_e \beta_N g_e g_N} \right)^2 \left[T_{zz}^2 + \frac{1}{3} (T_{xx} - T_{yy})^2 \right]^{-1/6} \quad (2.10)$$

where T_{zz} is the maximal absolute value of the principal components of the dipolar HFI tensor and T_{xx}, T_{yy} are the other two eigenvalues of $\overleftrightarrow{\mathbf{T}}$. Because of the $1/r^3$ dependence of dipolar interactions, even small spin-distribution effects on the ligand nucleus can significantly influence the resulting value of the effective distance of the dipolar hyperfine interaction. This is practically illustrated in Fig. 2.1 where ligand centered contribution enhances or diminishes the dipolar hyperfine coupling. For relaxation rates, this dependence is even stronger since HFI enters in square in eqs. (2.6-2.9) thus resulting in $1/r^6$ dependence. It is useful to decompose the dipolar HFI into a point-dipole and a ligand-centered contribution:

$$\overleftrightarrow{\mathbf{T}} = \overleftrightarrow{\mathbf{T}}^{PD} + \overleftrightarrow{\mathbf{T}}^{LC} \quad (2.11)$$

Several simplifications have been proposed in the literature for the analysis of ligand-centered contributions [65–67]. However, all these models were intrinsically linked to specific chemical systems. The approach presented below is free from specific approximations and still provides a clear insight into relations between the dipolar HFI tensor and $\overleftrightarrow{\mathbf{T}}^{PD}$.

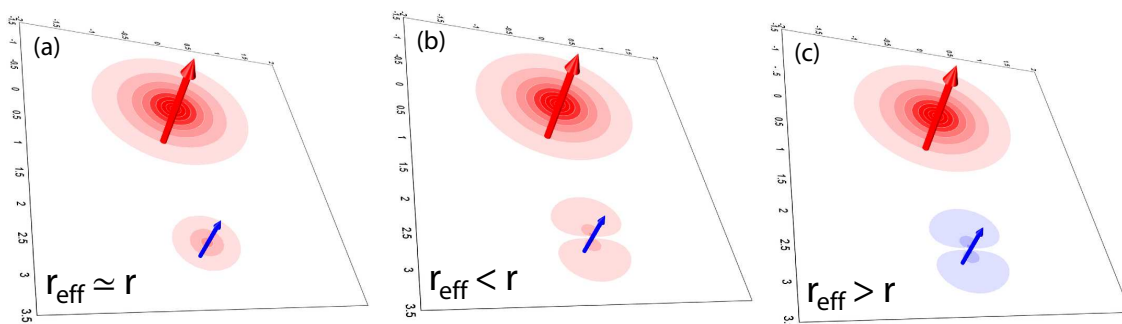


Figure 2.1: Demonstration of possible effects of spin distribution in paramagnetic metal complexes on the ligand dipolar HFI. While in all three cases the majority of the electron spin (red arrow) density is distributed on the distant metal ion, the local spin density distribution in the vicinity of the ligand nucleus spin (blue arrow) may have little effect (a), enhance (b) or diminish (c) the overall dipolar HFI.

2.3 Computational approach

The two-stage computational strategy has been applied to calculate dipolar HFI tensors. In the first stage, we studied as model compound $[\text{Gd}(\text{H}_2\text{O})_8]^{3+}$ with a square

antiprismatic coordination polyhedron of D_{4d} symmetry (Figure 2.2). The geometry of the system is the same as described by Borel *et al.* [68] except for the Gd–O distance which was fixed to 2.40 Å for the sake of better agreement with experimental studies of Gd^{3+} in aqueous solution [69]. Due to the small size and high symmetry of the aquaion, quantum chemical calculations of the complex are rather undemanding. That allowed us to perform a very detailed study of the influence of the basis set quality and other computational aspects on the HFI tensor.

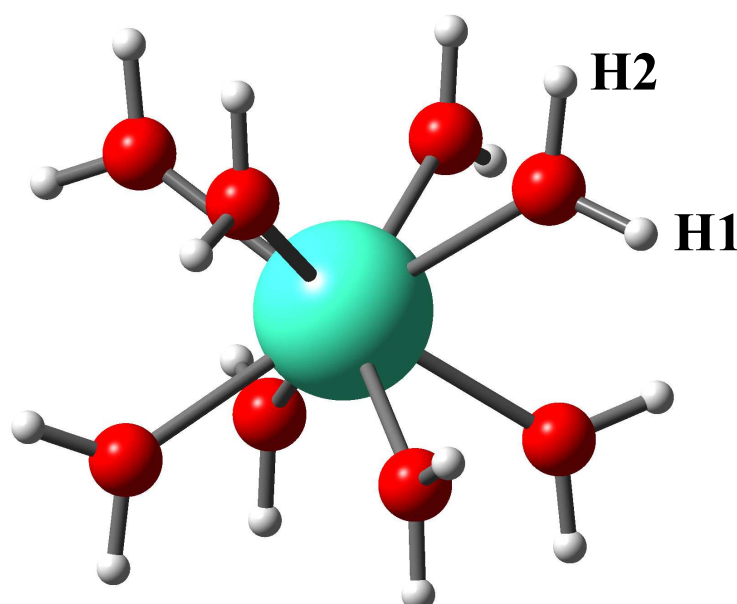


Figure 2.2: The structure of the model Gd^{3+} octa aqua complex of D_{4d} symmetry. The four-fold symmetry axis is aligned to be vertical.

The second stage involves a study of the $[\text{Gd}(\text{DOTA})(\text{H}_2\text{O})]^-$ complex in aqueous solution. To take into account solvent effects and to provide sufficient statistical averaging of the calculated HFI tensor we used a cluster method (see Chapter 11 in Ref. [62] and references therein). This approach implies the ensemble averaging of a property calculated for a set of single configurations (often referred to as “snapshots”) extracted from a molecular dynamics simulation trajectory. This approach has been proven to be reasonable for studying properties such as NMR chemical shifts [70], nuclear quadrupolar coupling constants [71, 72], hyperfine coupling constants [73], and g -tensors [74] of fluids and biosystems in solution. We applied this approach to investigate an extended system

including almost 100 atoms with the focus on the Gd^{3+} ion in the complex and on the water molecule directly bound to it.

A classical molecular dynamics simulation of the $[\text{Gd}(\text{DOTA})(\text{H}_2\text{O})]^-$ complex in water has been performed in a periodic box containing the complex anion, Jorgensen TIP3P water molecules [75], and a Na^+ counterion using Amber 6.0 code [76] ($T=300$ K, $P=1$ atm, NPT ensemble). The parametrization of $[\text{Gd}(\text{DOTA})(\text{H}_2\text{O})]^-$ and the details of the simulation have been extensively described [77, 78]. It is known from experiment that the $[\text{Gd}(\text{DOTA})(\text{H}_2\text{O})]^-$ complex is present in solution as a mixture of major **M** (80%) and minor **m** (20%) conformers with different coordination polyhedra and ligand conformations [79]. Only the major **M** isomer has been simulated and was therefore considered in the present study. The configuration space sampling (100 snapshots) was extracted from the trajectory at regular intervals of 10 ps. The time series of geometric parameters and calculated properties show no autocorrelation. The single configuration (cluster) for quantum chemical calculations consisted of the $[\text{Gd}(\text{DOTA})(\text{H}_2\text{O})]^-$ complex and the 6 second sphere water molecules closest to the inner sphere water molecule (74 atoms in total). Including second sphere water molecules ensures an adequate treatment of close-range solvent effects. Moreover, using the polarizable continuum model (PCM) calculations, we found that far-range solvent effects do not significantly influence the hyperfine coupling constants of the first coordination sphere water molecule. We neglected therefore in our quantum chemical calculations long-range solvent effects, and all calculations were performed for isolated clusters chosen from the snapshots. A typical example of a single configuration is shown in Figure 2.3.

Calculations of lanthanide compounds along with those of other heavy elements require an adequate treatment of relativistic effects [80]. In general, there are few alternative ways to treat relativistic effects. Usually one has to choose between all-electron treatment (including only scalar or both scalar and spin-orbit relativistic effects) and relativistic effective core potentials (RECP), which themselves can also be pure scalar or include also the spin-orbital part. The use of RECP can significantly reduce computational efforts since core electrons are removed and replaced by an effective operator. Several RECP parametrizations for gadolinium [81, 82] are available for routine applications. These pseudopotentials were proven to reproduce reliably experimental molecular geometries and vibrational spectra of gadolinium compounds [83, 84]. However, we found that for HFI tensor calculations all-electron treatments are much better than RECP approaches we considered. Particularly, with some RECPs we encountered severe problems

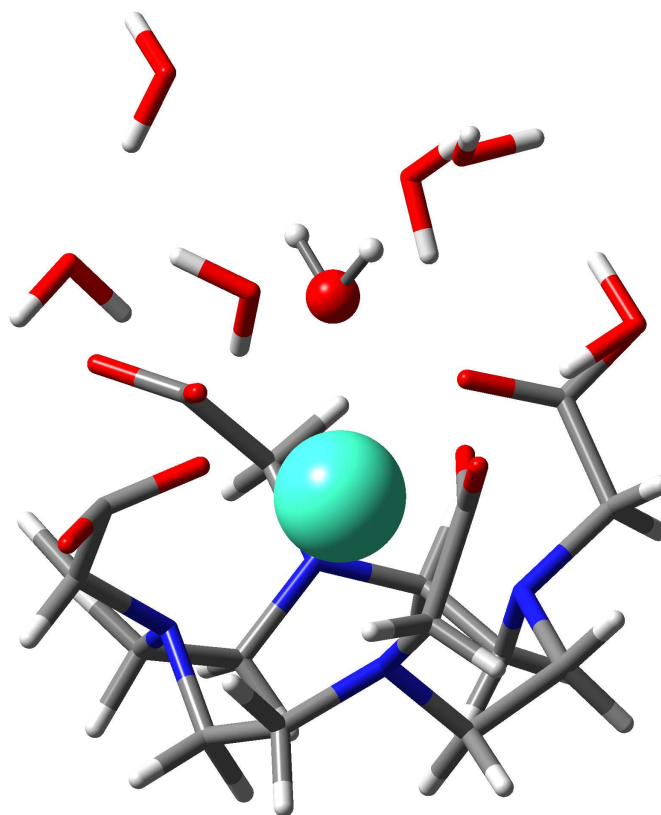


Figure 2.3: A typical “snapshot” extracted from MD simulation of $[\text{Gd}(\text{DOTA})(\text{H}_2\text{O})]^-$. The Gd^{3+} ion and first coordination sphere water molecule are shown in balls and sticks; the polyaminocarboxylate ligand DOTA and 6 second coordination sphere water molecules are presented as tubes.

with the SCF convergence. In other cases, our RECP calculations did not reproduce even the sign of spin-density on ligands. Therefore, in the following we will only discuss the results of all-electron approaches.

Currently, the family of Douglas-Kroll-Hess (DKH) [85] transformation based methods and zero order regular approximation (ZORA) [86, 87] are the methods most widely tested and used among the all-electron relativistic approaches. In a first stage of our computational study we compare second order Douglas-Kroll-Hess method (DKH2) implemented in the `Gaussian03` suite of programs [88] with the ZORA method available in `ADF2003` package [89]. For consistency the point-nucleus model was used in both methods (this is a good approximation in the present study since we are interested in HFI tensors on ligand nuclei only). Spin-orbit coupling terms were not taken into account since

they were not expected to be important for HFI tensor calculations due to the electronic structure and the high coordination (8 or 9) of Gd^{3+} in the compounds under study. In addition, only minor effects were found by recent calculations of spin-orbit corrections to HFI tensor for lighter nuclei [90, 91].

The choice of basis set becomes a nontrivial task considering the calculations of isotropic hyperfine coupling constants. There are two main problems associated with basis sets in such calculations. First, the accurate representation of nuclear cusp is necessary for evaluation of spin density at the point of nucleus. While this can be naturally covered using Slater type orbital (STO) basis sets, extra tight exponents are needed for Gaussian type orbital (GTO) basis sets. Second, it is not sufficient to use large contractions (in the case of GTO basis sets) for the description of the core region because additional flexibility is required to take into account spin-polarization effects [92, 93]. Therefore, the core basis functions have to be considerably uncontracted if GTO basis sets are used or simply represented by a sufficient number of functions of STO basis sets. The frozen core approximation is unacceptable in calculations of HFI if the core MOs are frozen on the nucleus of interest. In the present study, we used both GTO and STO basis sets for the calculations of the model Gd^{3+} octa aqua complex. The GTO set used in all DKH2 calculations was composed from relativistic basis sets of Nakajima *et al.* [94] by complete uncontraction and, in addition, for the light atoms, it was augmented with the polarization functions from the IGLO-III basis set [95]. In ZORA calculations on $[\text{Gd}(\text{H}_2\text{O})_8]^{3+}$ we used the standard TZ2P STO basis set from the ADF package. However, here the concept of basis set “of high local quality” [96] (locally dense basis set) was used in order to reduce the amount of computational resources required. In our case the TZ2P basis set was used only for the part of interest, Gd^{3+} and first coordination sphere water molecules, while the rest of the system was treated using the DZ basis set with frozen $1s$ core. On Gd the frozen core up to the $4d$ shell was used while no frozen core approximation was employed for the atoms of first coordination sphere water molecules. Using model calculations we showed that this approximation does not affect superhyperfine coupling constants on the ligand nuclei.

While most quantum chemical calculations are nowadays performed with the DFT approach, the question about its performance in calculations of a particular property is not an easy one. DFT for calculations of HFI of organic radicals gives acceptable results, and good accuracy can be achieved with pure density functionals except for some pathological cases. However, transition metal complexes are much more difficult

to calculate, and some pictorial failures of pure density functionals are known [97]. For instance, DFT tends to overestimate the coordination bond covalency in Cu^{2+} , which in turn leads to a more delocalized character of SOMO in such systems. Moreover, there is no a priori known best exchange-correlation functional for calculation of hyperfine coupling constants: all GGA functionals behave more or less similarly while hybrid density functionals usually give better results [92,97]. The use of hybrid density functionals (especially with a large admixture of HF exchange) increases, however, spin contamination, which could lead to inferior results [92]. The electronic structure of lanthanide compounds differs significantly from *d*-transition metal complexes: the core character of unpaired *f*-shell electrons makes an admixture of excited states energetically unfavorable. Thus, in principle, an admixture of the Hartree-Fock exchange should not lead to severe spin-contamination. The question about the performance of DFT for the description of spin-polarization driven effects on HFI tensor in lanthanides is still unexplored, and we present here a first attempt of such benchmark calculations. Among available exchange-correlation density functionals the exchange functional of Becke [98] and the correlation functional of Perdew and Wang [99] (this combination is known as the BPW91 functional) were chosen relying on benchmark calculations from Munzarová *et al.* [92]. Thus we used BPW91 as a pure DFT functional, B3PW91 [100] as its hybrid modification, and the Hartree-Fock method for completeness of the consideration. All methods were used in their spin-unrestricted implementation necessary to take into account spin-polarization effects.

2.4 Results and Discussion

2.4.1 Hyperfine couplings in gadolinium aqua complex

The detailed calculations on the small model $[\text{Gd}(\text{H}_2\text{O})_8]^{3+}$ allowed us to assess the reliability of density functional theory calculations of HFI for Gd complexes. The obtained isotropic ^{17}O hyperfine coupling constants (HFCC) (Table 2.1) are between 0.61 and 1.02 MHz for the DFT calculations. An admixture of the HF exchange to the exchange-correlation potential (B3PW91 vs. BPW91) pushes the calculated ^{17}O HFCC in the direction of the HF results, which is not unexpected. The difference between ZORA and DKH results for isotropic ^{17}O HFCC can be attributed to the neglect of so called picture-change effect in present DKH calculations. Taking into account that, due to a very local

character of the Fermi contact operator, the isotropic constants are very difficult to evaluate computationally, the results show reasonable mutual agreement. Furthermore, the DFT calculations are consistent with the experimental values of 0.84 MHz [18, 101] and 0.71 MHz [102] for $[\text{Gd}(\text{H}_2\text{O})_8]^{3+}$. Our model calculations do not include long-range solvent effects which are expected to be insignificant for HFI. Therefore, both pure and hybrid density functionals look reliable to describe ligand nuclei HFI in the compounds studied. The positive isotropic HFCC, A_{iso} , on ^{17}O nuclei corresponds to a negative spin-density at the point of the O nucleus of $-0.0118 \text{ a.u.}^{-3}$ while the most negative value of spin-density within cross sections shown in Figure 2.4 is $-0.1342 \text{ a.u.}^{-3}$.

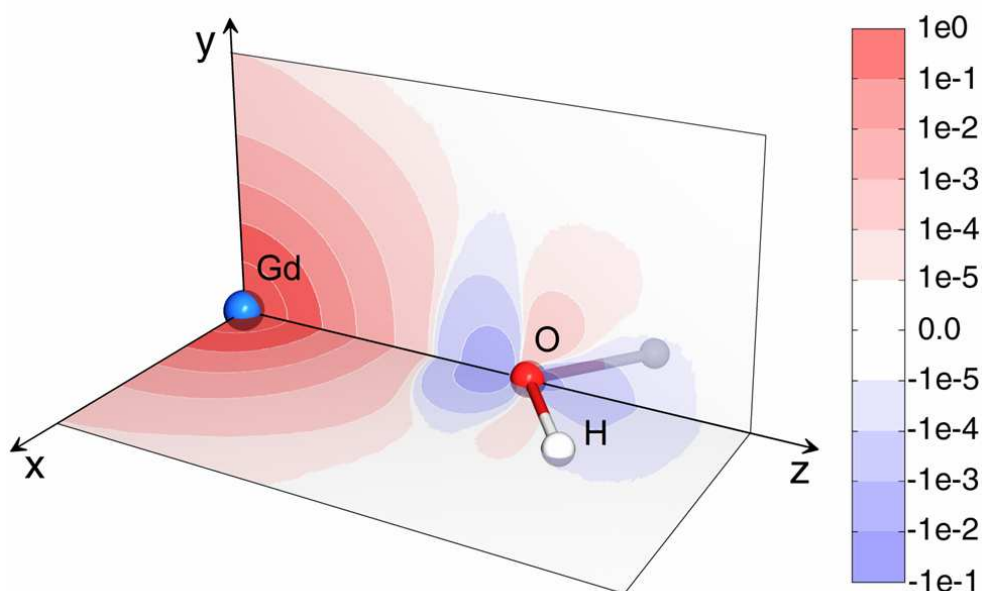


Figure 2.4: Spin density map of the $[\text{Gd}(\text{H}_2\text{O})_8]^{3+}$ model system (calculated at the BPW91/DKH2/Hirao level of theory, in a.u.^{-3}) shows the Gd^{3+} ion and one of the water molecules. Cross sections of size $2 \times 4 \text{ \AA}$ in XOZ and YOZ planes are shown.

The calculated T_{zz} values (Table 2.1) of the ^{17}O HFI anisotropy tensor are noticeably lower (about -1.35 MHz) than predicted by the point-dipole approximation (-1.55 MHz) using eq. 2.5 and $r_{\text{Gd-O}} = 2.40 \text{ \AA}$. All quantum chemical methods used in this study give results in good mutual agreement, which is not surprising since it is well-known that HFI anisotropy is much less sensitive to the computational aspects than the isotropic part [62]. Again this excellent agreement supports our confidence in using the DFT method in the calculations of HFI on ligand nuclei in lanthanide compounds. The rhombicity of

HFI anisotropy tensor, $T_{xx}-T_{yy}$, depends on the choice of quantum chemical method. The pure density functional BPW91 yields the largest positive $T_{xx}-T_{yy}$ values (0.242 and 0.178 MHz) as a consequence of possible residual π -binding involving f -electrons. This is not surprising since pure density functionals are known to overestimate the covalency of coordination bond. However, for Gd^{3+} the rhombicity influences only slightly the effective distance r_{eff} (eq 10), which is almost solely defined by the T_{zz} value. Our calculations of the HFI anisotropy tensor are in qualitative agreement with the estimations of Raitsimring *et al.* [103]. In their calculations they estimate the spin population of the whole $s-p_z$ hybrid orbital of the O atom from the experimental isotropic ^{17}O HFCC and neglect any valence shell and core shell spin-polarization effects. We have shown recently (see Chapter 4) that these effects might be significant and can be taken into account within quantum chemical calculations [104].

The calculated ^1H isotropic hyperfine couplings are very small (Table 2.1). The increase of amount of exact exchange tends to decrease spin density at ^1H nucleus and even to change its sign. This can be attributed to the fact that the hydrogen atoms lie very close to a node of the spin-density surface (see Figure 2.4). The calculated ^1H HFI anisotropy tensors are in very good agreement with each other and with the point-dipole approximation. All tested quantum chemistry methods give a negligible ligand-centered contribution to the ^1H HFI tensor.

The basis sets used in our calculations are sufficient since calculated HFCCs do not show significant changes upon the addition of extra basis functions. The purity of spin states is proved by calculated $\langle S^2 \rangle$ values (for DFT methods we use Kohn-Sham determinant to evaluate $\langle S^2 \rangle$). For BPW91, B3PW91, and HF calculations with GTO basis set the calculated values of $\langle S^2 \rangle$ are 15.7556, 15.7556, and 15.7576, correspondingly, while the nominal value for a pure octet state is 15.75.

Table 2.1: Calculated ^{17}O and ^1H hyperfine tensors for the first coordination sphere water molecules of the $[\text{Gd}(\text{H}_2\text{O})_8]^{3+}$ model system.^a

method	A_{iso} (MHz)	T_{xx} (MHz)	T_{yy} (MHz)	T_{zz} (MHz)	r_{eff} (Å)
^{17}O					
BPW91/ZORA/TZ2P	0.61	0.802	0.560	-1.362	2.50
BPW91/DKH2/Hirao	0.78	0.761	0.583	-1.344	2.51
B3PW91/DKH2/Hirao	1.02	0.716	0.633	-1.349	2.51
HF/DKH2/Hirao	1.60	0.681	0.671	-1.352	2.51
exp./point-dipole ^b	0.84	0.775	0.775	-1.551	2.40
^1H					
BPW91/ZORA/TZ2P	0.022	-2.652	-2.652	5.277	3.105
	0.028	-2.651	-2.626	5.277	3.106
BPW91/DKH2/Hirao	-0.001	-2.655	-2.623	5.278	3.105
	0.009	-2.653	-2.623	5.275	3.106
B3PW91/DKH2/Hirao	-0.031	-2.666	-2.618	5.283	3.104
	-0.023	-2.663	-2.618	5.281	3.105
HF/DKH2/Hirao	-0.044	-2.677	-2.606	5.283	3.104
	-0.029	-2.674	-2.607	5.280	3.105
exp./point-dipole ^b	0.03 ± 0.02	-2.643	-2.643	5.287	3.1037

^a Two different values for ^1H correspond to two types of protons in the model system. H1 and H2 protons as shown in Figure 2.2 belong to the same water molecule and are equivalent for different water molecules. H1 protons are equatorial and H2 are axial with respect to the symmetry axis. The Gd-H1 and Gd-H2 distances are equal.

^b r_{eff} obtained using the point-dipole approximation.

Table 2.2: Comparison of calculated (BPW91/ZORA/ TZ2P) and experimental hyperfine interaction parameters for $[\text{Gd}(\text{H}_2\text{O})_8]^{3+}$ and $[\text{Gd}(\text{L})(\text{H}_2\text{O})]^{n-}$.^a

	$[\text{Gd}(\text{H}_2\text{O})_8]^{3+}$		$[\text{Gd}(\text{L})(\text{H}_2\text{O})]^{n-}$	
	calc.	exp.	calc. ^b	exp.
¹⁷ O				
$r_{\text{Gd}-\text{O}}$ (Å) ^c	2.4		2.56 (0.06)	
r_{eff} (Å) ^d	2.50		2.72 (0.06)	
A_{iso} (MHz)	0.61	0.79 ^e	0.58 (0.11)	0.59 ^h
		0.84 ^f		0.75 ⁱ
		0.75 ^g		
T_{xx} (MHz)	0.802	0.76 ^{g,1}	0.623	0.76 ⁱ
T_{yy} (MHz)	0.560	0.62 ^{g,1}	0.452	0.62 ⁱ
T_{zz} (MHz)	-1.362	-1.38 ^g	-1.061 (0.09)	-1.38 ⁱ
¹ H				
$r_{\text{Gd}-\text{H}}$ (Å) ^c	3.1037		3.27 (0.14)	
r_{eff} (Å) ^d	3.106	3.09 ^j	3.27 (0.14)	
A_{iso} (MHz)	0.025	0.04 ^e	-0.032 (0.08)	-0.04 ^k
		0.03 ^j		
T_{xx} (MHz)	-2.652	-2.67 ^j	-2.306	-2.75 ^k
T_{yy} (MHz)	-2.626	-2.67 ^j	-2.256	-2.75 ^k
T_{zz} (MHz)	5.277	5.34 ^j	4.562 (0.66)	5.5 ^k

^a The distribution widths from molecular dynamics sampling are given in parentheses.

^b L = DOTA.

^c Nuclear distance.

^d Effective distance of dipole-dipole interaction.

^e From NMR chemical shift (Ref. [102]), corrected for coordination number of 8.

^f From NMR chemical shift (Ref. [18]).

^g From ENDOR experiments (Ref. [105]).

^h L = DOTA, NMR chemical shift (Ref. [18]).

ⁱ L = MS-325, ENDOR experiments (Ref. [103]).

^j From ENDOR (Ref. [105]).

^k L = HPDO3A, ENDOR experiments (Ref. [105]).

¹ From the estimated rhombicity of 0.14 MHz for the planar model 2 (Ref. [103]).

The qualitative inspection of spin density maps presented graphically in Figure 2.4 shows the strong spin-polarization effect on the water molecule. While most of the positive spin density resides on the Gd^{3+} ion itself, electron density along Gd–O bond is significantly spin-polarized, leading to two important consequences. Firstly, the calculated T_{zz} value (OZ axis is oriented along Gd–O bond) of -1.35 MHz for ^{17}O (Table 2.1) is noticeably lower than the value of -1.55 MHz predicted by the point-dipole approximation (eq. 2.5). This reduction of the T_{zz} value leads to an effective distance of $r_{eff}=2.50$ Å for the dipole-dipole interaction (eq. 2.10), which is considerably longer than the Gd–O internuclear distance $r_{\text{Gd-O}}=2.40$ Å (Table 2.2). One can think about this effect as a partial compensation of magnetic dipole-dipole interaction between the positive spin-density on the Gd^{3+} ion and the ^{17}O nucleus by the negative spin-density induced on the ligand. Furthermore, it is interesting to note the positive spin density located in the YOZ plane perpendicular to the plane of the water molecule (Figure 2.4). This is reflected in the bigger value of $T_{xx}-T_{yy}$ for BPW91 calculations and can be a consequence of some residual π -binding involving f -electrons or a spin alternation effect. However, as it was discussed above, the small rhombicity of the oxygen HFI anisotropy tensor has negligible influence on the resulting value of the effective distance of dipolar interaction $r_{eff}(\text{Gd-O})$. Secondly, the ^{17}O isotropic hyperfine coupling constant, A_{iso} , is positive as the consequence of a negative spin density at the oxygen nucleus and the negative magnetic moment of the ^{17}O nucleus. As we already mentioned in the beginning of this section, the experimental values of 0.71 MHz [102] and 0.84 MHz [101] lie within the $0.61-1.02$ MHz range of DFT predictions (Table 2.1).¹ The magnitude of the coupling is relatively small since the $s-p_z$ hybrid atomic orbital of O, which is mostly affected by spin-polarization, has little of s -character and therefore its node lies very close to the nucleus.

The Gd–H effective distance of dipole-dipole magnetic interaction recalculated via data of quantum chemical calculations (Table 2.2) is only slightly bigger than the distance between the nuclei, $r_{\text{Gd-H}}$. The point-dipole approximation is therefore valid for hydrogens of water molecules in $[\text{Gd}(\text{H}_2\text{O})_8]^{3+}$. The validity of this approximation for ^1H was found in a previous study on dipolar HFI in d -transition metal aqua ions [55]. The rationalization of this observation is that p -type atomic orbitals on hydrogen play only a

¹Please note: There is some confusion about the sign of the ^{17}O isotropic HFCC in Gd^{3+} complexes. In contrast to recent experimental work the correct sign of $A_{iso}=A/h$ of a water molecule bound to Gd^{3+} is positive (corresponding to negative spin density at the point of nucleus), leading to a downfield shift of the ^{17}O resonance.

minor role in bonding (and thus could not contribute significantly to the anisotropy of the HFI tensor) whereas the s -type atomic orbital gives zero contribution to the anisotropy of the tensor (but determines the isotropic constant A_{iso}).

The calculated ^1H isotropic hyperfine couplings are close to zero and in good agreement with experimental data. For instance, single-crystal EPR studies [106] put this value between -0.015 and $+0.04$ MHz while the most reliable ENDOR [105] gives $+0.03\pm 0.02$ MHz. Bryden *et al.* [107] deduced ^1H HFCC from NMR data to be about 0.005 MHz. We conclude that there is rather large uncertainty in the experimental data due to the small absolute magnitude of the coupling.

2.4.2 Hyperfine couplings in GdDOTA

The isotropic ^{17}O HFCCs obtained using the DFT cluster approach with averaging over a set of snapshots selected from a classical molecular dynamic simulation are in a very good agreement with experimental data. A major parameter influencing the ^{17}O HFCC is the Gd–O distance, $r_{\text{Gd-O}}$, which fluctuates during the molecular dynamics simulation. Figure 2.5a shows the isotropic hyperfine coupling constant as a function of $r_{\text{Gd-O}}$. The averaged $A_{iso}(\text{O})$ is 0.58 MHz (standard deviation: 0.11 MHz) for an average distance of 2.56 ± 0.06 Å; that is in excellent agreement with the value of 0.59 ± 0.03 MHz determined from ^{17}O NMR chemical shift data [18]. In all geometric configurations obtained from the snapshots the spin density at the position of oxygen nucleus is negative in accord with the spin-polarization mechanism. The magnitude of $A_{iso}(\text{O})$ strongly correlates with the Gd–O distance and the spin-polarization effect decays rapidly with the increase of $r_{\text{Gd-O}}$. The mean Gd–O distance from the classical MD simulation is however about 0.1 Å longer than that of the solid-state X-ray [108] or the solution XAFS structure [109]. ^{17}O electron nuclear double resonance spectra of the MS-325, a Gd^{3+} complex with an acyclic ligand, recorded in frozen solution, gave spectra of a shape similar to that of the Gd^{3+} aqua ion [103]. The authors concluded therefore that the ^{17}O hyperfine coupling parameters of both complexes are the same, $A_{iso}=0.75$ MHz.

The calculated mean value of the ^1H isotropic hyperfine coupling constant (-0.032 ± 0.08 MHz) is very small and varies from about -0.2 to $+0.1$ MHz (Figure 2.5b). Again a strong correlation with the Gd–H distance is observed. The corresponding NMR experimental value of Bryden *et al.* [107] for $[\text{Gd}(\text{DOTA})(\text{H}_2\text{O})]^-$ is about 0.075 MHz while the 2D Mims ENDOR result [105] for $[\text{Gd}(\text{HP-DO3A})(\text{H}_2\text{O})]^-$ is -0.04 ± 0.02 MHz.

Regarding the slightly longer Gd–H average distance from the MD simulations ($r(\text{Gd-H})=3.27 \text{ \AA}$ compared to 3.1 \AA from ENDOR) the agreement between calculated and experimental $A_{iso}(\text{H})$ is also very satisfactory.

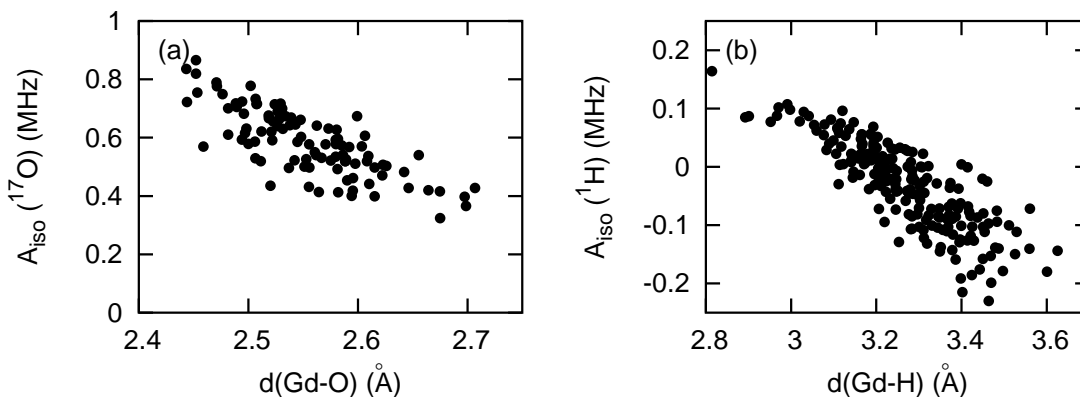


Figure 2.5: ^{17}O (a) and ^1H (b) hyperfine coupling constant, A_{iso} , plotted as function of Gd–O(H) distance for 100 configurations extracted from MD trajectory of $[\text{Gd}(\text{DOTA})(\text{H}_2\text{O})]^-$.

We express the results of anisotropic HFCCs in terms of effective distances of dipole-dipole interactions, r_{eff} (eq. 2.5). understanding. It allow us to compare the results of the calculations with those obtained within the point-dipole approximation. Figure 2.6 shows the values of the r_{eff}^{-6} factor as function of the Gd-ligand nucleus distances. The values of r_{eff}^{-6} , obtained from eq. 2.10, are based on the calculated dipolar HFI tensors for 100 MD snapshots. The point-dipole approximation used in the SBM equations uses internuclear distances $r_{\text{Gd-X}}$, and the corresponding factors $r_{\text{Gd-X}}^{-6}$ are shown as dashed lines in Figure 2.6.

From Figure 2.6a it can be seen that for ^{17}O the point-dipole approximation significantly overestimates the dipolar interaction between the ligand nuclear spin and the electron spin of the ion: The expectation value of the effective distance factor for dipolar relaxation is $\langle r_{eff}^{-6}(\text{Gd-O}) \rangle = 2.51 \times 10^{-3} \text{ \AA}^{-6}$ compared to the internuclear gadolinium-oxygen distance of $\langle r^{-6}(\text{Gd-O}) \rangle = 3.64 \times 10^{-3} \text{ \AA}^{-6}$. This corresponds to the following average distances of dipole-dipole magnetic interactions: $\langle r_{eff}(\text{Gd-O}) \rangle = 2.72 \text{ \AA}$ and $\langle r(\text{Gd-O}) \rangle = 2.56 \text{ \AA}$, respectively. Neglecting spin-polarization effects leads therefore to an overestimation of the dipolar ^{17}O nuclear spin relaxation rates by approximately 45%.

The point-dipole approximation is however valid to describe the anisotropic HFI between Gd^{3+} and ^1H of the inner sphere water molecule in $[\text{Gd}(\text{DOTA})(\text{H}_2\text{O})]^-$. From Figure 2.6b one can note that $r_{eff}^{-6}(\text{Gd-H})$ deviates only very slightly from $r^{-6}(\text{Gd-H})$ at

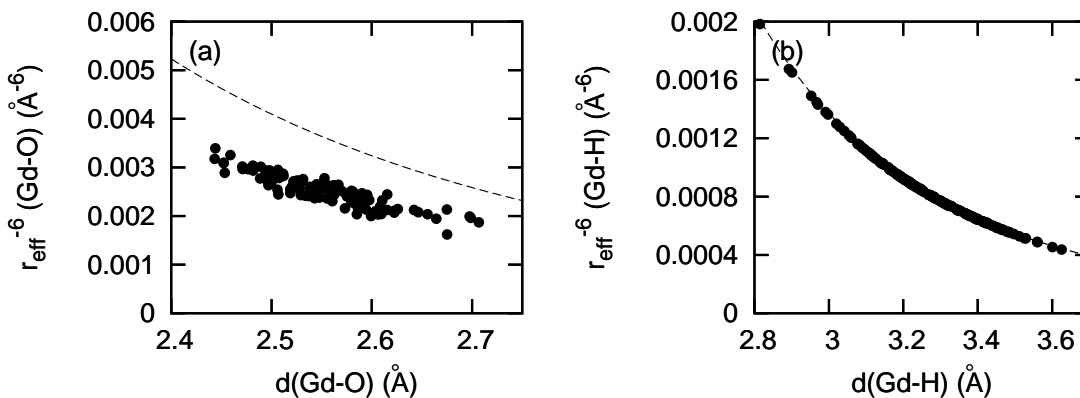


Figure 2.6: The $r_{eff}^{-6}(\text{Gd-O})$ (a) and $r_{eff}^{-6}(\text{Gd-H})$ (b) factors for the oxygen and hydrogen atoms of bound water in $[\text{GdDOTA}(\text{H}_2\text{O})]^-$ obtained from eq. 2.10 based on the calculated dipolar HFI tensors of the 100 MD “snapshots”. The dashed lines corresponds to $r^{-6}(\text{Gd-O})$ and $r^{-6}(\text{Gd-H})$, respectively, calculated using the point-dipole approximation.

short Gd–H distances and the average values are virtually identical: $\langle r_{eff}^{-6}(\text{Gd-H}) \rangle = 8.48 \times 10^{-4} \text{\AA}^{-6}$ and $\langle r^{-6}(\text{Gd-H}) \rangle = 8.56 \times 10^{-4} \text{\AA}^{-6}$.

2.5 Practical conclusions

The study of physicochemical parameters of gadolinium based MRI contrast agents is to a large extent based on ^1H and ^{17}O NMR relaxation measurements. The strong interaction between the nuclear spins and the electron spin of Gd^{3+} dominates the relaxation properties and allows the determination of rotational correlation times and water exchange rates, for example. Thus, an accurate knowledge of the isotropic and anisotropic parts of the hyperfine coupling constant is imperative for an accurate assessment of the data.

Our quantum chemical investigation of hyperfine coupling constants between Gd^{3+} ion and bound water molecules shows that the ^1H isotropic hyperfine coupling constants, A_{iso} , are small. Thus, the contribution of scalar relaxation to the relaxation enhancement can therefore be safely neglected as it has already been deduced from experimental data. What is more essential, the evaluation of the anisotropic part of the A-tensor shows that the point-dipole approximation is valid for ^1H NMR of bound water molecules. The distance $r_{\text{Gd-H}}$ introduced in SBM theory can therefore be safely set to the distance between the gadolinium and the proton nuclei.

Reduced transverse ^{17}O NMR relaxation rates $1/T_{2r}$ are, in the case of Gd-based

complexes, dominated by the scalar relaxation mechanism which depends on A_{iso} . This isotropic hyperfine coupling constant can be best determined experimentally by ^{17}O NMR shift measurements. Our calculated $A_{iso}(\text{O})$ strongly correlates with the metal-oxygen distance, and therefore, NMR shift measurements give at least a qualitative indication for $r_{\text{Gd-O}}$: smaller coupling constants are indicative for longer Gd–O distances.

Reduced longitudinal ^{17}O NMR relaxation rates, $1/T_{1r}$, are controlled to about two-thirds by the dipolar contribution, $1/T_1^{DD}$, and to about one-third by the quadrupolar contribution, $1/T_1^Q$ [45]. The quantum chemical evaluation of the anisotropic HFI tensor $\overleftrightarrow{\mathbf{T}}$ has shown that spin-polarization effects play an essential role for proper evaluation of ^{17}O HFI tensor. The point-dipole approximation, based on internuclear distances, significantly overestimates the interaction between electron and ^{17}O nuclear spin. To compensate for the 45% decrease of $1/T_1^{DD}$ by using the correct distance for dipolar interaction (2.72 Å instead of 2.46 Å) a 25% increase of the rotational correlation time τ_R is needed.

Chapter 3

^{17}O quadrupole couplings in gadolinium aqua complexes

3.1 Introduction

In the previous Chapter we considered magnetic the coupling electron spins and nuclear spins in the system by means of hyperfine interactions. Another important contribution to the effective spin Hamiltonian is the quadrupole interaction which couples nuclei with spin $I \geq 1$ with the electric field gradient (EFG) at the nucleus [110–112]. In an anisotropic phase this coupling leads to a quadrupole fine structure showing $2I$ equidistant lines with a separation proportional to the EFG. In an isotropic phase the EFG averages out and only a single resonance is observed. Rapid molecular motions lead to stochastic fluctuations of the EFG inducing transitions between the spin levels. Spin relaxation of quadrupole nuclei is therefore due to fluctuations of the magnetic field and of the EFG, although the later mechanism is generally dominating.

The electric field gradients at the nucleus are due to the total intra- and intermolecular charge distribution around the nucleus. If a quadrupole nucleus is a part of a molecule, EFG is mainly of intramolecular nature and fixed in the molecular frame of reference. Its time fluctuation comes mainly from the rotational motion of the molecule. For monoatomic species the EFG has an intermolecular origin. In the electrostatic approach for intermolecular quadrupole relaxation the EFG is generated by surrounding electric multipoles [113–116]. The relation between nuclear quadrupole relaxation and the correlation time characterizing molecular tumbling, τ_R , is particularly simple in case of fast tumbling (extreme narrowing, $\omega\tau_R \ll 1$, with ω being the resonance frequency

in rad s^{-1}). This makes it an ideal tool to determine τ_R , provided the EFG is known. Oxygen-17 NMR has been successfully used in recent years to study poly amino carboxylate complexes of gadolinium(III) used as contrast agents in medical magnetic resonance imaging (MRI) [45]. Transverse ^{17}O relaxation rates have become the most important source for water exchange rate constant on these complexes. Longitudinal ^{17}O relaxation rates provide an easy and relatively direct method to determine rotational correlation times for the Gd–O vector which are in general equal to τ_R of the complex.

In the last decade several research groups used quantum chemical calculations to determine quadrupole coupling parameters which combine electric field gradients and the electric quadrupole moment of the nucleus [62, 71, 72, 117–128]. The rotational correlation time of water molecules in coordination compounds can be determined by measuring ^{17}O relaxation rates of bound water molecules. The use of ^2H , which is also a quadrupole nucleus, is in general prohibited because it exchanges rapidly with those on surrounding water molecules. The biggest effort of both experimental and theoretical research was dedicated to quadrupole coupling parameters of pure water in gas, liquid and solid state. The condensation effects, leading to a difference in quadrupole coupling constants for gas, liquid phase water and ice, are largely understood [62, 72, 120, 124–128]. In contrast, controversial experimental data and no recent theoretical studies were provided for ^{17}O quadrupole couplings for water molecules in metal aqua complexes.

In this Chapter, we investigate electric field gradients on the water molecule oxygen nucleus using density functional theory (DFT) and molecular dynamics (MD) techniques. The implications of our calculations for ^{17}O NMR relaxation studies are discussed.

3.2 Calculation of ^{17}O quadrupole couplings

3.2.1 Theoretical foundations

High spin nuclei ($I \geq 1$) in addition to their magnetic dipole moment possess an electric quadrupole moment. Different nuclear spin projections split in the electrostatic field of surrounding electrons and nuclei according to the following effective spin Hamiltonian operator:

$$\hat{H}_Q(I, I) = \mathbf{I} \cdot \overleftrightarrow{\mathbf{Q}} \cdot \mathbf{I}, \quad (3.1)$$

where $\overleftrightarrow{\mathbf{Q}}$ is the symmetric and traceless nuclear quadrupole coupling tensor. The quadrupole coupling tensor elements, Q_{ij} , are related to the electric field gradient (EFG) tensor elements, $q_{ij} = \partial^2 V(\mathbf{r}_I) / \partial r_i \partial r_j$, as

$$Q_{ij}[\text{MHz}] = -2.3496 \cdot Q[\text{fm}^2] \cdot q_{ij}[\text{a.u.}], \quad (3.2)$$

where $V(\mathbf{r}_I)$ is the electrostatic potential at the point of nucleus I and Q is the nuclear quadrupole moment in fm^2 [71, 121]. Typically, instead of the full quadrupole coupling tensor two simple quantities are used, the quadrupole coupling constant (QCC), $\chi = Q_{zz}$, and the asymmetry parameter, $\eta = (Q_{xx} - Q_{yy}) / Q_{zz}$, where $|Q_{zz}| \geq |Q_{yy}| \geq |Q_{xx}|$ are the principal values of the quadrupole coupling tensor [129]. In this notation, the nuclear relaxation due to quadrupole interaction can be written in the extreme narrowing as

$$\frac{1}{T_{iQ}} = \frac{3\pi^2}{10} \frac{2I + 3}{I^2(2I - 1)} \chi^2 (1 + \eta^2/3) \tau_R, \quad (3.3)$$

where I is the spin quantum number of the nucleus.

3.2.2 Computational methodology

The larger part of the computational methodology used for the EFG calculations has already been described in Chapter 2. In addition to classical MD simulations, in this part of our work we performed also MD simulations based on the density functional theory. The details of these calculations are given below. In spite of the fact that EFG tensors can be calculated directly in pseudopotential based first principles MD simulations (e.g. Ref. [130]), we follow the cluster approach in order to keep the consistency with the classical MD based methodology.

First principles MD simulation of the Gd^{3+} ion in water was performed using the Car-Parrinello technique [131] implemented in the CPMD code [132]. The details of these simulations are described in details later, in Chapter 5.

The cluster configurations were extracted from the classical and first principles MD simulation in the following way. The Gd^{3+} aqua ion clusters contained one ion surrounded with the 24 closest water molecules. The EFG tensors of all first coordination sphere water molecules were calculated. The time interval between extracted snapshots

in classical MD simulation is in this case equal to 4 ps. Because of the limited duration of first principles MD simulation the time interval is equal to 0.25 ps in this case. The total amount of extracted configurations is 14 in both cases, thus, providing 112 EFG tensors for statistical averaging (eight water molecules in the first sphere). The comparative calculations of condensation effects on the quadrupole coupling parameters were also performed using results of both classical and first principles simulations of the same level of theory. The clusters containing the water molecule, on which the EFG tensor is considered, and 17 closest to it water molecules were extracted in this case. The $[\text{Gd}(\text{DOTA})(\text{H}_2\text{O})]^-$ ion contains only one first coordination sphere water molecule. In total 100 configurations were extracted from the classical MD trajectory with a time step of 10 ps. Each configuration consisted of the Gd^{3+} ion, the DOTA ligand, the inner sphere water molecule and 6 second coordination sphere water molecules closest to the inner sphere molecule. This procedure has been previously described in Ref. [104].

3.2.3 Calibration of ^{17}O quadrupole moment

Besides the EFG tensor calculated theoretically in our work, the second physical quantity necessary for the calculation of quadrupole coupling parameters is the quadrupole moment Q of the nucleus. Unfortunately, reported experimental and theoretical values of $Q(^{17}\text{O})$ are rather uncertain and range from about -2.3 fm^2 to -3.0 fm^2 [121]. Moreover, the values of EFG components slightly depend upon the level of theory and basis set used in calculations. To overcome these problems Huber and co-workers proposed a nuclear quadrupole moment calibration procedure [71]. According to this methodology, for a given level of theory the nuclear quadrupole moment is obtained from the calculations performed on a set of small molecules with accurate known experimental QCCs. We exactly reproduce this procedure using a set of 7 small molecules ($\text{C}_2\text{H}_4\text{O}$, OCS , HNCO , H_2CO , O_2 , H_2O and CO). The calculated χ values versus the experimental QCCs are shown in Fig. 3.1. The least-square fit using eq. (3.2) yields the value of $-2.45 \pm 0.05 \text{ fm}^2$ for $Q(^{17}\text{O})$. The R^2 value of the fit is 0.996. Our calibrated value agrees well with the value of -2.558 fm^2 recommended by Pyykkö [133] and the range of values between 2.36 fm^2 and 2.64 fm^2 obtained by Ludwig *et al.* [121] for different post-Hartree-Fock methods and different Gaussian basis sets using the same calibration procedure. The principal components of the ^{17}O EFG tensor of a water molecule at the equilibrium geometry are $q_{zz} = -1.762$ (a.u.), $q_{yy} = 1.523$ (a.u.) and $q_{xx} = 0.238$ (a.u.). The directions of principal

axes of the ^{17}O EFG tensor are shown in Fig. 3.2. Thus, the calculated value of the ^{17}O QCC for the gas-phase water molecule using the calibrated nuclear quadrupole moment is 10.158 MHz which agrees closely with the experimental value of 10.175 MHz [134]. For the water molecule at TIP3P geometry the principal values are $q_{zz} = -1.727$ (a.u.), $q_{yy} = 1.516$ (a.u.) and $q_{xx} = 0.211$ (a.u.) with the same orientation of principal axes. This gives a slightly smaller value of 9.958 MHz for the QCC which still agrees within 2% with the experimental value.

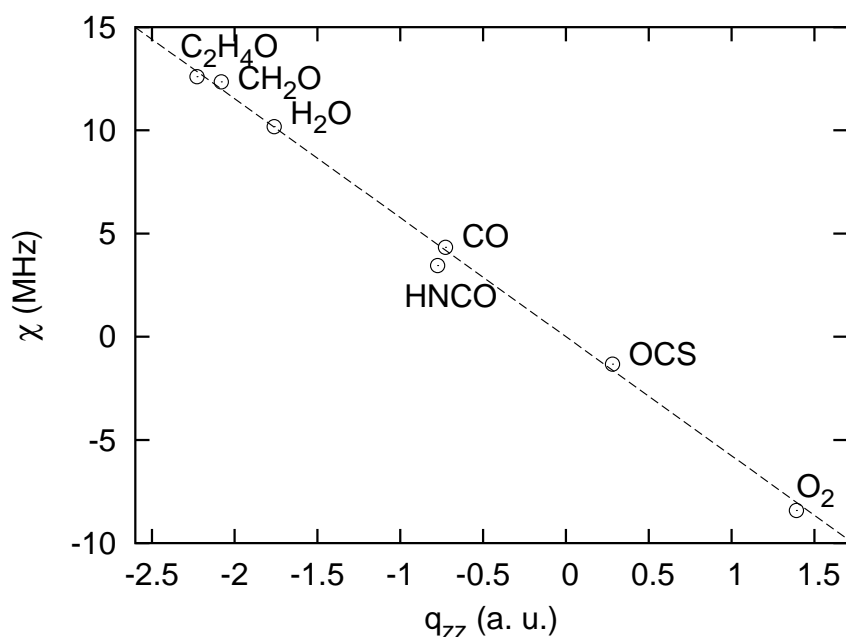


Figure 3.1: Experimental ^{17}O quadrupole coupling constants [71] χ versus calculated values of q_{zz} for the set of small molecules used in the calibration of ^{17}O quadrupole moment. Least-squares fitted line is shown on the graph.

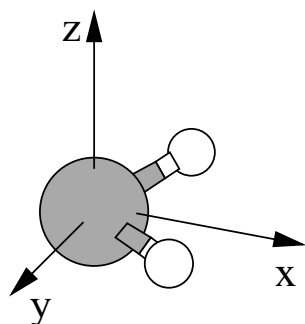


Figure 3.2: Convention on the orientation of principal axes of ^{17}O quadrupole coupling tensor in water molecule.

3.3 Quadrupole couplings in model aqua complexes

In order to investigate the effects of coordination on the ^{17}O quadrupole coupling parameters of a water molecule in the first coordination sphere of a metal ion complex we studied a number of small model systems. Since our computational study models aqua ions in solution, these effects are studied consistently along with hydrogen bonding effects which are always present in water solutions. In cationic complexes the water molecules are always O-coordinated, serving as an electron donor in the coordination bond with the positively charged ion. In hydrogen bonding a water molecule may participate both as donor and acceptor providing its oxygen lone pairs or its hydrogen atoms. These two scenarios are called H_O -bonding and H_H -bonding, correspondingly. We compare effects of ion coordination with those of H_O -bonding. The geometry of H_O -bonded and Gd^{3+} -coordinated systems are shown on Fig. 3.3. The hydrogen bond length is set to 1.8 Å. The model of the $[\text{Gd}(\text{H}_2\text{O})_8]^{3+}$ -complex is described in details in Ref. [104]. The Gd–O distance is chosen to be 2.4 Å in accordance with experimental data [69]. The two O-bonding scenarios are indicated with the Roman numerals **I** and **II**, respectively. The geometry of the water molecule is the geometry of a TIP3P water molecule.

Furthermore, we distinguish three possible ways of O-bonding which are indicated by capital letters in our model nominations. The letter **A** stands for complete absence of O-bonding (**A** is just a TIP3P water molecule). In models indicated with **B** the tilt angle θ (the angle between the bond and the dipole moment vector in isolated water molecule) is 0° . In models indicated with **C** the angle θ is half of the tetrahedral angle (54.74°). Models named **D** differ in respect to models indicated with **C** by the presence of an additional H_O -bond tilted by 54.74° .

Effects of H_H -bonding are investigated in models indicated with a prime ($'$). In these models both hydrogen atoms of the water molecule are H-bonded to other water molecules. In total 14 models were investigated using different combinations of the models described above.

Before discussing the results of the model calculations in detail, it is worth to mention that environmental effects on the largest principal value of the EFG tensor, which is directly linked to χ , have the strongest impact on the value of $\chi\sqrt{1+\eta^2/3}$. In all model systems studied the order of the absolute magnitudes of the EFG tensor principal values remains the same as in an isolated water molecule (Fig. 3.2 and Table 3.1). The orientations of the principal vectors of the EFG tensor do not change significantly. The

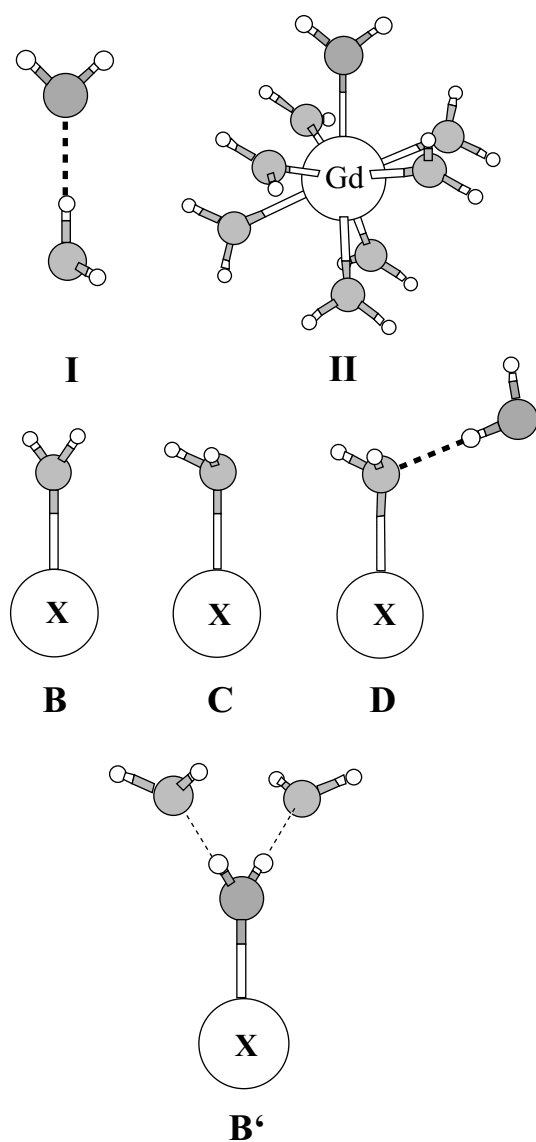


Figure 3.3: Construction of model systems. Top: Configurations of the model H_O -bonded water molecule (**I**) and the first coordination sphere water molecule (**II**) in $[\text{Gd}(\text{H}_2\text{O})_8]^{3+}$. Middle: Three modes of the H_O -bonding and the coordination to Gd^{3+} ion (denoted as **B**, **C** and **D**) in model systems study. **X** refers to either a H_O -bonded water molecule or the $[\text{Gd}(\text{H}_2\text{O})_7]^{3+}$ moiety. Bottom: H_H -bonded configuration (denoted with prime (')) of the water molecule in model systems as example of a **B'** system.

largest deviation of 12° was observed in model **IIC'** for the principal vectors oriented along x - and z -axes. Qualitatively, the effects of coordination bonding and H_O -bonding were found to be very similar. This suggests that in aqua ions ^{17}O quadrupole coupling parameter $\chi\sqrt{1+\eta^2/3}$ should not differ significantly from that of a water molecule in the bulk liquid. In models **IB** and **IIB** the values of χ are very similar to those in the isolated water molecule (model **A**) while the asymmetry parameter η is slightly smaller for the latter. Upon tilting the water molecule (models **IC** and **IIC**) a decrease of the χ value and an increase of η were observed. Both changes are stronger in the case of binding to a metal ion (**II**). An additional H_O -bond (models **ID** and **IID**) lowers the value of χ

Table 3.1: Calculated ^{17}O quadrupole coupling parameters in model water molecule clusters and gadolinium(III) aqua complexes. Numbers in parentheses show deviation of quadrupole tensor principal axes (in degrees) in model systems from those in the gas-phase water molecule.

	Q_{xx} (a.u.)	Q_{yy} (a.u.)	Q_{zz} (a.u.)	χ (MHz)	η	$\chi\sqrt{1+\eta^2/3}$ (MHz)
A	0.2113	1.5157	-1.7270	9.96	0.76	10.86
A'	0.0908	1.2973	-1.3882	8.00	0.87	8.96
IB	0.2646 (<1)	1.4695 (<1)	-1.7342	10.00	0.69	10.77
IB'	0.1748 (<1)	1.2370 (<1)	-1.4118	8.14	0.75	8.88
IC	0.1916 (2)	1.4498 (<1)	-1.6414	9.46	0.77	10.35
IC'	0.0936 (4)	1.2156	-1.3091 (4)	7.55	0.86	8.42
ID	0.1739 (<1)	1.3985 (<1)	-1.5724	9.07	0.78	9.94
ID'	0.0522 (<1)	1.1526 (<1)	-1.2047	6.95	0.91	7.85
IIB	0.3301 (<1)	1.3535 (<1)	-1.6835	9.71	0.61	10.29
IIB'	0.2913 (<1)	1.0562 (<1)	-1.3475	7.77	0.57	8.18
IIC	0.1368 (7)	1.3311 (<1)	-1.4679 (7)	8.46	0.81	9.35
IIC'	0.0615 (12)	1.0508 (1)	-1.1123 (12)	6.41	0.89	7.21
IID	0.1229 (5)	1.3039 (<1)	-1.4269 (5)	8.23	0.83	9.12
IID'	0.0362 (8)	1.0212 (1)	-1.0574 (7)	6.10	0.93	6.92

further without affecting significantly η . For all model systems, adding two H_H -bonds resulted both in a decrease of χ and in an increase of η . Thus, one can conclude that in general all possible environmental effects upon condensation and coordination of a gas phase water molecule result in a lowering of the value of $\chi\sqrt{1+\eta^2/3}$. Among the models studied, the largest decreases of 3 MHz and 3.9 MHz were observed for systems **ID'** and **IID'**, respectively.

The dependence of ^{17}O quadrupole coupling parameters of the inner sphere water molecule on the Gd-O distance and the tilt angle θ was investigated for model **IIB** (Fig. 3.4). We found that the variation of the Gd-O distance weakly influences both χ and η : only a slight increase of χ and $\chi\sqrt{1+\eta^2/3}$ and a slight decrease of η upon the distance elongation is observed. The dependence on the angle θ is more pronounced. In particular, χ decreases by more than 1.7 MHz if θ is increased from 0° to 90° . At the same time the asymmetry parameter η increases from 0.6 to almost 1 in the same

range of θ -values. Because of the determinant role of χ in $\chi\sqrt{1+\eta^2/3}$, the overall value decreases by about 1.4 MHz.

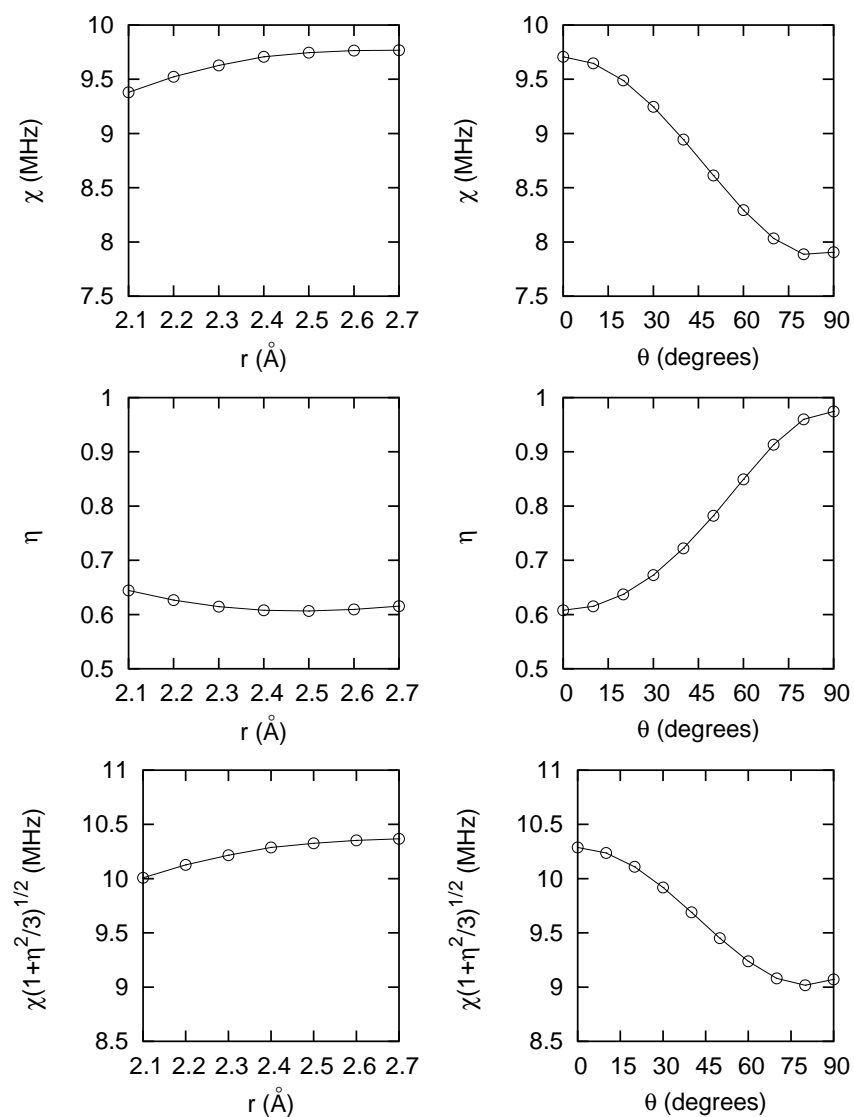


Figure 3.4: Dependence of calculated ^{17}O quadrupole coupling parameters on the Gd–O distance r (left) and the tilt angle θ (right) in the Gd^{3+} octa aqua model complex **IIB**.

3.4 Quadrupole couplings of gadolinium aqua ions in solution

3.4.1 Liquid water and gadolinium aqua complex

The next stage in approaching a realistic computational model is the conjunction of quantum chemical calculations with MD simulations. We compare the condensation effects in liquid water and coordination effects in Gd^{3+} aqua ion using classical and the density functional theory Car-Parrinello molecular dynamics (CPMD). On one hand, density functional theory tends to overstructure liquid water [135, 136]. On the other hand, CPMD is more suitable for the description of coordination compounds than classical MD based on empirical force fields. In our CPMD simulations of the Gd^{3+} aqua ion the average Gd–O distance for the first coordination sphere water molecules is 2.37 Å which is in good agreement with the average value of 2.4 Å obtained in experimental studies [69]. The coordination polyhedron of a square antiprism also agrees with experimental data on eight coordinated lanthanides [137, 138]. However, the results of classical MD simulations of the Gd^{3+} aqua ion using the force field developed for a realistic description of the coordination sphere of the gadolinium poly amino carboxylates [77, 78] show significant discrepancies with the experimental data. A mean coordination number of 10 and, consequently, a larger Gd–O distance of 3.0 Å were found in our simulations.

The calculated distributions of parameters χ , η and $\chi\sqrt{1+\eta^2/3}$ for neat liquid water are shown in Fig. 3.5a. A significant difference between the results based on the classical and on the CPMD simulations is only observed for the asymmetry parameter η . In the CPMD simulation the distribution is shifted towards higher values of η . This is consistent with the overall overstructuring of DFT water [135, 136]. The average values of χ , η and $\chi\sqrt{1+\eta^2/3}$ obtained from the CPMD simulations are equal to 8.11 ± 0.08 MHz, 0.82 ± 0.01 and 8.98 ± 0.08 MHz, respectively. The corresponding classical MD results are 8.38 ± 0.07 MHz, 0.66 ± 0.01 and 8.98 ± 0.08 MHz, respectively. Thus, even despite the difference in η values the average values of $\chi\sqrt{1+\eta^2/3}$ parameter are very similar. The values of χ and η obtained by Huber from the calculations based on classical MD simulations are 8.76 ± 0.09 MHz and 0.79 ± 0.02 for η and χ , correspondingly [72]. Using a CPMD simulation to sample configuration space Pennanen *et al.* obtained 7.77 MHz (χ) and 0.79 (η) [128], Ropp *et al.* experimentally found 8.96 MHz at 300K for the $\chi\sqrt{1+\eta^2/3}$ parameter [139].

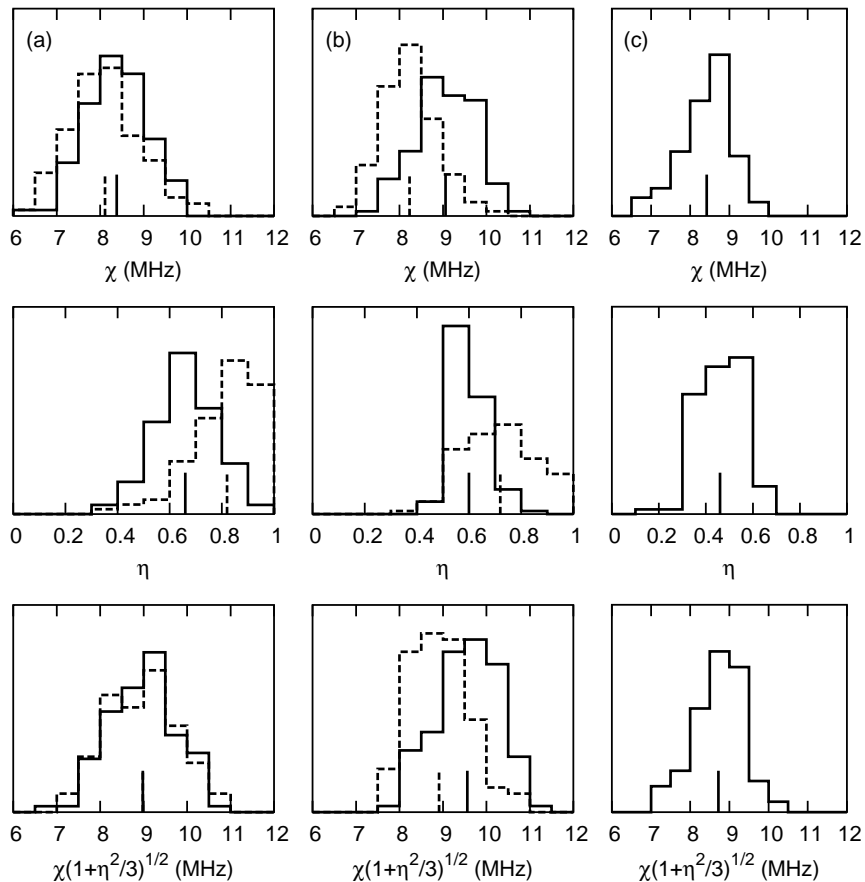


Figure 3.5: Histogram plots of the distribution of the ^{17}O quadrupole coupling parameters calculated for $(\text{H}_2\text{O})_{18}$ clusters (a), first coordination sphere water molecules of $[\text{Gd}(\text{H}_2\text{O})_8]^{3+}$ (b) and $[\text{Gd}(\text{DOTA})(\text{H}_2\text{O})]^-$ (c) sampled from classical (full line) and CPMD simulations (dashed line). Vertical lines indicate corresponding mean values.

The distributions of the calculated quadrupole coupling parameters for water in the first coordination sphere of Gd^{3+} are shown in Fig. 3.5b. As in the case of neat liquid water the asymmetry parameter η is also larger for calculations based on CPMD simulations. However, in this case also a smaller χ is observed for the CPMD result compared to the result of classical MD. This difference can be explained by an increase of the tilt angle of Gd^{3+} first sphere water molecules in density functional theory results ($\langle\theta\rangle = 23^\circ$ for the CPMD based configurations vs. $\langle\theta\rangle = 13^\circ$ from the classical MD simulations). The average values of χ , η and $\chi\sqrt{1+\eta^2/3}$ obtained from classical MD simulations are equal to 9.06 ± 0.06 MHz, 0.60 ± 0.01 and 9.59 ± 0.07 MHz, correspondingly. The CPMD simulation gives 8.23 ± 0.06 MHz, 0.72 ± 0.01 and 8.91 ± 0.06 MHz, respectively. Despite

the poor description of the coordination sphere of the Gd^{3+} ion using classical force fields, the average values of $\chi\sqrt{1+\eta^2/3}$ parameter are very similar. It is notable, that the quadrupole coupling parameters do not show large differences with those of liquid water. This disagrees with the much lower value from simultaneous fitting of ^{17}O NMR, ^1H NMRD and EPR data [18], and the more recent results of Dunand *et al.* [140]. Our calculations are, however, in reasonable agreement with a recent ENDOR study of Raitsimring *et al.* which give $\chi=6.5$ MHz and $\eta \geq 0.8$ [103].

To confirm the finding of insensitivity of ^{17}O quadrupole coupling parameters to the coordination effects of H_2O in the first sphere of metal ions, we performed an additional study of the EFG tensor in the Ca^{2+} aqua ion. The results of a CPMD simulation from Ref. [141] were used in the same way as in the case of the Gd^{3+} aqua ion. The simulated calcium ion has a lower charge (2+) and an octahedral coordination sphere (coordination number 6). We found the values for χ , η and $\chi\sqrt{1+\eta^2/3}$ of ^{17}O to be equal to 8.1 ± 0.2 MHz, 0.78 ± 0.03 and 8.9 ± 0.2 MHz, respectively. These results are very similar to those found for $[\text{Gd}(\text{H}_2\text{O})_8]^{3+}$ and liquid water, and we therefore conclude that quadrupole coupling parameters are in general not very sensitive to coordination effects on closed shell metal ions and lanthanides which can in this respect be considered as quasi-closed shell ions. This conclusion also agrees with the early theoretical and NMR relaxation studies of alkali cation crown ether complexes by Eliasson *et al.* [142].

3.4.2 GdDOTA aqua complex

To study the quadrupole coupling parameters of first sphere water molecules in gadolinium poly(amino carboxylate) complexes calculations on $[\text{Gd}(\text{DOTA})(\text{H}_2\text{O})]^-$, an approved MRI contrast agent, have been performed. Because of the considerable size of the chelating ligand DOTA (1,4,7,10-tetraazacyclododecane-1,4,7,10-tetraacetate) no CPMD simulation has been carried out. The distributions of the calculated quadrupole coupling parameters for $[\text{Gd}(\text{DOTA})(\text{H}_2\text{O})]^-$ are shown in Fig. 3.5c. The average values of χ , η and $\chi\sqrt{1+\eta^2/3}$ are equal to 8.42 ± 0.06 MHz, 0.46 ± 0.01 and 8.72 ± 0.05 MHz, correspondingly. Again, the resulting parameters are similar to those found in neat water and in the first sphere of aqua ions.

3.5 Implications for ^{17}O NMR relaxation studies

Optimization of the rotational correlation time, τ_R , is a key for the development of more efficient contrast agents for MRI and therefore its experimental determination is crucial [45]. A reliable way to get τ_R values is the simultaneous analysis of variable temperature ^1H NMRD, ^{17}O NMR and EPR data [18, 143]. In the early simultaneous analysis the same rotational correlation time has been assumed for the Gd–O vector (important for ^{17}O relaxation) and for the Gd–H vector (important for ^1H relaxation). The apparent discrepancies in fitting longitudinal ^{17}O relaxation rates and ^1H NMRD curves together were resolved by either fitting the apparent Gd–H distance or the quadrupole coupling constant [18]. This led in the latter case to an increase of the quadrupole coupling parameter $\chi\sqrt{1+\eta^2/3}$ up to a factor of 2. In a later study Dunand *et al.* allowed for an internal motion of the water molecule in the complex, leading to different rotational correlation times τ_{RH} and τ_{RO} [140]. From sterical considerations a τ_{RH}/τ_{RO} ratio between $0.65 \leq \tau_{RH}/\tau_{RO} \leq 1$ has been determined. From direct observation of the ^{17}O relaxation of bound water in the slowly exchanging $[\text{Ln}(\text{DOTAM})(\text{H}_2\text{O})]^{3+}$ -complexes (Ln=Eu, Tb) in acetonitrile solution at low temperature a quadrupole coupling parameter of 5.2 ± 0.5 MHz has been deduced. Struis *et al.* determined experimentally values of 6.6 MHz or 5.7 MHz for water bound to Mg^{2+} , depending if viscosity changes for very highly concentrated solutions are considered or not [144].

Table 3.2: Summary of the calculated mean values of ^{17}O quadrupole coupling parameters for water molecules in different chemical environments simulated using classical molecular dynamics (TIP3P) and CPMD simulations.

		χ (MHz)	η	$\chi\sqrt{1+\eta^2/3}$ (MHz)
liquid H_2O	TIP3P	8.38	0.66	8.98
	CPMD	8.11	0.82	8.98
$\text{Gd}(\text{H}_2\text{O})_n^{3+}$	TIP3P	9.06	0.60	9.59
	CPMD	8.23	0.72	8.91
$\text{Ca}(\text{H}_2\text{O})_6^{2+}$	CPMD	8.1	0.78	8.9
$[\text{Gd}(\text{DOTA})(\text{H}_2\text{O})]^-$	TIP3P	8.42	0.46	8.72

Our quantum-chemical calculations led to the conclusion that the quadrupole cou-

pling parameter $\chi\sqrt{1 + \eta^2/3}$ depends only slightly on binding of the water molecule to lanthanide ions. The value of 8.7 MHz calculated for $[\text{Gd}(\text{DOTA})(\text{H}_2\text{O})]^-$ is equal to the value determined in neat water (9.0 MHz) within the precision of the calculations. Even if the quadrupole coupling parameter $\chi\sqrt{1 + \eta^2/3}$ enters as squared value in the calculation of the relaxation rates we have to keep in mind that quadrupole relaxation constitutes only between 25 % and 33 % to the overall ^{17}O relaxation of water molecules bound to Gd^{3+} in poly amino carboxylate complexes. The mayor contribution is dipolar relaxation due to interaction with the electron spin of the paramagnetic center.

In conclusion, the ^{17}O quadrupole coupling parameters of a coordinated water molecule are in general very similar to that of a water molecule in the bulk environment (Table 3.2). The fixed value of 9.0 MHz for the quadrupole parameter $\chi\sqrt{1 + \eta^2/3}$ can therefore be safely used in experimental estimations of the rotation correlation time of closed shell ion and lanthanide ion aqua complexes.

Chapter 4

Pseudopotential calculations of hyperfine interactions

4.1 Introduction

The mathematical expressions underlying hyperfine coupling constants are simple. However, the local nature of this property makes its computation difficult for electronic structure theory methods based on the optimization of global properties such as the total energy. While all-electron approaches based on localized basis sets (e.g. Gaussian or Slater type atomic orbitals) have already proven to give satisfactory results for the calculation of isotropic hyperfine coupling constants, there is still a lack of methods for calculations of this property in pseudopotential based approaches. These are of particular importance for condensed matter physics [145] and plane wave based first-principles dynamics applications in chemistry and biology [146].

The difficulty in evaluating hyperfine coupling constants within pseudopotential-based calculations is due to two main reasons. The first one concerns the behavior of the pseudo wavefunctions in the vicinity of the nucleus (within the predefined core radius) which differ from the all-electron ones while playing a decisive role in the determination of both isotropic and dipolar (though to a lesser extent) hyperfine coupling constants. The solution to this problem was proposed by Van de Walle and Blöchl [147] who employed a so-called reconstruction of the all-electron wavefunction in order to calculate hyperfine couplings from the pseudo wavefunctions. It is worth noting that in DFT calculations this correction does not solve the problem of the behavior of the exchange-correlation potential in the vicinity of the nucleus, necessary for a correct description of spin-polarization

effects on the valence orbitals. Furthermore, no extended benchmarks of this method were provided until now. Secondly, the complete elimination of the core electrons in pseudopotential calculations implies complete disregard of the spin-polarization of core electrons. While this effect has only negligible influence on the valence wavefunctions of the system, its contribution to the isotropic hyperfine coupling constants can be significant. This is explained by the high magnitudes of the atomic core s -type wavefunctions at the point of the nucleus which in turn can result in high values of the spin-density.

In this Chapter, we will consider the spin-density $\rho^s(\mathbf{r}) = \rho^\uparrow(\mathbf{r}) - \rho^\downarrow(\mathbf{r})$ as the sum of valence and core contributions, $\rho_v^s(\mathbf{r})$ and $\rho_c^s(\mathbf{r})$. We will first review available approaches for calculating the valence contribution to the hyperfine coupling constants. A novel methodology for calculating the dipolar hyperfine coupling tensor in supercell calculations will be presented. Afterwards, we will present a practical method for calculating the core spin-polarization contribution to the Fermi contact hyperfine coupling constants. The accuracy of our approach is supported by the benchmark calculations on the small molecular radicals of first row elements, which show that the core electrons can not be disregarded in the case when the unpaired electron populates other than s -type atomic orbitals centered on the considered atom. Finally, we will make an attempt to assess the importance of core spin-polarization effects across the periodic table.

4.2 Valence contribution to hyperfine coupling constants

4.2.1 Isotropic hyperfine coupling constants

In pseudopotential electronic structure calculations, the behavior of valence one-electron wavefunctions deviates from their all-electron counterparts. This is so because of the absence of the orthogonality conditions with core electrons removed from the problem and because of special requirements of computational methods. In plane wave basis set implementation this special requirement is the extreme smoothness of pseudopotential wavefunctions for the purpose of minimization of the number of basis functions. However, these deviations are restricted in space and occur only within the atomic-centered spheres of small radius. This radius is often equal to the pseudopotential cutoff radius r_c which is of the order of 1 a. u. for the first row elements. Figure 4.1 illustrates typical

pseudopotential and all-electron wavefunctions on the example of the oxygen atom. The difference is evident, the $2s$ pseudopotential wavefunction is smooth, nodeless and has no cusp. The absolute magnitude of the $2s$ pseudopotential wavefunction at the origin is much smaller than the magnitude of its all-electron counterpart.

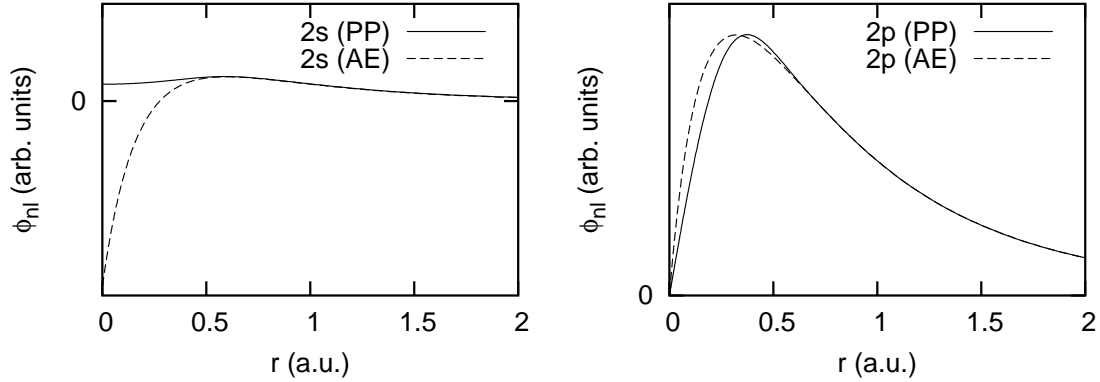


Figure 4.1: Comparison of $2s$ (a) and $2p$ (b) all-electron (AE) and pseudopotential (PP) atomic wavefunctions for oxygen atom.

Since the shape difference is localized within the small atom-centered spheres, not in the “bonding regions”, chemical and most of physical properties are correctly described by the pseudopotential electronic structure theories. This does not apply to the hyperfine coupling constants discussed here. A reconstruction of the all-electron (AE) wavefunctions $\psi_i(\mathbf{r})$ from the pseudopotential ones, $\tilde{\psi}_i(\mathbf{r})$, has to be performed in this case. This procedure in its most general form can be described by the following expression [148]

$$\psi_i(\mathbf{r}) = \tilde{\psi}_i(\mathbf{r}) + \sum_j [\phi_j(\mathbf{r}) - \tilde{\phi}_j(\mathbf{r})] \langle \tilde{p}_j | \tilde{\psi}_i \rangle_{r_c}, \quad (4.1)$$

where $\phi_i(\mathbf{r})$ and $\tilde{\phi}_i(\mathbf{r})$ are the AE and PP atomic wavefunctions, respectively. Index j is the composition of the atomic site position \mathbf{r}_j and the angular momentum quantum numbers of the valence atomic level $\{l_j m_j\}$. The notation $\langle \cdot | \cdot \rangle_{r_c}$ stands for the scalar product evaluated within the core radius r_c . The functions p_j are the projector functions which have to satisfy the following condition:

$$\langle \tilde{p}_j | \tilde{\phi}_i \rangle_{r_c} = \delta_{ij}. \quad (4.2)$$

For the purpose of the present discussion it is convenient to reformulate the Fermi contact

hyperfine coupling formula (eq. 2.3) introduced in Chapter 2 as

$$A_{iso}(I) = \frac{4\pi}{3} \frac{\mu_e \mu_N g_e g_I}{\langle S_z \rangle} \int \rho^s(\mathbf{r}) \delta(\mathbf{r}) d\mathbf{r}, \quad (4.3)$$

where μ_e and μ_I are Bohr and nuclear magnetons, g_e and g_I are g -values of free electron and nucleus I , $\langle S_z \rangle$ is the expectation value of the total electronic spin z -component. The vector \mathbf{r} is taken relative to the position of nucleus I .

By constructing the projector p_i from the Dirac's delta function $\delta(\mathbf{r})$ and performing the reconstruction of only the s component of the AE wavefunction, Van de Walle and Blöchl arrived to the simple expression for the valence spin density at the point of nucleus [147]

$$\rho_v^s(0) = \tilde{\rho}_v^s(0) + \frac{\tilde{\rho}_v^s(0)}{|\tilde{\phi}_s(0)|^2} \left(|\tilde{\phi}_s(0)|^2 - |\phi_s(0)|^2 \right), \quad (4.4)$$

which can be directly applied to the calculations of Fermi contact HFCCs.

4.2.2 Dipolar hyperfine coupling constants

Unlike the strictly localized Fermi contact operator, the dipole-dipole interaction operator obeys a r^{-3} decay law. Evaluation of the matrix elements of the hyperfine anisotropy tensor involves the integration in real space:

$$T_{ij}(I) = \frac{1}{2} \frac{\mu_e \mu_N g_e g_I}{\langle S_z \rangle} \int \rho^s(\mathbf{r}) \frac{3r_i r_j - \delta_{ij} r^2}{r^5} d\mathbf{r}. \quad (4.5)$$

For infinite periodic systems its straightforward evaluation by the numerical integration in real space is unrealistic. In computational approaches based on plane wave basis sets the pseudopotential spin density is naturally available in the G -space linked to the real space density by the Fourier transform [149]

$$\tilde{\rho}^s(\mathbf{r}) = \frac{1}{\Omega} \sum_{|\mathbf{G}| < G_c} \tilde{\rho}^s(\mathbf{G}) e^{i\mathbf{G}\cdot\mathbf{r}}, \quad (4.6)$$

where the summation is taken over all plane wave basis functions defined by the G -space vectors \mathbf{G} enclosed within the sphere of radius G_c . Ω is the real space supercell volume. Complete expression for the elements of the hyperfine anisotropy tensor is then [147, 150]

$$T_{ij}(I) = \frac{1}{2} \frac{\mu_e \mu_N g_e g_I}{\langle S_z \rangle} \times \left[- \sum_{|\mathbf{G}| < G_c} 4\pi \frac{3G_i G_j - \delta_{ij} G^2}{G^2} \tilde{\rho}^s(\mathbf{G}) e^{i\mathbf{G}\cdot\mathbf{r}_I} + \int_{r < R_C} (\rho^s(\mathbf{r}) - \tilde{\rho}^s(\mathbf{r})) \frac{3r_i r_j - \delta_{ij} r^2}{r^5} d\mathbf{r} \right] + \Delta T_{ij}. \quad (4.7)$$

The first term accounts for the dipolar couplings evaluated from the pseudopotential spin density in G -space. The second term represents the correction due to the difference $\rho^s(\mathbf{r}) - \tilde{\rho}^s(\mathbf{r})$ in the core region of atom I which can be evaluated numerically in real space. The last term, ΔT_{ij} , which accounts for the contributions due to the difference $\rho^s(\mathbf{r}) - \tilde{\rho}^s(\mathbf{r})$ from the neighboring atomic regions, is negligible in most cases [147].

Although the formulation (4.7) is suitable for most practical calculations, it is not convenient for our specific purpose. Dipolar HFI parameters evaluated in G -space take into account interaction with an infinite array of periodic images. We aim modeling of solutions in the ideal case of an infinite dilution of paramagnetic ion. In this case, the contribution of the spin density localized on the paramagnetic ion closest to the nucleus under considerations as well as associated ligand-centered contributions has to be considered. This can be efficiently achieved by the integration in real space over the volume of supercell with the paramagnetic ion translated to its center. In the plane wave codes such an integration is convenient to perform on the uniform real space grid. However, due to the behavior of the dipolar operator close to the origin (nucleus under consideration) such integration can not be performed accurately on uniform grids. We solve this problem by introducing a ‘‘pseudo-dipolar’’ operator $f(r)\frac{3r_i r_j - \delta_{ij} r^2}{r^2}$. Unlike $1/r^3$, the function $f(r)$ is smooth and has no singularity at the origin. The complete expression for the hyperfine anisotropy tensor elements takes the form

$$T_{ij}(I) = \frac{1}{2} \frac{\mu_e \mu_N g_e g_I}{\langle S_z \rangle} \times \left[\int_{\Omega} \tilde{\rho}^s(\mathbf{r}) f(\mathbf{r}) \frac{3r_i r_j - \delta_{ij} r^2}{r^2} d\mathbf{r} + \int_{r < R_C} \left(\frac{1}{r^3} \rho^s(\mathbf{r}) - f(r) \tilde{\rho}^s(\mathbf{r}) \right) \frac{3r_i r_j - \delta_{ij} r^2}{r^2} d\mathbf{r} \right]. \quad (4.8)$$

On the reconstruction stage (the second term) we reconstruct the product $f(r)\tilde{\rho}^s(\mathbf{r})$ rather than just the pseudopotential density $\tilde{\rho}^s(\mathbf{r})$. Following the principles of construction of norm-conserving pseudopotential wavefunctions [151] we obtain $f(r)$ by sewing together $1/r^3$ and a smooth function at $r < r_c$ (Fig. 4.2)

$$f(r) = \begin{cases} \frac{1}{r^3}, & r \geq r_c, \\ \sum_{i=0}^2 c_i j_i(r), & r < r_c, \end{cases} \quad (4.9)$$

where $j_i(r)$ are spherical Bessel functions of the first kind [152] and the coefficients c_i are determined by the conditions of continuity of $f(r)$ and its first two derivatives at r_c :

$$\frac{d^n f(r_c)}{dr^n} = \frac{d^n (1/r_c^3)}{dr^n}, \quad n = 0, 1, 2. \quad (4.10)$$

The value r_c is chosen to be equal to the pseudopotential cutoff radius.

It is worth mentioning that the quadrupolar coupling tensor can be calculated in a similar way once the spin-density $\rho^s(\mathbf{r})$ is substituted by the total charge density and the physical constants are properly changed in eq. (4.8).

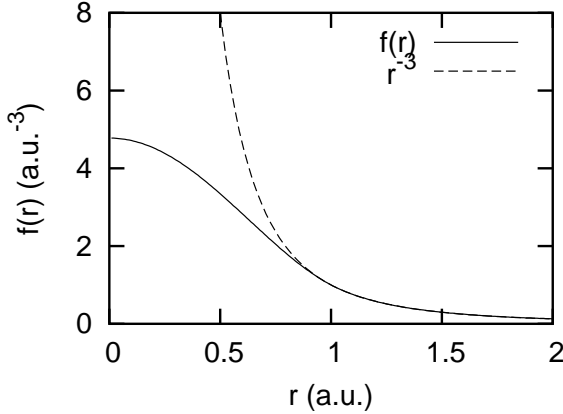


Figure 4.2: Behavior of the radial-dependent parts of the dipolar operator, $1/r^3$, and the pseudo-dipolar operator, $f(r)$ ($r_c=1$ a.u.).

4.3 Core spin-polarization correction

4.3.1 Methodology

We propose a simple approach for the estimation of the core spin-polarization contribution to the total spin-density. The approach is based on the solution of the unrestricted Kohn-Sham equations for core states only in the external potential of frozen valence spin-up and spin-down electron densities (termed frozen valence spin-density below). These densities are constructed to reproduce those of the system under consideration in the core region of nucleus I . Practically, this can be achieved using both basis set based approaches or numerical calculations on a spherically symmetric atom. While the first approach substantially depends on the choice of a basis set, making it less flexible, the second one implies that the error introduced by the spherical averaging of the external potential can be neglected.

Our implementation is based on the second method. The accuracy of a frozen valence spin-density approach for the calculation of $\rho_c^s(\mathbf{r}_I)$ can be validated for the case of atoms ($\mathbf{r}_I=0$ for simplicity) using the following simple computational scheme. Here we limit our study to the first-row atoms C, N, O and F using electronic configurations where only the p -shell is spin-polarized. For the first-row atoms the core electrons belong only

Table 4.1: $\rho_c^s(0)$ (in a. u.) from all-electron (AE) and frozen valence spin-density (FV) PBE [153] DFT numerical atomic calculations.

Atom	Configuration	$\rho_c^s(0)$, AE	$\rho_c^s(0)$, FV
C	$2s\{1\uparrow,1\downarrow\}2p\{2\uparrow,0\downarrow\}$	-0.199294	-0.199265
N	$2s\{1\uparrow,1\downarrow\}2p\{3\uparrow,0\downarrow\}$	-0.441030	-0.440956
O	$2s\{1\uparrow,1\downarrow\}2p\{3\uparrow,1\downarrow\}$	-0.417946	-0.417854
F	$2s\{1\uparrow,1\downarrow\}2p\{3\uparrow,2\downarrow\}$	-0.273401	-0.273335

to the $1s$ -shell thus the core contribution to the spin-density at the point of the atomic nucleus can be written as $\rho_c^s(0) = \phi_{1s}^{\uparrow 2}(0) - \phi_{1s}^{\downarrow 2}(0)$. The densities $\rho_v^{\uparrow}(\mathbf{r})$ and $\rho_v^{\downarrow}(\mathbf{r})$ are obtained from frozen core calculations, with the atomic core wavefunctions $\phi_{1s}^{\uparrow}(\mathbf{r}) = \phi_{1s}^{\downarrow}(\mathbf{r})$ are taken from all-electron calculations in the corresponding spin-averaged configuration $2s\{1\uparrow,1\downarrow\}2p\{\frac{n}{2}\uparrow,\frac{n}{2}\downarrow\}$. The results of our frozen valence spin-density calculations based on the above mentioned densities $\rho_v^{\uparrow}(\mathbf{r})$ and $\rho_v^{\downarrow}(\mathbf{r})$ are then compared to all-electron results for $\rho_c^s(0)$ (See Table 4.1). For light atoms we observed that the difference between these two approaches never exceeds 0.1%. Thus, the core spin-polarization has almost no influence on the valence wavefunctions of these atoms. It should also be mentioned that in the case of first-row atoms the with spin-polarized p -shell, $\rho_v^s(0)$ is positive and of comparable magnitude to the core contribution. Therefore, the neglect of core spin-polarization will result in large errors in the Fermi contact hyperfine coupling constants.

Figure 4.3 illustrates the spin-polarization for an oxygen atom in its triplet spin state ($2s\{1\uparrow,1\downarrow\}2p\{3\uparrow,1\downarrow\}$ configuration). In this case the spin density at $r=0$ is the result of the spin-polarization of the $1s$ and $2s$ states due to the different exchange-correlation potentials (Fig. 4.3b) for spin-up and spin-down electrons. We observe that $\rho_c^s(0)$ ($= \rho_{1s}^s(0)$) and $\rho_v^s(0)$ ($= \rho_{2s}^s(0)$) are comparable in their magnitudes while their signs differ: the core spin-density has a negative value in contrast to the valence one (Fig. 4.3c). Both contributions have sharp extrema at the point of nucleus, but integrate to zero. Similar behavior was observed for the series of benchmark molecules chosen as validation examples.

The electronic structure calculations of more complicated molecular and condensed matter systems using pseudopotentials require some additional care. In this case a reconstruction of the all-electron wavefunctions [130, 147, 148] $\psi_i^{\uparrow(\downarrow)}(\mathbf{r})$ from the pseudo wavefunctions $\tilde{\psi}_i^{\uparrow(\downarrow)}(\mathbf{r})$ has to be performed since the shapes of $\tilde{\psi}_i^{\uparrow(\downarrow)}(\mathbf{r})$ differ from those

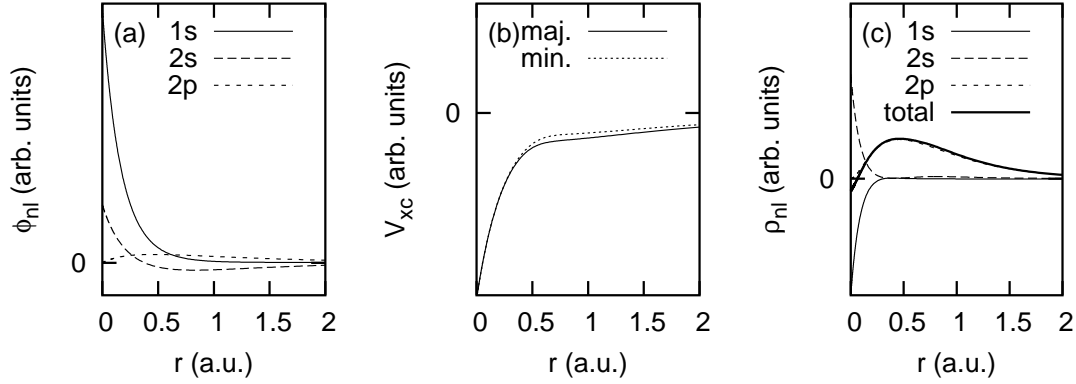


Figure 4.3: (a): Radial parts $\phi_{nl}(r)$ of atomic one-electron wavefunctions of the oxygen atom. (b): Self-consistent exchange-correlation potentials $v_{xc}(r)$ for the majority and minority spin components for the oxygen atom. (c): Contributions of the electronic sub-shells to $\rho^s(r)$ in the spin-polarized ($2s\{1\uparrow,1\downarrow\}2p\{3\uparrow,1\downarrow\}$ configuration) oxygen atom. The thick line shows the total spin density $\rho^s(r)$.

of $\psi_i^{\uparrow(\downarrow)}(\mathbf{r})$ within the core radius r_c around the nucleus. Here, we propose a simple procedure which takes into account the specificity of our problem. In our approach we construct an atom in which spin-up and spin-down valence electron densities $\rho_v^{\uparrow(\downarrow)}(r)$ mimic those of the system under consideration in the neighborhood of the nucleus I . We expand these densities in terms of the spin-up and spin-down partial atomic occupation numbers $\omega_l^{\uparrow(\downarrow)}$ and the valence orbitals $\phi_l(r)$ of the spherically symmetric all-electron atom (all orbitals correspond to the spin-averaged all-electron wavefunctions used to generate the pseudopotentials)

$$\rho_v^{\uparrow(\downarrow)}(\mathbf{r}) = \sum_l \omega_l^{\uparrow(\downarrow)} \phi_l^2(\mathbf{r}). \quad (4.11)$$

The occupation numbers can be calculated using the following general expression

$$\omega_l^{\uparrow(\downarrow)} = \sum_i^{N_{\uparrow(\downarrow)}} \sum_{m=-l}^l \langle \tilde{\psi}_i^{\uparrow(\downarrow)} | \tilde{\phi}_{lm} \rangle_{r_c} \langle \tilde{\phi}_{lm} | \tilde{\psi}_i^{\uparrow(\downarrow)} \rangle_{r_c}, \quad (4.12)$$

assuming that the pseudo atomic orbitals form a complete basis set within a small radius r_c around the nucleus. The pseudoatom valence orbitals $\tilde{\phi}_{lm}(\mathbf{r}) = \tilde{R}_l(r)Y_{lm}(\mathbf{r})$ are represented as the product of the radial part $\tilde{R}_l(r)$ and the spherical harmonic $Y_{lm}(\mathbf{r})$. N^\uparrow and N^\downarrow are the numbers of spin-up and spin-down electrons in the system, correspondingly. For periodic systems the proper sampling of the first Brillouin zone must also be included

into these expressions to account for the dependence of the pseudo wavefunctions of the system on the crystal momentum.

Our implementation is based on the following expression for the atomic occupation numbers

$$\omega_l^{\uparrow(\downarrow)} = \sum_i^{N_{\uparrow(\downarrow)}} \sum_{m=-l}^l \frac{\langle f Y_{lm} | \tilde{\psi}_i^{\uparrow(\downarrow)} \rangle^2}{\langle f | \tilde{R}_l \rangle^2}, \quad (4.13)$$

where the cutoff function $f(r)$ is used in order to limit the overlap integral only to the atom-centered sphere around the nucleus under consideration. For reasons of computation efficiency in our implementation expression (4.13) is evaluated in G -space. We take a cutoff function $f(G)=1$ which in the real space representation approaches a Dirac delta function $\delta(r=0)$ when the plane wave cutoff tends to infinity, $G_c \rightarrow \infty$. Another motivation for this choice is that in this case $\omega_0^{\uparrow(\downarrow)} = \tilde{\rho}_v^{\uparrow(\downarrow)}(0)/\tilde{R}_0^2(0)$ and therefore one obtains $\rho_v^s(0) = (\omega_0^{\uparrow} - \omega_0^{\downarrow})\phi_0^2(0) = \tilde{\rho}_v^s(0)R_0^2(0)/\tilde{R}_0^2(0)$, which is identical to “scaling up the spin-density” eq. (4.4). From this point of view our approach is the extension of simple wavefunction reconstruction scheme from Ref. [147] to the angular momenta $l > 0$.

4.3.2 Benchmarks

To provide the necessary benchmarks we compare the quality of our results based on pseudopotentials and plane wave basis sets with all-electron calculations performed using Slater-type orbitals. STO basis sets correctly describe the cusp condition and thus usually provide the most accurate theoretical predictions of hyperfine coupling constants. The benchmark set consists of a representative series of small molecular doublet radicals containing only hydrogen and first-row atoms C, N, O, F. The core spin-polarization effects are important for these atoms and originate uniquely from the $1s$ core shell. For these molecules reliable experimental data are also available together with computational results obtained from both all-electron DFT and high level ab initio methods. For the sake of completeness, we also compare our results for pseudopotential plane wave calculations with frozen core all-electron calculations in order to estimate the importance of core spin-polarization effects. The results are summarized in convenient form in Figure 4.4.

The basic goal of this work is not an accurate reproduction of experimental data but rather a comparison of two different computational methodologies in the context of what is known experimentally. For this reason, vibrational averaging or environment effects, important for the precise prediction of hyperfine coupling constants, were not taken into

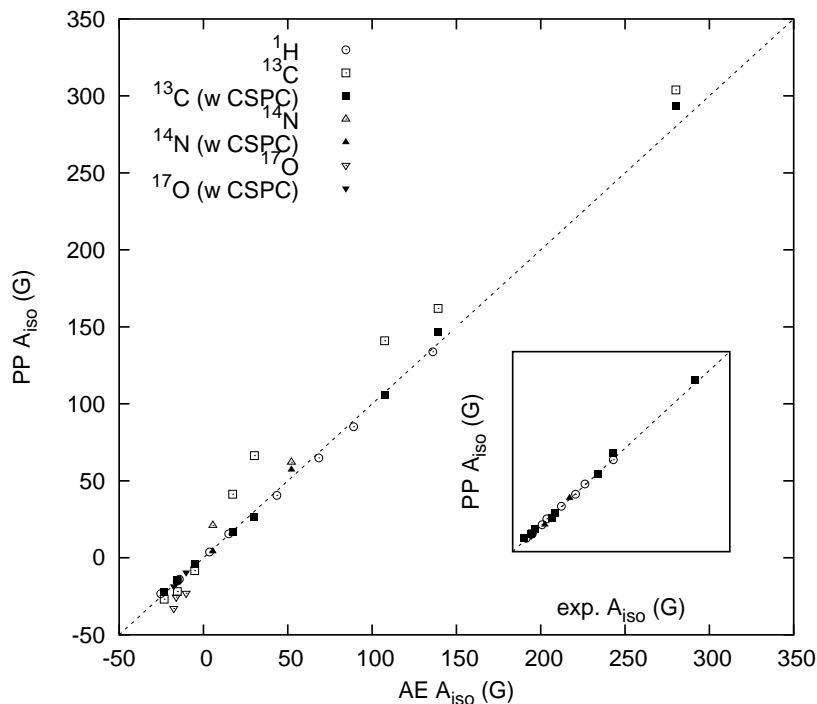


Figure 4.4: Comparison of Fermi contact hyperfine coupling constants (in Gauss units) calculated using the all-electron (AE) and the pseudopotential (PP) approaches in seven molecular radicals (CH_3 , C_2H_3 , C_3H_5 , H_2CN , HCO , FCO , NO_2). The filled symbols correspond to the values corrected for the core spin-polarization contribution. The ^{19}F HFCC in FCO is out of the scale. The inset compares the values calculated using the pseudopotential scheme with the core spin-polarization correction and the accurate experimental data. For the inset the same scale of values applies [154–163].

account. In both approaches we use the Becke gradient-corrected exchange density functional [98] together with the gradient-corrected correlation density functional proposed by Perdew [164]. The unrestricted solution of the Kohn-Sham equations was used in order to account for spin-polarization effects in the valence wavefunctions. In the plane wave calculations we used original norm-conserving Troullier-Martins pseudopotentials [151] generated from spin-averaged wavefunctions computed for atoms in their ground states. For the construction of the hydrogen atom pseudopotential we used an occupation number of 0.7 instead of the nominal value 1.0. The cutoff radii used in the generation of all other pseudopotentials are the same as the ones given in Ref. [165]. These values correspond to rather hard pseudopotentials. Nonlinear core corrections [166] (NLCC) were applied for the first-row elements. The NLCC core radii were chosen experimentally to

achieve a compromise between a reasonable NLCC “softness” and accuracy of results. For clarity all these values are summarized in Table 4.2.

Table 4.2: Cutoff radii r_c used for the pseudopotential generation and NLCC core radii r_{core} (in a. u.). The same values of r_c were used for both s - and p -channels of the first-row elements.

	H	C	N	O	F
r_c	0.5	1.14	0.96	0.83	0.73
r_{core}	-	1.03	0.77	0.65	0.58

The Gauss-Hermite integration with 16 points was used for the calculation of the nonlocal parts of the pseudopotential. The calculations were performed in a $12 \text{ \AA} \times 12 \text{ \AA} \times 12 \text{ \AA}$ isolated cubic box using Tuckerman-Martyna’s Poisson equation solver [167]. The size of the box was chosen large enough to make the results consistent with STO calculations on isolated molecules. The plane wave cutoff of 100 Ry for the wavefunction expansion was chosen to ensure the basis set completeness, while for the electron density expansion a consistent cutoff of 400 Ry was used. The first Brillouin zone was sampled only at the Γ point. These calculations were performed with a modified version of the CPMD code [132]. STO calculations were performed with the basis set of TZ2P quality using the ADF2003 code [89]. All geometries were optimized at the same level of theory using STO basis sets. We use frozen valence spin-density calculations implemented in a numerical atomic DFT code from the ESPRESSO program package [168], which allows for predefined frozen wavefunctions and partial atomic occupation numbers. The all-electron wavefunctions were reconstructed taking into account only the s -channel for H, while for the first-row atoms also the p -channel was reconstructed. This is a necessary condition for an accurate evaluation of the correction since spin population of valence p -type orbitals often produce a strong spin-polarization of s -core orbitals (See Chapter 19 in Ref. [62]).

The results in Figure 4.4 prove the accuracy of the proposed correction scheme. For the simplest case of ^1H hyperfine coupling constants, no spin-polarization effects occur and the pseudo wavefunctions in the vicinity of these nuclei resemble the all-electron wavefunctions apart from the absence of the nuclear cusps. Thus, the wavefunction reconstruction approach proposed by Van de Walle and Blöchl gives results very close to the all-electron STO calculations and to experimental data as well. Comparison between the all-electron calculations and the frozen core STO calculations also shows small dif-

ferences in the ^1H hyperfine coupling constants. This confirms the hypothesis about the negligible influence of the spin-polarization of core orbitals on the valence ones. For heavier elements in the first row of the periodic table the core spin-polarization contribution is present. From Fig. 4.4 one can see that $\rho_c^s(\mathbf{r}_I)$ is usually lower in magnitude and has an opposite sign compared to $\rho_v^s(\mathbf{r}_I)$. The HFCCs calculated without the core spin-polarization correction tend to be overestimated (open squares in Fig. 4.4). In some cases $\rho_c^s(\mathbf{r}_I)$ is negligible while in others (e. g. ^{14}N HFCC in H_2CN) it cannot be neglected. This observation is in perfect agreement with the STO calculations.

In conclusion, the proposed core spin-polarization correction recovers the largest part of the error in pseudopotential plane wave calculations of the Fermi contact HFCCs when compared to all-electron calculations and experimental results. It turned out that for the first-row elements the core contribution to the isotropic HFCCs is significant. In the last part of this Chapter, we will try to assess its importance for the rest of the periodic table. Since core electrons of the first-row elements have s symmetry, they do not contribute to the dipolar hyperfine couplings. Investigation of the core-level contribution to the dipolar HFCCs for heavier elements is left for future investigations.

4.3.3 Trends across the periodic table

Probing HFIs with magnetic resonance experiments, both ESR and NMR, can be performed for the nuclei of the elements constituting a larger part of the periodic table. There is also no restriction on performing the calculations of HFCCs for any element in the periodic table. Moreover, pseudopotential calculation are more common for the systems involving heavy elements since they allow decreased computational demand by disregarding core electrons from the problem and by avoiding an explicit treatment of relativistic effects. However, a general picture of core contributions to the isotropic HFCCs across the periodic table is still missing. It is difficult and demanding to deduce this general picture from the studies on various molecular and solid state systems. So, we turn to the methodology based on the atomic density functional theory calculations and perform a systematic study of the core contributions to the Fermi contact HFCCs for all elements starting with Li ($Z=3$) till Rn ($Z=86$). We do not intend to provide a quantitative theory of HFIs transferable to all possible complex molecular or solid state environments. Instead, we would like to provide a semi-qualitative picture to reveal the relative importance of core electrons in different parts of the periodic table.

Our computational methodology is based on the same all-electron numerical atomic code as used before. This code is able to perform relativistic calculations in the scalar approximation. The PBE exchange-correlation density functional [153] has been used. The quantity of interest is the the response of core electrons to the spin-polarization of valence sub-shells,

$$R_l^c = \frac{\partial \rho_c^s(0)}{\partial \omega_{v,l}^s}, \quad (4.14)$$

where $\omega_{v,l}^s = \omega_{v,l}^\uparrow - \omega_{v,l}^\downarrow$ is the spin-differential population of valence electrons with angular momentum l . The response is calculated within the finite difference approximation. The electronic configurations of atoms are the spin-averaged ground state configurations of neutral atoms. The valence sub-shells are the sub-shells filled in the corresponding period. For the elements with zero population in one of the valence sub-shells (which is typical for the beginning of periods) we modify the ground state electronic configuration by promoting 0.1 electron to the empty valence sub-shells from the populated ones. For example, the ground state of calcium is $[\text{Ar}]4s^2$ - we use $[\text{Ar}]4s^{1.8}4p^{0.1}3d^{0.1}$ in our calculations. We found that the R_l^c values and the $|\phi_{v,0}(0)|^2$ values are relatively insensitive to such rehybridization effects and to the charge of the atom. The rest of electrons are considered as core electrons.

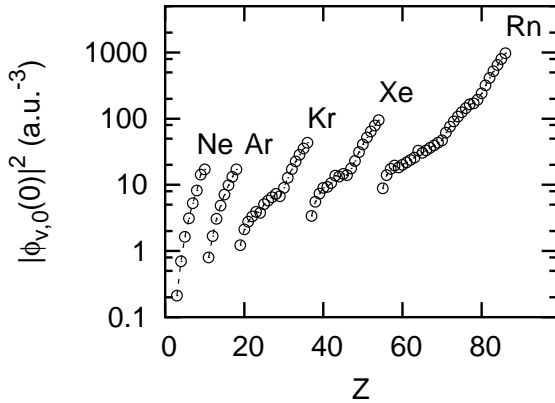


Figure 4.5: Values of $|\phi_{v,0}(0)|^2$ as a function of the atomic number Z . The labels indicate the noble gases terminating periods.

First, it is important to discuss how the valence contribution $|\phi_{v,0}(0)|^2$ varies across the periodic table. The semi-logarithmic plot (Fig. 4.5) shows the values of $|\phi_{v,0}(0)|^2$ as a function of atomic number Z . The values span 5 orders of magnitude and exhibit a monotonic (except non-regular ground state configurations) increase of $|\phi_{v,0}(0)|^2$ within the periods. The slopes of the $|\phi_{v,0}(0)|^2$ versus Z curves are higher for the elements filling the shells with lower angular momentum.

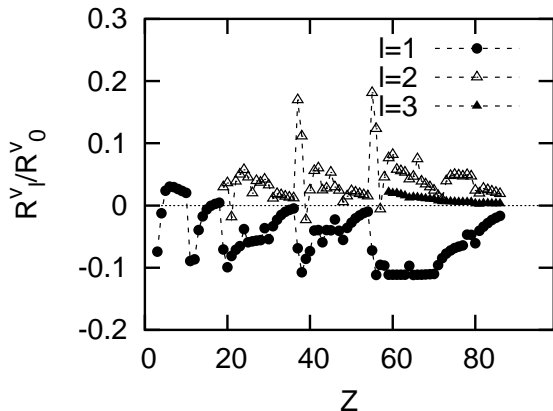


Figure 4.6: Response of $l=0$ valence electrons to the spin-polarization of the valence states with $l>0$ presented as the ratio R_l^v/R_0^v .

One would naturally ask about the response of valence s -electrons to the spin-polarization of the valence states with $l>0$. Unfortunately, in this case the picture provided by the atomic calculations has very limited transferability to complex systems. Nevertheless, the trends are worth discussion at least on the qualitative level. Figure 4.6 shows the dependence of the $R_l^v = \partial\rho_v^s(0)/\partial\omega_{v,l}^s$ on the atomic number Z for $l>0$. The dependence is presented in the convenient form of ratio $R_l^v/R_0^v = R_l^v/|\phi_{v,0}(0)|^2$. At a glance, the values of R_l^v are in general about one order of magnitude smaller than the values of R_0^v . The absolute magnitudes of R_l^v/R_0^v tend to decrease with increasing l . For $l=1$ the ratio R_l^v/R_0^v is negative and $R_l^v/R_0^v > -0.1$ except the late elements in the first and second rows where it is positive. For $l=2$ this ratio is in general positive and $R_l^v/R_0^v < 0.1$ except the first two elements in the fifth and sixth periods where it reaches $R_l^v/R_0^v \approx 0.2$. For $l=3$ the ratio is always positive and remarkably small, $R_l^v/R_0^v < 0.03$.

Finally, we discuss the relative core spin-polarization ratios R_l^c/R_0^v obtained from the numerical DFT calculations on atoms (Fig. 4.7). The response of the core electrons to the spin-polarization of the valence s -subshells tends to be positive and achieves respectable magnitudes for the first row elements. For the alkali elements of consequent periods it is also rather large and negative. Spin-polarization of the valence p -subshell results in large negative values of $\rho_c^s(0)$. It tends to be much smaller in all the consequent periods. This explains the relative importance of core spin-polarization effects on Fermi contact HFCCs for the first row (Li to Ne) elements. For the third period elements (Na to Ar) the core spin-polarization contribution is much less pronounced. This can be explained by the fact that in the third period the spin-polarization contributions of $1s$ and $2s$ electrons have opposite signs and partially cancel each other. Spin-polarization of d electrons lead to negative values of $\rho_c^s(0)$ which are large for all periods starting from the fourth where

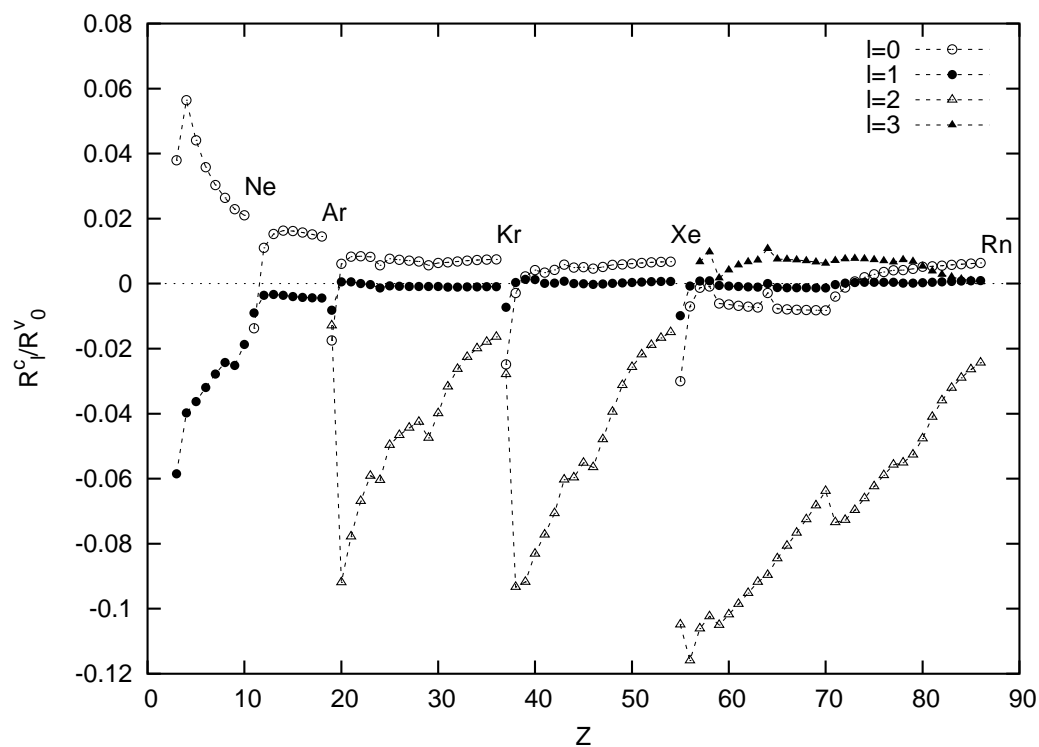


Figure 4.7: Relative core spin-polarization ratios R_l^c/R_0^v ($l=0,\dots,3$) across the periodic table. The labels indicate the noble gases terminating periods.

the $3d$ subshell is filled. The relative magnitudes tend to decrease within the periods. On the contrary, the spin-polarization of f electrons results in small positive values of $\rho_c^s(0)$ in the sixth period. Taking into account the fact that the spin-polarization of valence s electrons is small too, the core spin-polarization in lanthanide compounds still may be important.

Chapter 5

Paramagnetic ions in water: *ab initio* molecular dynamics

5.1 Introduction

In Chapters 2 and 3, we modeled solvated aqua ions by means of cluster approach. Although this technique has fulfilled our needs for studying electron-nuclear interactions of the inner coordination sphere of aqua complexes, there exists another approach. This approach is based on the periodic boundary conditions. The solute molecule along with the predefined amount of solvent molecules fill a periodically repeated supercell. All solvation effects can be modeled explicitly in this way. Below, we will use this approach to assess the distant hyperfine interactions, in the outer coordination sphere. In addition, the supercell approach is the basic framework for the molecular dynamics simulations based on the density functional theory. The capability of classical force fields for modeling transition metal and lanthanide aqua ions in solutions and associated reactions is limited. First principles molecular dynamics has already proved to provide accurate descriptions of aqueous solutions of ions [141, 169–173]. Moreover, the electronic structure properties can be obtained on-the-fly, without any need of changing the computational model. In this Chapter, we extend the scope of *ab initio* simulated metal ions to paramagnetic Cr^{3+} and Gd^{3+} ions.

The choice of the Cr^{3+} ion was not random. Structure and dynamics of the first and second hydration shells of Cr^{3+} have been extensively studied in the last ten years both experimentally [174–180] and by means of classical MD simulations [177, 178, 181, 182]. The inert first coordination sphere, as well as strong hydrogen binding due to polarization

of first sphere water molecules, leads to a well structured second coordination sphere. A residence time of water molecules in the second sphere of 128 ps at 298 K could be measured by ^{17}O NMR due to a significant hyperfine interaction between the electron spin of Cr^{3+} and the ^{17}O nuclear spin [177]. In this Chapter we show that the measured Fermi contact hyperfine field of the second coordination sphere water molecules can be reproduced by means of the supercell approach. In the second part of the Chapter, we study the structure, dynamics and hyperfine interactions both in inner and outer coordination spheres of the Gd^{3+} aqua ion important for biomedical applications.

5.2 Methodology

Accurate calculation of the hyperfine parameters requires carefully designed pseudopotentials (see Chapter 4) which in turn require high plane wave kinetic energy cutoffs. The tight convergence of the wavefunction is another necessary condition for accurate hyperfine coupling calculations. Thus, HFCCs can not be calculated accurately from instant wavefunctions in Car-Parrinello simulations. Car-Parrinello MD simulations [131] do not follow Born-Oppenheimer surface precisely and the spin density distribution in the system tends to be more delocalized which may significantly decrease the accuracy of calculated hyperfine coupling constants. A quenching of the wavefunctions to the Born-Oppenheimer surface has to be performed. Finally, explicit description of the localized $4f$ states of the gadolinium ion is necessary for the calculation of hyperfine couplings. However, the lanthanide f electrons do not contribute to chemical binding and can be included in the pseudopotential core for performing molecular dynamics simulations. For the purpose of our study, we perform MD simulations using “soft” pseudopotentials. A set of atomic configurations is then extracted from the MD trajectory and the calculations of HFCCs are performed using “hard” pseudopotentials and a higher plane wave kinetic energy cutoff. In both cases we use the Becke exchange density functional [98] in combination with the Lee-Yang-Parr correlation density functional [183].

The periodically repeated simulation box consisted of a metal ion and 54 and 56 water molecules in the simulations of the solutions of Cr^{3+} and Gd^{3+} ions, respectively. Dimensions of the cubic boxes ($a=11.513 \text{ \AA}$ and $a=11.648 \text{ \AA}$, respectively) were calculated on the basis of the experimental values for the absolute molar volumes of the ions [184, 185] and assuming a water density of $1 \text{ g}\cdot\text{cm}^{-3}$. The first two coordination spheres of the ions entirely fit into the box of this size (see Fig. 5.1 for illustration). The 3+ charge of

the ions was neutralized by a uniform background charge in these simulations. The MD simulation was carried out for 2.5 ps and 4.0 ps for chromium(III) and gadolinium(III) ions, respectively, after an initial equilibration of 1 ps. Limitations due to short simulation time were compensated by the altered temperature which was kept around 350 K. Hyperfine coupling constants are in general not temperature dependent. The fictitious electron mass was set to 600 a. u. The time step used was equal to 5 a. u. (0.121 fs). Hydrogen nuclei were treated classically and had a mass of the deuterium isotope. For the MD simulation we used Vanderbilt ultrasoft pseudopotentials [186] for all elements. The [Ne] core configuration was used for the Cr^{3+} ion. The [Xe]4f⁷ core configuration with *f* electrons included in core was used for the Gd^{3+} ion. The plane-wave kinetic energy cutoff for valence electron wavefunctions was set to 30 Ry and 35 Ry, respectively.

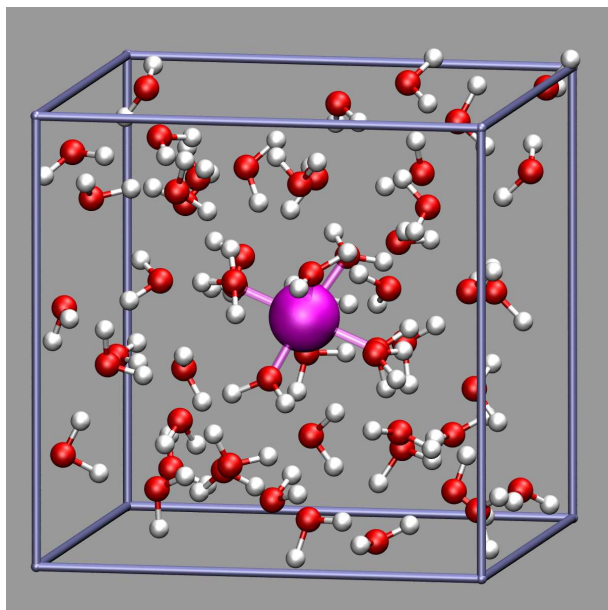


Figure 5.1: A typical configuration of the *ab initio* molecular dynamics simulation of Cr^{3+} with 54 water molecules in a cubic box at 350 K.

For the calculation of isotropic HFCCs in the Cr^{3+} ion solution, 5 snapshots were extracted from the MD trajectory in 0.5 ps intervals. Thus, 30 $A_{iso}(^{17}\text{O}_I)$ values, 60 $A_{iso}(^1\text{H}_I)$ values for first sphere water and approximately 60 $A_{iso}(^{17}\text{O}_{II})$ values for second sphere water are available for statistical analysis. The total amount of 270 values of $A_{iso}(^{17}\text{O})$ and 540 values of $A_{iso}(^1\text{H})$ was calculated for the whole system. A larger amount of data available from 14 snapshots extracted in 0.25 ps intervals has been used for the Gd^{3+} HFCC calculations. This results in 112 values of the inner sphere ^{17}O hyperfine couplings and 224 values of the inner sphere ^1H hyperfine couplings. The total amount of HFCCs was 784 and 1568 values for ^{17}O and ^1H nuclei, respectively.

This quantity of data is sufficient for reliable statistical analysis. The interval of time sampled is enough to provide the averaging over molecular vibrations in the system. Since stable coordination spheres were observed for both ions, we suggest that the simulation times used are enough to get accurate mean values. The statistical errors of the calculated hyperfine couplings are standard deviations of the mean. The valence wavefunctions in the calculations HFCCs were expanded in the plane wave basis set to cutoffs of 80 Ry and 140 Ry for the Cr^{3+} and Gd^{3+} calculations, respectively. In these calculations we used norm-conserving pseudopotentials [151] with a $[\text{Ne}]3s^23p^6$ core configuration for chromium. For gadolinium the core configurations was $[\text{Kr}]4d^{10}$. The nonlinear core correction [166] was used on chromium, gadolinium and oxygen. The wavefunctions were converged with the preconditioned conjugate gradient method using a maximum value of 10^{-6} for the largest element of the gradient of the wavefunction.

The ^1H water isotropic hyperfine coupling constants and valence contribution to ^{17}O water hyperfine coupling constants were calculated from pseudopotential spin density using the method of Van de Walle and Blöchl [147]. The $1s$ core spin-polarization contribution to ^{17}O hyperfine coupling constants and the dipolar hyperfine couplings were calculated using the methods described in the previous Chapter.

5.3 Discussion and results

5.3.1 Aqueous solution of Cr^{3+} : a test case

The Cr–O and Cr–H radial distribution functions (RDF) from the Car-Parrinello simulation are given in Fig. 5.2. The octahedral coordination sphere was stable and no first coordination sphere water exchange events were observed during the simulation. The average Cr– O_I distance in the first coordination sphere is 2.033 Å, and the average Cr– H_I distance is 2.696 Å. The Cr– O_I distance compares well with existing experimental values of 2.03 ± 0.02 Å (large angle X-ray diffraction [187]), 1.97–1.99 Å (X-ray diffraction [188–190]), 1.98 Å (neutron diffraction [191]), 1.97–2.01 Å (extended X-ray absorption fine structure [179, 180, 187]) and other theoretical studies [177](see also Table 1 in Ref. [177, 192–195] and Table 1 in Ref. [195]).

The Cr–O RDF shows a well pronounced second coordination sphere of Cr^{3+} in aqueous solution. The limit of the second coordination sphere, determined on the basis of the second minimum of CrO RDF, is 4.75 Å. The second sphere coordination number

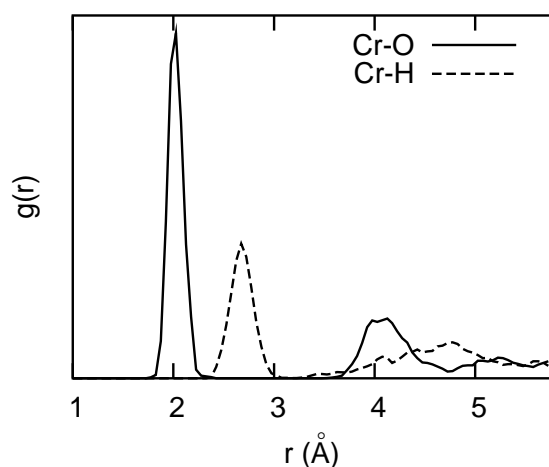


Figure 5.2: The Cr–O (full line) and Cr–H (dashed line) radial distribution functions (RDF).

is 12.6 and the average Cr– O_{II} distance is 4.17 Å. The available experimental data give values of 12–14 for the second sphere coordination number and 3.95–4.25 Å for the Cr– O_{II} distance [179, 188–191, 193, 194]. The combined QM/MM study [195] led to a slightly longer Cr– O_{II} distance of 4.36 Å and connected to the higher second sphere coordination number of 15.4.

The distribution of oxygen atoms of water molecules outside the first coordination sphere around first shell oxygen atoms, O_I , is shown in Fig. 5.3. From the maximum of the first peak a O_I – O_{II} distance of 2.67 Å is obtained. This value is markedly larger than the 2.41 Å found in a classic MD simulation [177]. However, the agreement with the results of classical MD using more sophisticated interaction potentials (2.58–2.60 Å [178, 196]) as well as experimental data (2.60–2.63 Å [187]) is very satisfactory.

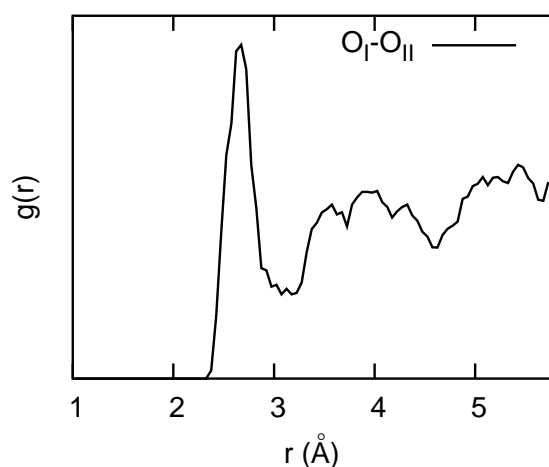


Figure 5.3: The RDF of water oxygen outside the first coordination sphere around first shell oxygen atoms O_I .

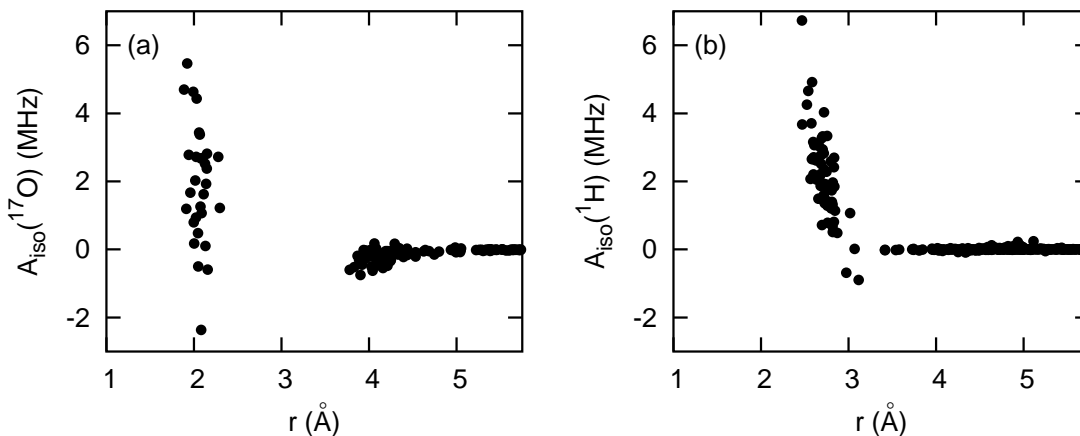


Figure 5.4: Isotropic scalar coupling constant on ^{17}O (a) and ^{17}H (b), as a function of the Cr–O and Cr–H distances, correspondingly, calculated from five snapshots.

Figure 5.4 shows the dependence of $A_{iso}(^{17}\text{O})$ and $A_{iso}(^1\text{H})$ on the Cr–O and Cr–H distances, respectively. The mean isotropic HFCC for first coordination sphere water molecules, $\langle A_{iso}(^{17}\text{O}_I) \rangle$, is equal to 1.9 ± 0.3 MHz which corresponds to a negative average value of spin-density on the $^{17}\text{O}_I$ nuclei, due to a negative gyromagnetic ratio for ^{17}O . This suggests a strong spin-polarization mechanism of the distribution of unpaired electron density in the first coordination sphere (Fig. 5.5a). However, the positive value observed for first shell water protons, $\langle A_{iso}(^1\text{H}_I) \rangle = 2.1 \pm 0.2$ MHz, corresponds to a positive value of spin density at the positions of $^1\text{H}_I$ nuclei. The $A_{iso}(^1\text{H}_I)$ values also show a clear dependence on the Cr– H_I distance (Fig. 5.4b). A possible explanation is that the spin-delocalization contribution (always positive) depends on the tilt angle θ for first sphere water molecules (Fig. 5.6) which is commonly defined as the deviation from a radial alignment of the water dipoles. The $A_{iso}(^{17}\text{O}_I)$ increases when θ approaches radial alignment of water dipoles, but at the same time $A_{iso}(^{17}\text{O}_I)$ shows no visible dependence on the Cr– O_I distance. However, $A_{iso}(^1\text{H}_I)$ decreases with θ approaching 180° , and shows therefore a dependence on the Cr– H_I distance with a negative slope. The experimentally measured value for $A_{iso}(^1\text{H}_I)$ is 2.1 MHz [44, 192], in perfect agreement with our calculations. No experimental $A_{iso}(^{17}\text{O}_I)$ value is available due to very slow exchange of first shell water molecules on Cr^{3+} .

Our calculations show also considerable spin-polarization of the second coordination sphere water molecules (Fig. 5.5b) leading to negative $A_{iso}(^{17}\text{O}_{II})$ values for the Cr–O distance values between 3.7 and 4.8 Å (Fig. 5.4a). It is worth noting that while the

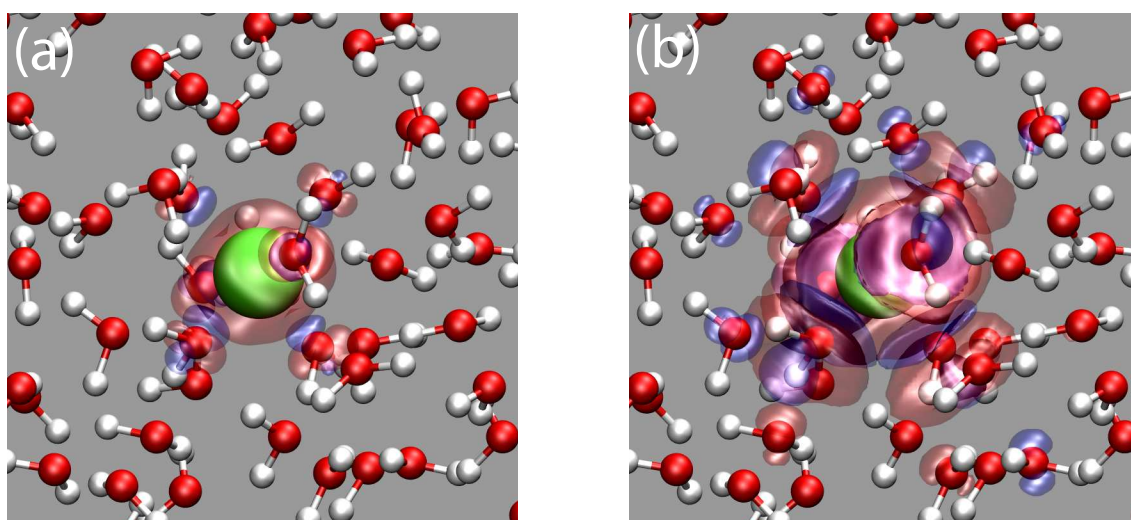


Figure 5.5: Isosurface plots of the spin-density distribution around the paramagnetic Cr^{3+} ion for an isovalue of 0.002 a.u.^{-3} (a) and 0.0001 a.u.^{-3} (b). The positive (excess spin) spin-density is shown in red and the negative spin density is shown in blue. The spin-polarization of second coordination sphere water molecules can be observed (b).

spin polarization over second coordination sphere bears mainly negative character (see Fig. 5.5b) the positive spin density at the positions of $^{17}\text{O}_{II}$ nuclei prevails. The average second sphere ^{17}O HFCC, $\langle A_{iso}(^{17}\text{O}_{II}) \rangle = -0.20 \pm 0.02 \text{ MHz}$, is an order of magnitude smaller than $\langle A_{iso}(^{17}\text{O}_I) \rangle$. Our calculated value is in agreement with the experimental values of -0.215 MHz and of -0.24 MHz (recalculated for a second sphere coordination number of 12) [177, 197]. An interesting feature is the change in sign of $A_{iso}(^{17}\text{O})$ from positive to negative between first and second coordination sphere. Such a behavior has been observed experimentally for $[\text{Ti}(\text{H}_2\text{O})_6]^{3+}$ [198]. The outer sphere chemical shift of the ^{17}O NMR resonance is about 5 % of the first sphere shift with a negative sign. Golding and Stubbs calculated as early as in 1979 isoshielding maps for a d^1 transition metal ion in a strong crystal field [199]. From their calculations, water oxygen sitting close to the triangular faces of the octahedron formed by the coordinated water molecules have opposite chemical shifts with respect to those on the vertices of the octahedron. Hyperfine coupling to second sphere water molecules is also observed on polyaminocarboxylate complexes of gadolinium(III), used as contrast agents in magnetic resonance imaging in medicine [45]. On these complexes, water exchange of the first sphere water molecule is relatively slow and an outer sphere term has to be used to fit the chemical shift data. This outer sphere term was suggested to be about 1/10 of the first sphere term which

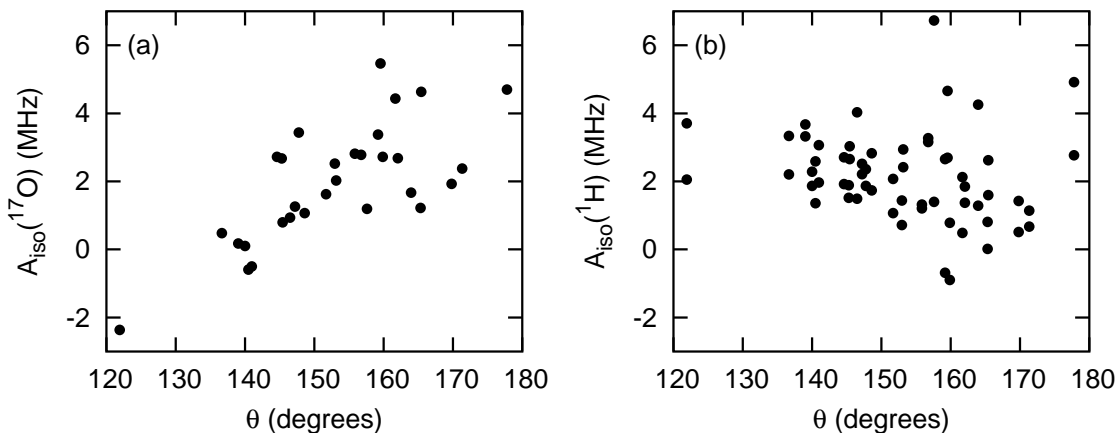


Figure 5.6: Isotropic scalar coupling constant on ^{17}O (a) and ^1H (b), as a function of the water molecule tilt angle θ .

agrees with our findings [18]. In the case of the Gd^{3+} aqua ion $[\text{Gd}(\text{H}_2\text{O})_8]^{3+}$ such a term could not be quantified because water exchange is very fast [101].

5.3.2 Hyperfine interactions in aqueous solution of Gd^{3+}

During the MD simulation of the gadolinium(III) ion in water a well defined first coordination sphere containing 8 water molecules (square antiprism coordination polyhedron with all water molecules being on average equivalent) was observed in agreement with experimental data [137]. The average inner sphere distances, $r_{\text{Gd}-\text{O}}=2.37 \text{ \AA}$ and $r_{\text{Gd}-\text{H}}=3.04 \text{ \AA}$ also agree very well with experimental results [69, 103, 105]. The Gd–O and Gd–H radial distributions functions are shown in Figure 5.7a. Our results also show close agreement with the Car-Parrinello simulations of Ikeda *et al.* [200, 201] performed for the diamagnetic yttrium(III) cation which is known to be the closest analog of the gadolinium(III) cation [69]. They have obtained 2.38 \AA average Y–O distance and the square antiprism as the most stable coordination polyhedron. However, free energy surface minima corresponding to other coordination numbers have been observed in their metadynamics simulations. For an individual inner sphere water molecule the Gd–O distance is subjected to fluctuations of large amplitude (between 2.1 \AA and 2.8 \AA). In the case of Gd^{3+} ion this interval is wider than in the case of Cr^{3+} ion with inert first coordination sphere. It is notable (Fig. 5.7b) that during the MD simulations the first coordination sphere undergoes dynamic distortions leading to significant elongation of

the Gd–O bond of individual water molecules. The Gd–O distance averaged over the first coordination sphere shows much smaller variation around the mean value.

The second coordination sphere is well pronounced but to a smaller extent comparing to other metal ions forming very stable and inert first coordination spheres (e.g. Cr^{3+} ion). The distance of closest approach to the Gd^{3+} ion for both O and H atoms of the outer coordination sphere water molecules is 3.8 Å. The corresponding maxima of the radial distribution functions are 4.6 Å and 5.0 Å, respectively.

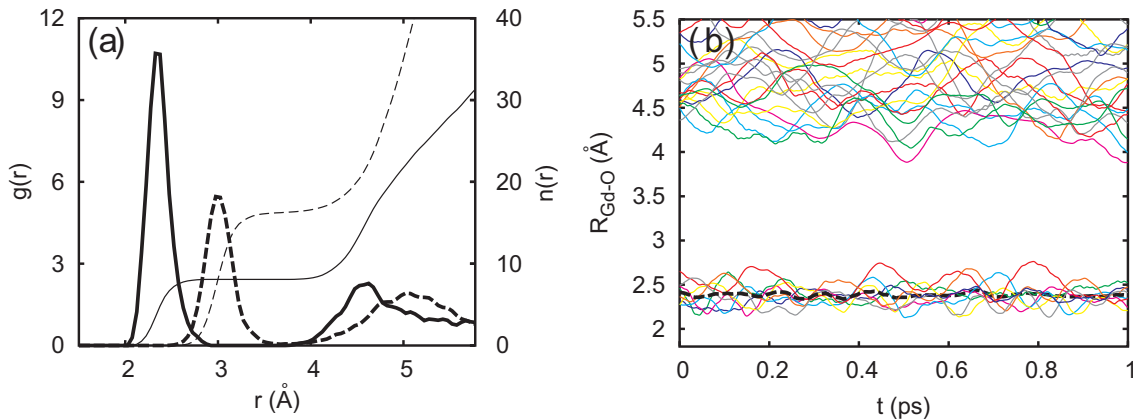


Figure 5.7: (a): Radial distribution functions $g_{\text{Gd-O}}(r)$ (thick solid line) and $g_{\text{Gd-H}}(r)$ (thick dashed line) for Gd^{3+} ion in liquid water. The thin lines represent the running coordination number $n(r)$. (b): Time evolution of the Gd–O distances $R_{\text{Gd-O}}$ during a representative 1 ps interval of the Car-Parrinello MD simulation. The black dashed line shows the time evolution of the average Gd–O distance for the inner coordination sphere water molecules.

The qualitative features of the electron spin density distribution are shown in Figure 5.8. The spin-polarization pattern of the eight inner sphere water molecules (Fig. 5.8a) is very similar to the one described in Chapter 2. The second part of the figure, Fig. 5.8b, shows the contour plot of the electron spin density in a plane passing through the Gd^{3+} ion. Apart from the spin-polarization of the inner sphere water molecules, one can note one spin-polarized outer sphere water molecule, though to a smaller extent. As in the case of the inner sphere water molecules, the spin-polarization affects primarily the lone pair orbitals of the water molecule.

The calculated Fermi contact HFCCs of the inner sphere water molecules are in agreement with the experimental data and the results of cluster calculations described in Chapter 2. The expectation value of the inner sphere ^{17}O HFCC, $\langle A_{\text{iso}}(^{17}\text{O}_I) \rangle = 0.65 \pm 0.03$ MHz, compares to the reported experimental values ranging from 0.75 MHz

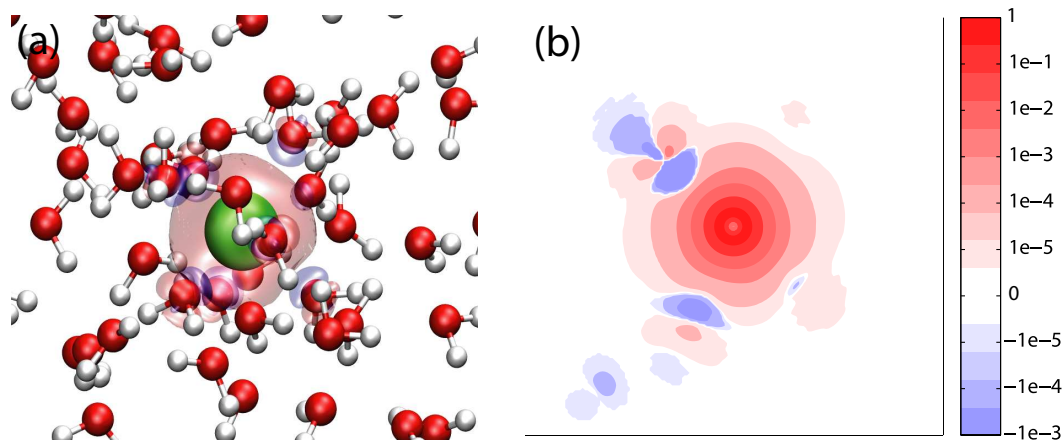


Figure 5.8: (a) Atomic structure and isosurface plot of the spin density around Gd^{3+} ion in solution. Red surfaces correspond to $0.0002 \text{ a. u.}^{-3}$, blue surfaces correspond to $-0.0002 \text{ a. u.}^{-3}$ values. (b) Contour plot of the the spin-density distribution in a plane passing through Gd^{3+} ion. An area of $10 \text{ \AA} \times 10 \text{ \AA}$ is shown. The Gd^{3+} ion, located in the middle, gives rise to a positive magnetization density of large magnitude. The anisotropic spin polarization of four inner sphere and one outer sphere water molecules can be also recognized on the plot.

to 0.84 MHz [18, 102, 105], and 0.61 MHz predicted by the BPW91/ZORA/TZ2P calculations described in Chapter 2. The values of the ^{17}O HFCCs are spread over the broad interval $[-0.04 \text{ MHz}; 1.26 \text{ MHz}]$ and shows a pronounced dependence on the Gd–O distance (Fig. 5.9a). Similarly, the inner sphere ^1H HFCC shows a strong dependence on the Gd–H distance (Fig. 5.9b). The mean value $\langle A_{iso}(^1\text{H}_I) \rangle = 0.085 \pm 0.005 \text{ MHz}$ is larger than the experimental values $0.03 \pm 0.02 \text{ MHz}$ [102] and 0.04 MHz [105] as well as the value of 0.025 MHz obtained in our previous calculations for the model aqua complex with a longer Gd–O distance of 2.40 \AA . However, in terms of absolute value this difference is very small: both experimental and theoretical values are close to zero.

The mean value of the second coordination sphere ^{17}O HFCC, $\langle A_{iso}(^{17}\text{O}_{II}) \rangle = -0.005 \pm 0.001 \text{ MHz}$, is calculated supposing an upper limit of the second coordination sphere at $r_{\text{Gd-O}} = 6 \text{ \AA}$. The largest values of $A_{iso}(^{17}\text{O}_{II})$ are observed for the water molecules closest to the Gd^{3+} ion (Fig. 5.9a, inset). The outer sphere ^1H HFCC is almost zero, $A_{iso}(^1\text{H}_{II}) = 0.00027 \pm 0.00007 \text{ MHz}$. The ligand hyperfine couplings of the Gd^{3+} aqua ion show the same qualitative trends as for the solvated Cr^{3+} ion discussed previously. However, both the absolute magnitudes of the HFCCs and the ratios of the outer sphere HFCCs to the inner sphere couplings are smaller in the Gd^{3+} case. This can be attributed to a more

organized character of the Cr^{3+} second coordination sphere involving a strong hydrogen bonding between the water molecules of the two coordination spheres.

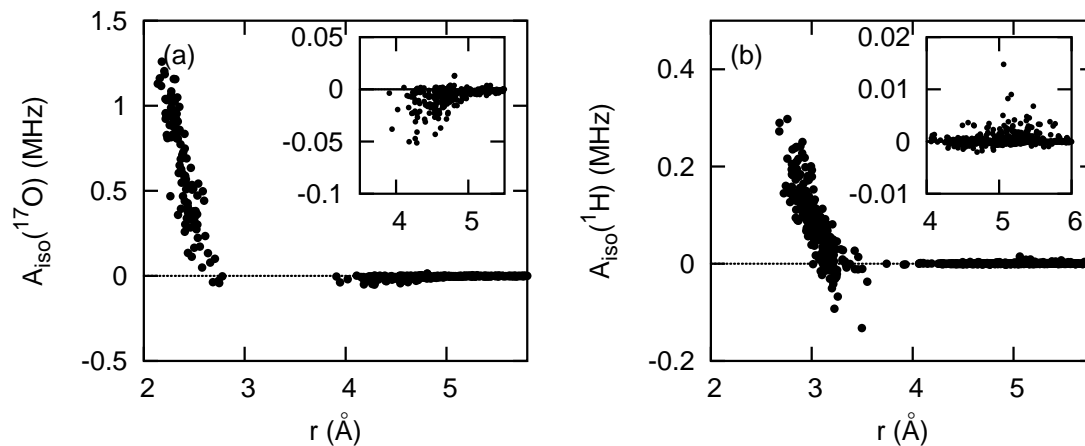


Figure 5.9: Isotropic hyperfine coupling constants as a function of the distance to Gd^{3+} ion for ^{17}O (a) and ^1H (b) nuclei. Insets show the values for second coordination sphere water molecules.

As it was done in Chapter 2, the dipolar HFIs are expressed in terms of the effective distances, r_{eff} . Figure 5.10 shows the enhancement factors of the dipolar interaction, $(r/r_{eff})^3$. In agreement with the results of Chapter 2, the ^{17}O dipolar HFIs are partially screened due to the spin-polarization. The average value is $\langle (r/r_{eff})^3(^{17}\text{O}) \rangle = 0.91$ and the screening become stronger with decreasing the Gd–O distance. The dipolar interactions of the ^{17}O nuclei of the second coordination sphere water molecules are enhanced in respect to what is expected from the point-dipole approximation and its magnitude is largest for the water molecules closest to the Gd^{3+} ion. However, the enhancement is relatively weak and does not exceed 3% (Fig. 5.10a). The screening of the ^1H dipolar HFIs in the inner coordination sphere is very small, $(r/r_{eff})^3(^1\text{H})=0.995$. The effects of the spin-polarization on the anisotropic ^1H HFIs in the outer sphere are negligible.

In conclusion, we have studied the structure, dynamics and ligand hyperfine couplings of bulk aqueous solutions of paramagnetic Cr^{3+} and Gd^{3+} ions using ab initio molecular dynamics techniques. The primary emphasis is on the HFIs of the water molecules in the outer sphere of the Gd^{3+} ion. The calculated isotropic HFCCs values for the inner sphere water molecules and for the Cr^{3+} second sphere water molecules agree well with the experimental data. The Gd^{3+} outer sphere isotropic HFCCs are weaker than those

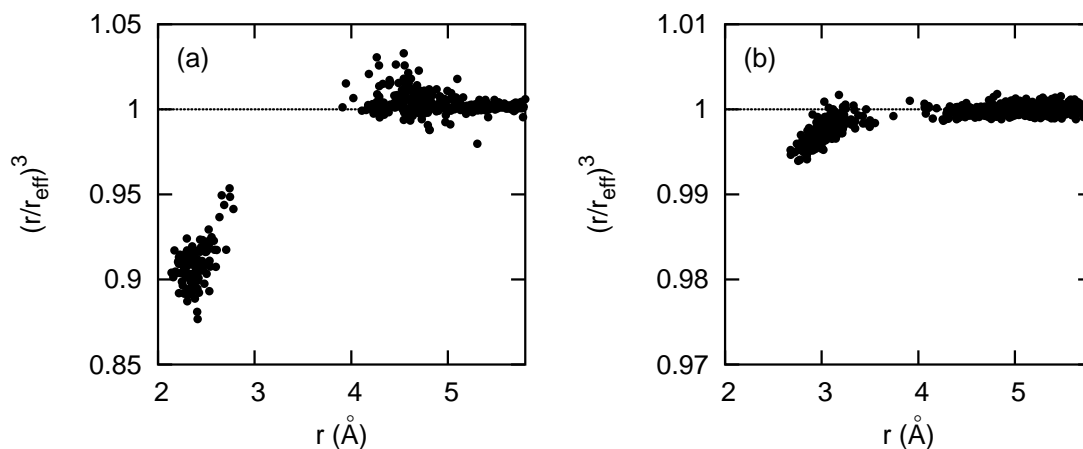


Figure 5.10: Dipolar hyperfine interaction enhancement factors as function of distance to Gd^{3+} ion for ^{17}O (a) and ^1H (b) nuclei.

calculated for Cr^{3+} . The magnitudes of the Fermi contact HFCCs in the outer sphere are about two orders of magnitude smaller than in the inner sphere. In the case of Cr^{3+} ion the spin-polarization of outer sphere water molecules is more pronounced due to the higher degree of organization of the second coordination sphere. We expect that in poly(amino carboxylate) complexes of Gd^{3+} the outer coordination sphere may be better organized in the vicinity of carboxylate groups compared to the octa aqua ion. The dipolar HFIs are well described within the point-dipole approximation with the exception of ^{17}O dipolar interactions in the inner coordination sphere.

Chapter 6

Hyperfine interactions in carbon nanostructures

6.1 Introduction

In this Chapter, we consider hyperfine interactions in a different class of atomic structures - in carbon nanostructures. Carbon nanostructures have attracted enormous interest due to the broad diversity of atomic structures and topologies and due to their unusual physical properties. Graphene, a honeycomb-patterned single layer of graphite, is considered as a predecessor of the class of carbon-based nanostructures. Its closest relatives include fullerenes, carbon nanotubes (CNTs), carbon nanohorns, nanofoams, etc. Outstanding electronic properties of these materials promise many applications of carbon nanostructures in technology, more specifically, as the components of future nanometer-sized electronic devices, nanoelectromechanical systems, conducting composites and many more [21]. A general understanding of hyperfine interactions in carbon nanostructures is an important part of the progress in this field because of the following two reasons.

Firstly, probing HFIs with nuclear magnetic resonance (NMR) or electron spin resonance (ESR) techniques provide an information about structure and dynamics of materials [202, 203]. Consider an example of carbon nanotubes, which are presently produced in large quantities. For instance, CNTs may be either metallic or semiconducting [27, 204] with the electronic properties depending on their atomic structure which is commonly characterized by the pair of chirality indices, (n,m) , as explained in Introduction. Efficient methods for separation of metallic and semiconducting CNTs and their further purification have been developed [205]. At this stage, the nuclear magnetic resonance

(NMR) technique widely used in chemistry and material science can be applied to the study of the composition of CNT samples. However, performing NMR experiments on CNTs is by no means trivial and promising results have been achieved only recently. The ^{13}C nuclear spins of semiconducting and metallic CNTs have been identified by means of spin-lattice relaxation rate measurements [206], and NMR spectra of single-wall CNTs, purified from paramagnetic impurities, have been obtained [207]. In the latter case, the NMR signal has been resolved into the contributions of semiconducting and metallic CNTs at a ppm-level resolution. As we will show below, the HFIs make an important contribution to the NMR chemical shift of metallic carbon nanotubes.

Secondly, graphene and related carbon nanostructures are considered as potential building blocks for the alternative approaches of future electronics: spintronics [32], exploiting the electron spin degree of freedom, and quantum information processing, operating with electron spins [208] or nuclear spins [209]. Carbon nanostructures are attractive for this applications because of the negligible spin-orbit coupling [210, 211], which is the primary source of the electron spin decoherence in heavy element compounds. Promising results for the coherent electron spin transport in carbon nanotubes [33–35, 212, 213] indicate potential of these materials. Single electron devices based on carbon nanotubes have also been recently studied [214, 215]. In this prospective the HFIs are expected to be the leading contribution to the spin decoherence in carbon materials [210, 213, 216]. Minimizing HFIs with nuclear spins is necessary for achieving longer electron spin coherence times [217] while in some instances the HFIs play an important role of the link between the spins of electrons and nuclei in the system [209, 218–220]. A common understanding of HFIs is therefore necessary for engineering efficient devices for spintronics and quantum information processing applications based on graphenic nanostructures.

The rest of this Chapter is divided in two parts. In the first part we study in details the contribution of HFIs to the NMR chemical shift, so called Knight shift, in metallic CNTs. In the second part, we aim understanding of HFIs in graphenic nanostructures in its broadest sense, i.e. how does a spin polarized π electron with an arbitrary distribution in an arbitrary carbon nanostructures is coupled to nuclear spins?

6.2 Isotropic Knight shift of metallic carbon nanotubes

The shift of the Larmor frequency of the nuclear spin is described by the chemical shift tensor, $\overleftrightarrow{\delta} = \overleftrightarrow{\sigma}_{ref} - \overleftrightarrow{\sigma} + \overleftrightarrow{\mathbf{K}}$, which is defined by the magnetic shielding relative to a standard reference, $\overleftrightarrow{\sigma}_{ref} - \overleftrightarrow{\sigma}$, and the Knight shift tensor $\overleftrightarrow{\mathbf{K}}$, which originates from the Pauli paramagnetism, occurring only in metals [221]. In the same way as it was done in the previous chapters for the HFI tensor, we split the Knight shift tensor and the chemical shift tensor into the scalar isotropic parts (e.g. $K_{iso} = \frac{1}{3}Tr[\overleftrightarrow{\mathbf{K}}]$ for the Knight shift contribution) and the remaining traceless anisotropy tensors. In reality solid samples of carbon nanotubes are orientationally disordered. The isotropic chemical shift δ_{iso} and partial information about chemical shift anisotropy tensor can be obtained from the static NMR measurements of such samples. Moreover, high resolution solid state NMR experiments are often performed under isotropic averaging conditions such that only isotropic quantities are measured. Latil *et al.* [222, 223] theoretically predicted a separation of about 11 ppm between the isotropic chemical shifts of metallic and insulating CNTs due to the London ring current contribution to the magnetic shielding. However, they have concluded that the ring current contribution does not provide more details about the atomic structure of CNTs which is commonly characterized by the pair of chirality indices, (n, m) .

The isotropic Knight shift,

$$K_{iso} = \frac{A_{iso}}{\gamma_e \gamma_n \hbar^2} \chi_p = \frac{8\pi}{3} (\langle |\psi|^2(0) \rangle + \eta) \chi_p, \quad (6.1)$$

is closely related to the isotropic hyperfine coupling constant and originates from the Fermi contact HFI involving the conduction electrons. One can separate the contributions due to the effects of (i) the conduction electrons, which is proportional to the squared magnitude of conduction band wavefunction at the point of the nucleus, $\psi(0)$, and (ii) the ensemble of spin-polarized valence bands and atomic core states [224, 225]. The later contribution can be collected in the common parameter η . The Pauli spin susceptibility, $\chi_p \approx 2\mu_B^2 g(\epsilon_F)$, is proportional to the density of states at the Fermi level, $g(\epsilon_F)$. Thus, K_{iso} provides an information about the conduction states which can be related to the atomistic structure of the metallic system under investigation.

In a single two-dimensional graphite layer, graphene, $\psi(0) = 0$ because conduction bands have π -character and all nuclei lie in the nodal plane of these states. Rolling up

the graphene sheet into a carbon nanotube causes partial sp^2 - sp^3 rehybridization which means that the π states receive some s -character rapidly increasing with a decreasing CNT diameter. The rehybridization contribution to isotropic Knight shift is positive. The Knight shifts are relatively well studied for the kindred class of conducting compounds, alkali metal graphite intercalates, in which individual graphene sheets maintain their planarity. Negative isotropic Knight shifts up to 100 ppm in magnitude were measured experimentally [226] for these systems. However, the density of states at the Fermi level in graphite intercalates is higher compared to that of metallic carbon nanotubes [27, 204]. This reduces the estimates of the negative spin-polarization contribution to the order of several ppm.

Other possible contributions to isotropic Knight shifts in CNTs concern ultranarrow, chemically modified, bundled and multi-walled CNTs. (i) It has been shown by first principles calculations [227, 228] that $(n,0)$, $(n=3-6)$ single-wall CNTs (termed irregular CNTs below, regular otherwise) are true metals. The density of states at the Fermi level, $g(\epsilon_F)$, is higher than predicted by the zone folding approximation [27, 204] and the conduction bands might have higher s -character in these cases. (ii) For chemically functionalized CNTs additional possibilities can be exploited. A chemical modification may change both $g(\epsilon_F)$ as well as the spatial character of the conduction states. In addition, introduced nuclei of functional groups may also experience isotropic Knight shifts. This suggests to perform NMR measurements on nuclei other than ^{13}C in order to probe the conduction states of a sample. (iii) Nanotube bundling may affect the band structure of CNTs by breaking the metallicity of otherwise metallic CNTs or closing the gap in semiconducting ones. The pseudogap opening in conducting nanotubes has been observed experimentally and studied theoretically [229, 230] while the band gap closing in otherwise semiconducting nanotubes was predicted theoretically [231]. Reich *et al.* showed in their computational study [231] that in $(10,0)$ nanotube bundles the gap between π and π^* bands closes due to the dispersion perpendicular to the nanotube axis. The curvature-induced metallization of double-wall semiconducting nanotubes has also been predicted recently [232].

Unlike its isotropic contribution, the Knight shift anisotropy originates from the dipole-dipole interaction between the electron spin and the nuclear spin. The dipolar contribution can be accessed by analyzing the static line shape of the NMR spectrum or through the nuclear relaxation rate measurements. In case of conducting CNTs, the dipolar Knight shift originates from the direct contribution of conduction π -states and

almost unaffected by spin-polarization and sp^2 - sp^3 rehybridization effects [202]. Its value provides a direct information about $g(\epsilon_F)$ what was used in a number of studies of carbon nanotubes and graphite intercalation compounds [206, 222, 223, 233].

6.2.1 Computational methods

The computational method we use is based on the all-electron density functional theory (DFT) approach within periodic boundary conditions [234] implemented in the GAUSSIAN03 code [88]. Following the methodology of Weinert *et al.* [235], we perform unrestricted self-consistent field (SCF) calculations with arbitrary external magnetic field H . In order to keep the numerical errors of the SCF calculations small it is necessary to apply strong magnetic fields, about two orders of magnitude stronger than the ones conventionally used in NMR measurements. For instance, in case of the (6,6) CNT calculation an external magnetic field of 1.3×10^7 G was applied in order to achieve magnetization of 0.002 electrons per atom. The corresponding Fermi contact hyperfine field at the ^{13}C nuclei is about 21 G in this calculation. We confirmed that for these systems such strong external fields are still in the linear regime for the change of the hyperfine field with respect to the external one. The calculated isotropic Knight shift,

$$K_{iso} = \frac{8\pi}{3} \gamma_e \frac{\rho^\uparrow(0) - \rho^\downarrow(0)}{H}, \quad (6.2)$$

with γ_e being the electron gyromagnetic ratio and $\rho^{\uparrow(\downarrow)}(0)$ being the spin-up(down) electron density at the nucleus site. The SCF approach permits to include explicitly contributions coming from the magnetization of the conduction electrons, possible spin-polarization effects and the exchange-correlation spin susceptibility enhancement [236].

The Becke exchange [98] and Lee-Yang-Parr correlation [183] generalized gradient approximation density functionals and Dunning's D95(d) Gaussian-type orbital basis set [237] have been used in our calculations. In this basis set both valence and core functions are double split as a necessary condition for an accurate description of spin-polarization. We found that this basis set is a reasonable compromise between accuracy and computational cost. In order to check the accuracy of this combination of basis set and density functional we have performed test calculations of ^{13}C isotropic hyperfine coupling constant for the planar CH_3 -radical. A number of detailed experimental works and theoretical calculations are available for this simple radical. In this system the unpaired electron resides on an orbital of pure p -character. Thus, the Fermi contact contribution

of the singly occupied molecular orbital to the ^{13}C isotropic hyperfine coupling constant is zero like in a graphene sheet. This isotropic coupling can be reproduced with good accuracy by DFT calculations (see e. g. Ref. [238]). At the chosen level of theory the calculated ^{13}C isotropic hyperfine coupling constant of the CH_3 -radical amounts to 26.40 G, while the BLYP basis set limit value is 26.13 G. The coupled-cluster singles and doubles (CCSD) theory in combination with D95(d) basis set gives 27.72 G. All these results compare well with the experimental value of 28.4 G determined by Chipman [239] for the planar radical. The crucial step for an accurate calculation of Knight shifts using self-consistent approach is the Brillouin zone integration. We have used an interpolative approach, which is a one-dimensional version of the linear tetrahedron method [240–243]. No thermal smearing has been applied. In all our calculations the uniform Brillouin zone integration mesh consists of 512 \mathbf{k} -points.

We have restricted our consideration to conducting armchair (n,n) (n=3-12) and zigzag (n,0) (n=3-6,9,12,15) nanotubes which have diameters up to 1.6 nm. The structures of these nanotubes have been generated [244] assuming a 1.421 Å carbon-carbon bond distance. The geometries of the ultranarrow zigzag nanotubes (n,0) (n=3-6) have been relaxed at the same level of theory as the one used for the calculation of Knight shifts. This is necessary since an effect of the bond length alternation [245] becomes important for ultranarrow CNTs. The small curvature-induced band gaps [246] in wider zigzag CNTs have not been taken into account.

6.2.2 Results

The calculated values of K_{iso} for regular metallic CNTs are shown in Fig. 6.1 as a function of their diameter. The shifts have been predicted to be negative for the CNTs with diameter larger than 0.5 nm while a positive value of 5.4 ppm has been predicted for the narrow (3,3) CNT. We explain the observed trend as the sum of the contributions due to the spin-polarization for the flat graphene sheet (K_{iso}^{sp}) and due to the curvature-induced rehybridization (K_{iso}^{rh}). The spin-polarization contribution is proportional to the density of states at the Fermi level, $K_{iso}^{sp} = B \cdot g(\epsilon_F)$ ($g(\epsilon_F)$ is the density of states at the Fermi per carbon atom). The negative constant B equal to $-228 \text{ ppm} \cdot \text{eV} \cdot \text{spin}$ has been predicted on the basis of calculations for the flat graphene sheet. This result can be compared to the experimental range between -530 and $-270 \text{ ppm} \cdot \text{eV} \cdot \text{spin}$ for MC_n (M = K, Cs; $x \geq 8$) graphite intercalation compounds [226].

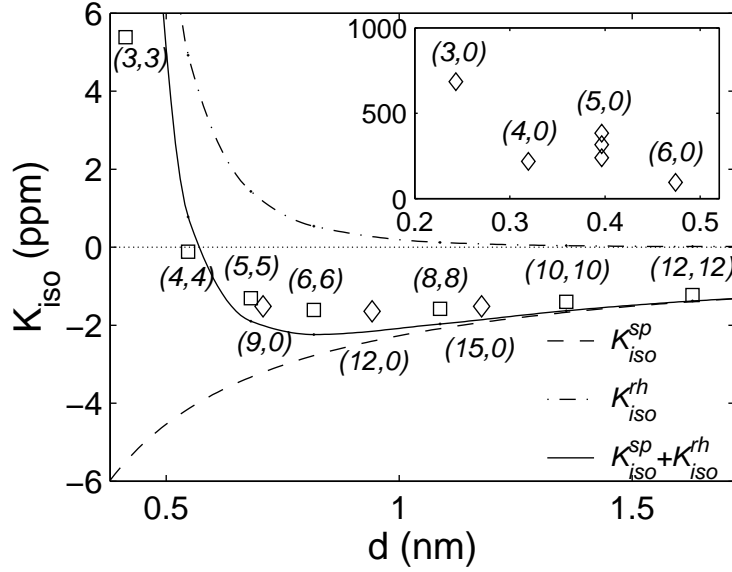


Figure 6.1: Isotropic Knight shifts of conducting single-wall CNTs. In regular metallic nanotubes K_{iso} shows dependence on the nanotube diameter as a result of interplay between the spin-polarization (K_{iso}^{sp}) and the rehybridization (K_{iso}^{rh}) contributions. The squares and diamonds indicate the calculated shifts for armchair and metallic zigzag CNTs, correspondingly. The curves show the estimated shift as a function of the CNT diameter d and its individual contributions (see text). Isotropic Knight shifts of ultranarrow conducting CNTs are shown in the inset. Three different types of ^{13}C nuclei in (5,0) CNT can be recognized.

The SCF spin-density induced by the external magnetic field is shown in Fig. 6.2. The positive spin-density due to the direct magnetization of the graphene π and π^* conduction band electrons prevails. However, negative magnetization has been observed in the graphene plane ($z=0$). The magnetization achieves absolute maxima at the sites of carbon nuclei. This can be explained by both negative $1s$ core and $2s$ spin-polarization. The rehybridization contribution is estimated as $K_{iso}^{rh} = 8\pi/3(m\psi_{2s}^2(0))\chi_p$, where m is the s -content of the π -orbital as defined in the π -Orbital Axis Vector (POAV) analysis [247] and $\psi_{2s}(0)$ is the magnitude of the carbon atom $2s$ wavefunction at the point of the nucleus. This contribution is significant only for the narrowest CNTs and increases very fast with decreasing diameter. It is remarkable that the estimated trend in Knight shifts reproduces calculated values.

From our calculations we conclude that the isotropic Knight shift of average diameter ($d > 0.6$ nm) metallic CNTs is on the order of 1-2 ppm towards lower frequencies. These

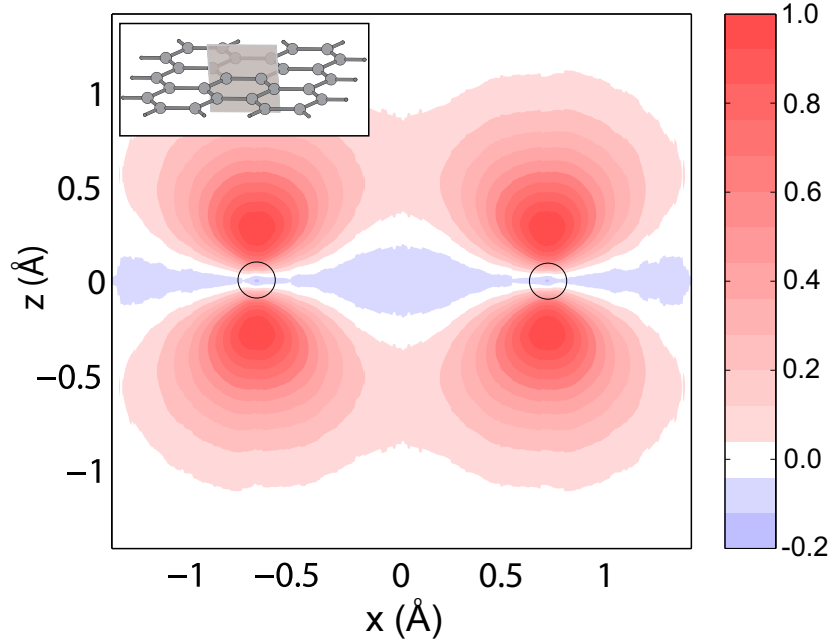


Figure 6.2: Calculated SCF spin-density (arb. units) for flat graphene sheet in an external magnetic field in the plane passing through the C-C bond and orthogonal to the graphene sheet (see inset). Positions of carbon atoms are indicated by circles.

values can be compared to the difference of about 8 ppm between the chemical shifts of semiconducting and metallic single-wall CNTs obtained experimentally using solid-state NMR [207]. This experimental value is 3 ppm smaller than the difference of 11 ppm, theoretically predicted when taking into account only ring current effects. The calculated negative isotropic Knight shift may explain the difference in predicted and experimentally observed values. Knight shifts of wider ($d > 1.6$ nm) CNTs, which are not considered here can be obtained by means of extrapolation based only on the graphenic spin-polarization contribution. Rehybridization contribution can safely be neglected for wider CNTs. In this case, a measured Knight shift reflects the density of states at the Fermi level in a direct way.

Ultrathin irregular CNTs show much larger, compared to wider CNTs, positive isotropic Knight shifts (Fig. 6.1, inset) as a result of significant rehybridization of the conduction band states and higher $g(\epsilon_F)$. The highest predicted value is +685 ppm for the (3,0) nanotube. For the (5,0) single-wall CNT, three types of nuclei can be distinguished because this CNT is predicted to be slightly flattened. Similar observations concerning the geometry of the (5,0) CNT have been made in Ref. [234].

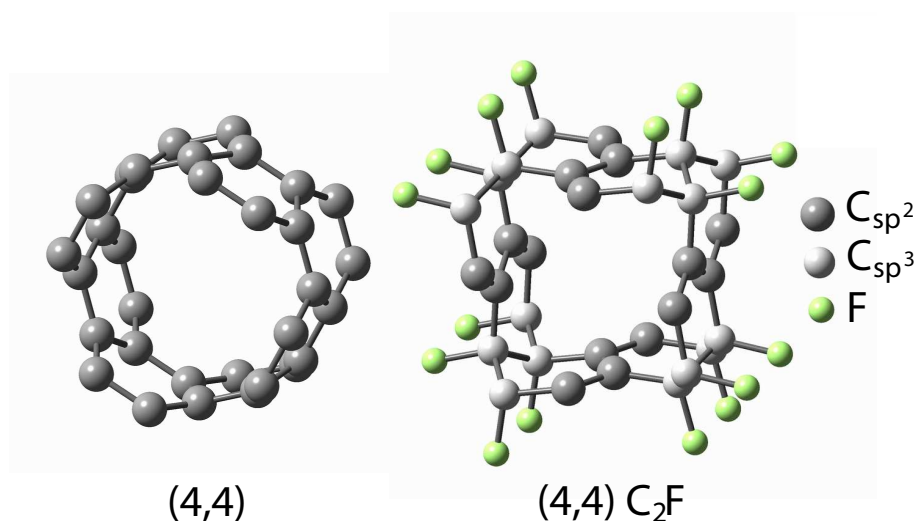


Figure 6.3: Atomic structures of unmodified and fluorinated (4,4) CNTs. The hybridization states of carbon atoms are indicated. Two unit cells are shown in both cases.

As an example of a chemically functionalized system, the isotropic Knight shifts of the fluorinated (4,4) armchair CNT [248] have been calculated. The stable configuration of the single-wall (4,4)-C₂F CNT is taken from the computational study of Bettinger *et al.* [249]. For the benefit of the reader, the structure of the unmodified and fluorinated (4,4) CNTs are shown in Fig. 6.3. In this case chemical functionalization causes complete rehybridization to sp^3 state of half of the carbon atoms without breaking the metallicity. The contribution of these atoms to the conduction states is smaller but their relative s -contribution is higher. Thus, a positive Knight shift for such atoms is expected. The other atoms are arranged into flat “strips” which are responsible for conductivity. A negative graphenic shift is expected on the nuclei of C _{sp^2} atoms. Chemical modification also leads to an increase of $g(\epsilon_F)$ in this case, $0.063 \text{ (eV}\cdot\text{spin)}^{-1}$ compared to $0.020 \text{ (eV}\cdot\text{spin)}^{-1}$ for the unmodified (4,4) CNT ($g(\epsilon_F)$ is the density of states at the Fermi per sp^2 carbon atom). Our calculations predict -7.5 ppm , $+18.6 \text{ ppm}$ and $+21.3 \text{ ppm}$ isotropic Knight shifts for the nuclei of C _{sp^2} , C _{sp^3} and F atoms, respectively. The difference in Knight shifts among the two types of carbon nuclei is 26.1 ppm . Thus the Knight shift contribution to the total chemical shift is of similar order of magnitude with the typical difference (about 100 ppm) in orbital chemical shifts of C _{sp^2} and C _{sp^3} nuclei. In addition, the Knight shift anisotropy of C _{sp^3} and of F nuclei is smaller compared to that of C _{sp^2} nuclei what favors the observation of narrow NMR signals.

Our results show that the isotropic Knight shifts of metallic CNTs, except ultranarrow ones, reflect the density of states at the Fermi level. High-resolution NMR can be used to study the distribution of diameters of conducting CNTs in a sample. Ultranarrow zigzag CNTs possess large positive isotropic Knight shifts characteristic of their chirality indices. Knight shifts can serve as the spectroscopic signatures of these unusual structures. Finally, Knight shift measurements can be useful to study chemically functionalized CNTs. The results of our theoretical study provide a new perspective for studying carbon nanostructures using NMR.

6.3 Hyperfine interactions in graphenic nanostructures

In the first part of this Chapter, we considered an important situation of the uniform distribution of the conduction electron spin density in the system. In other words, this situation corresponds to the case of infinitely long ideal CNTs. In this part, we follow a different approach. We try to figure out how the arbitrarily distributed conduction electron spin is coupled to the nuclear spins in the system. In many practical situations, the conduction electron distribution can be found using simpler computational approaches, e. g. tight binding method or analytical approximations. To achieve this goal, we study HFIs in small molecular fragments, a bottom side of the nanoscale regime, but using a more accurate all-electron basis set and the hybrid exchange-correlation density functional. The consideration is extended to involve curved topologies and the presence of heteronuclei due to impurities and boundaries.

Once again, the HFI tensor $\overleftrightarrow{\mathbf{A}}$ is decomposed into the scalar hyperfine coupling constant A_{iso} and the dipolar HFI tensor $\overleftrightarrow{\mathbf{T}}$. The electron spin density $\rho^s(\mathbf{r})$ can be further decomposed into the contribution of half-populated conduction electron states lying close to the Fermi level (or singly occupied molecular orbitals in the molecular context), $\rho_c^s(\mathbf{r}) = \sum_c |\psi^c(\mathbf{r})|^2 \geq 0$, and the contribution of the fully populated valence states perturbed by the spin-polarized conduction electrons, $\rho_v^s(\mathbf{r}) = \sum_v |\psi^{v\uparrow}(\mathbf{r})|^2 - |\psi^{v\downarrow}(\mathbf{r})|^2$. The spin-polarization of the valence electrons is illustrated with a model hydrogen-terminated graphene fragment in the triplet spin state (Fig. 6.4). While the projection of $\rho_c^s(\mathbf{r})$ on the xy plane (Fig. 6.4a) is positive everywhere and reveals an enhancement at the zig-zag edges, the projection of the total spin-density $\rho^s(\mathbf{r})$ (Fig. 6.4b) is negative where $\rho_c^s(\mathbf{r})$

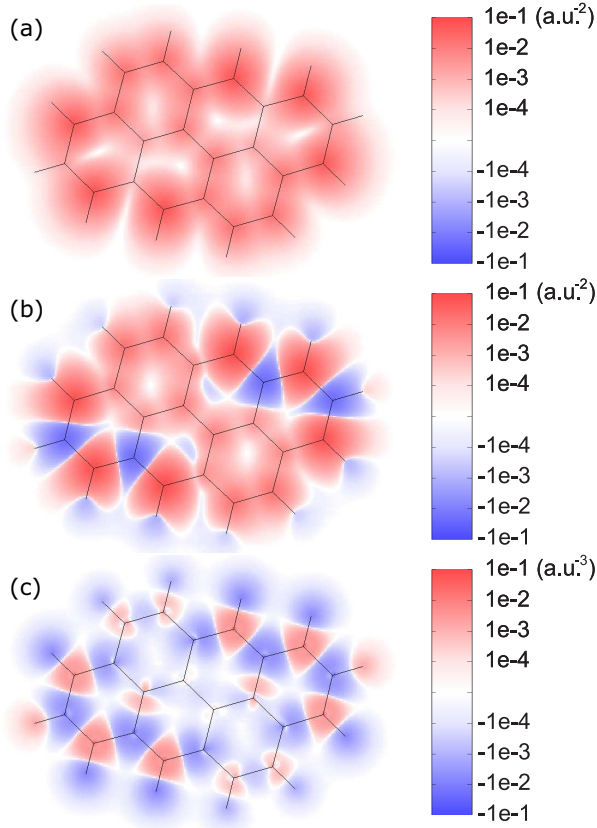


Figure 6.4: Projections of the spin-polarized conduction electron density $\rho_c^s(\mathbf{r})$ (a) and the total spin density $\rho^s(\mathbf{r})$ (b) on the plane of a small nanographite molecule in its triplet spin state. The magnitudes of the total spin density $\rho^s(\mathbf{r}, z=0)$ (c) in the plane of nuclei reflects the isotropic hyperfine field. Molecular framework is shown by black lines.

is close to zero. For the ideal graphene and planar sp^2 carbon nanostructures (all nuclei lie in the $z=0$ plane) $\rho_c^s(z=0)=0$ due to the p_z symmetry of the conduction states, although the sp^2 - sp^3 rehybridization of conduction states due to the curvature effects or chemical functionalizations may lead to the positive $\rho_c^s(z=0)$ contribution [202, 238]. However, there is a contribution of the σ symmetry valence states $\rho_v^s(z=0) \neq 0$ due to the spin-polarization effect. For the model graphene fragment $\rho_v^s(z=0)$ (Fig. 6.4c) shows an alternating pattern with the relative dominance of the negative spin density. Since the σ bands are situated well above and well below the Fermi level in the graphenic nanostructures, the valence spin-polarization phenomenon exhibit the property of locality. This property has been exploited by Karplus and Fraenkel almost 50 years ago to describe the isotropic ^{13}C HFCCs in conjugated organic radicals [250]. The main contribution to the hyperfine anisotropy originates from the total spin population n of the on-site p_z atomic orbital, which also incorporates the contribution of spin-polarized valence states. Assuming a local axial symmetry, $\overleftrightarrow{\mathbf{T}}$ can be written as a diagonal matrix with elements $T_{zz}/2 = -T_{xx} = -T_{yy} = A_{dip}$, where $A_{dip} = \frac{2}{5} \gamma_e \gamma_I \hbar^2 n \langle 1/r_{2p}^3 \rangle$ (r_{2p} is the distance

of the carbon $2p$ electron to nucleus). Although n is largely defined by the on-site contribution of the half-filled conduction π electron states, a significant contribution from the spin-polarization of the filled valence states can also be expected.

The all-electron density functional theory calculations on molecular graphenic nanostructures have been performed using the GAUSSIAN03 code [88]. The combination of the EPR-III Gaussian-type orbital basis set [251] specially tailored for the calculations of HFCCs and the B3LYP hybrid density functional [98, 100, 183] has been used. All molecules have been relaxed using the 6-31G** basis set. This computational protocol can be applied to molecules of limited size and provides HFCC values in excellent agreement with experimental results [252]. For a representative set of experimentally measured ^{13}C HFCCs in small graphenic ion-radicals [253–255] our computations provide the mean absolute error of only 1.1 MHz ($\approx 2\%$ of the range of magnitudes) which justifies our use of calculated HFCCs as a reference.

The HFIs in planar graphenic nanostructures were considered for a set of 12 small planar hydrogen terminated nanographites (Fig. 6.5a) in their triplet spin states. This provides overall statistics for 103 inequivalent ^{13}C HFCCs. The calculated A_{iso} and A_{dip} values are fitted to the extended form of the Karplus-Fraenkel expression

$$A = a_j(1 + \sum_{i \in NN} b_j \Delta r_i) n^c + c \sum_{i \in NN} (1 + d \Delta r_i) n_i^c, \quad (6.3)$$

where the two terms account for the contributions of the on-site and nearest neighbor (NN) conduction electron spin populations, n^c and n_i^c , respectively, calculated from first principles. The on-site coefficients a_j and b_j are distinguished for the cases of C atoms with 3 carbon NNs ($j=3$) and the boundary atoms with 2 carbon NNs ($j=2$). The C–C bond length effects are encountered through the coefficients b_j and d with $\Delta r_i = r_i - r_0$ being the deviation of the bond length r_i from the value for the ideal graphene, $r_0 = 1.42 \text{ \AA}$. The results of the regressions are summarized in Table 6.1 ($1 \text{ MHz} = 4.136 \times 10^{-3} \mu\text{eV}$). Fig. 6.5(b,c) shows the predicted (using expression (6.3) and fitted parameters) values \tilde{A}_{iso} (\tilde{A}_{dip}) versus the calculated A_{iso} (A_{dip}) values. Regressions to the linear expression (6.3) provide accurate estimations (root-mean-square-errors are 1.2 MHz and 1.8 MHz for A_{iso} and A_{dip} , respectively). The calculated isotropic HFCCs span about the same range of magnitudes ($-16.3 \text{ MHz} < A_{iso} < 23.1 \text{ MHz}$) as the dipolar HFCCs ($-5.3 \text{ MHz} < A_{dip} < 24.1 \text{ MHz}$). The HFCCs of boundary atoms tend to be larger due to the fact that low-energy states localize at the zigzag graphene edges [256]. The on-site and the NN spin-polarization effects have competitive character ($a_3/c \approx -2.5$) in the case

of isotropic HFCCs. Our calculations predict $\approx 50\%$ larger values for the parameters a_2 , a_3 and c for A_{iso} compared to those obtained by Karplus and Fraenkel in their early studies of HFCCs in molecular radicals ($a_2=99.8$ MHz, $a_3=85.5$ MHz and $c=-39$ MHz) [250]. This difference can be explained by the explicit incorporation of the electron correlation effects in our calculations and to the characteristic local atomic structure of the graphene lattice. Both A_{iso} and A_{dip} show a tendency to enhance the on-site and to weaken the NN contributions with the increase of C–C bond lengths. The dipolar HFCC is mostly influenced by the on-site contribution of the half-populated conduction state and the NN spin-polarization effect is weaker in this case ($a_3/c \approx -7$). When compared to typical solid state environments based on heavier elements, the ^{13}C HFCCs in graphene and related nanostructures are weaker (e.g. 117 MHz ^{31}P Fermi contact HFCC for the P shallow donor in Si [257]) and more anisotropic.

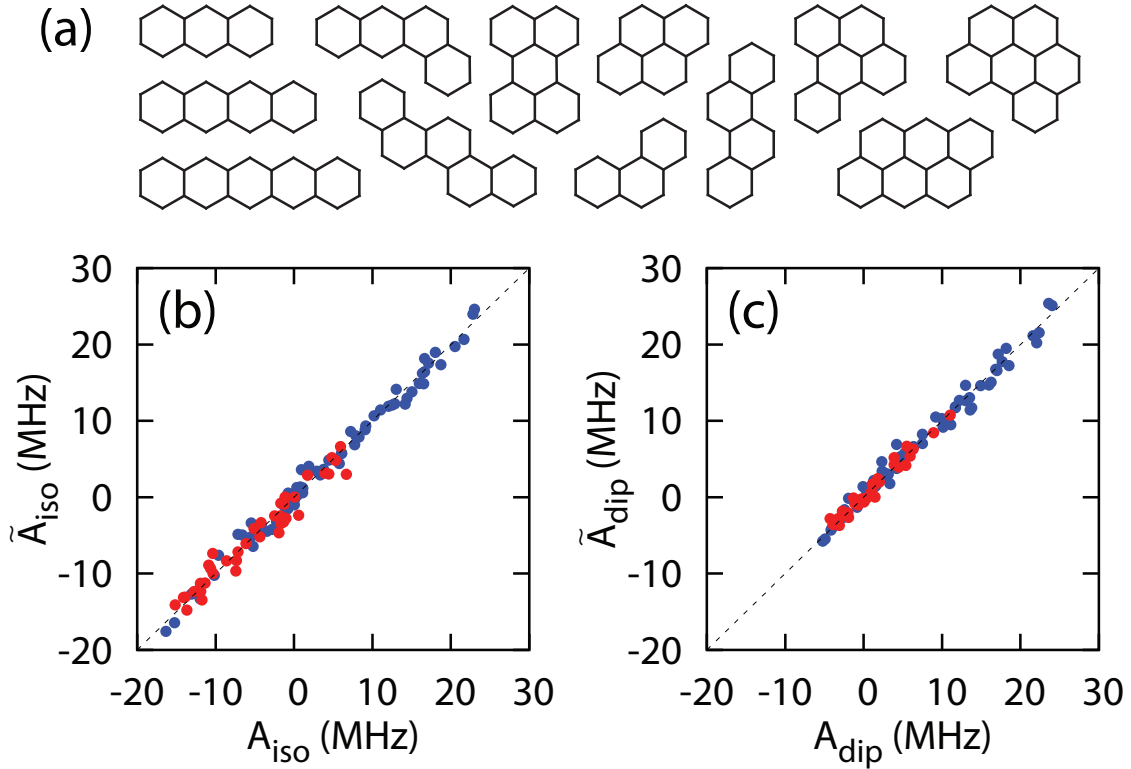


Figure 6.5: (a) Set of graphene fragments used in the present calculations. Fitted Fermi contact (\tilde{A}_{iso}) and dipolar (\tilde{A}_{dip}) ^{13}C HFCCs vs the corresponding values, A_{iso} (b) and A_{dip} (c), calculated from first principles. The values for inner (3 carbon NNs) and boundary (2 carbon NNs) atoms are shown as red and blue dots, respectively.

Table 6.1: Parameters (in MHz) fitted to the results of calculations of a set of nanographite molecules.

	This work		Ref. [250]	
	A_{iso}	A_{dip}	A_{iso}	A_{dip}
a_2	151	144	99.8	
a_3	135	116	85.5	
b_2	1.7	2.9		
b_3	4.9	5.2		
c	-57.6	-17.3	-39	
d	-5.5	-13.9		

The graphene honeycomb lattice is a bipartite lattice, i.e. it can be partitioned into two complementary sublattices A and B . We discuss the HFIs for the three general cases of conduction electron spin distributions over the sublattices: (i) ferromagnetic $n_A^c = n_B^c > 0$; (ii) ferrimagnetic $n_A^c > 0$ and $n_B^c = 0$ and (iii) antiferromagnetic $n_A^c = -n_B^c > 0$ (see Table 6.2). The first case can be physically realized upon the uniform magnetization of the system with equivalent A and B sublattices, e.g. by applying an external magnetic field. The negative $A_{iso} = -35.8$ MHz is small due to the partial compensation of the on-site and the NN spin-polarization effects. This value is consistent with the values derived from the experimental ^{13}C Knight shifts in graphite intercalates ($-25 \text{ MHz} < A_{iso} < -50 \text{ MHz}$) [226] and with the calculated isotropic Knight shifts in metallic carbon nanotubes [104]. The ferrimagnetic case with the conduction state distributed over the atoms of only one sublattice (A) is physically realized at the zigzag edges [256] and around single-atom point defects in sublattice B [258]. Considerable alternating Fermi contact and dipolar HFCCs are predicted in this case. An antiferromagnetic pattern can be realized in the case of heavily disordered systems with localized defect and edges states in both sublattices [259]. The magnitudes of HFIs are minimized and maximized in the cases of ferromagnetic and antiferromagnetic electron spin distributions, respectively.

Many carbon nanostructures of reduced dimensionality (e.g. nanotubes and fullerenes) represent non-planar topologies. Local curvatures lead to the $sp^2 - sp^3$ rehybridization of carbon atoms and enable a Fermi contact interaction involving the electron spins of π states [202]. This results in a positive contribution of the π states unless n^c is close

Table 6.2: Hyperfine coupling parameters for three general cases of spin populations n_c of the carbon atoms of A and B sublattices of graphenic systems.

	$A_{iso}(A)/n^c$	$A_{iso}(B)/n^c$	$A_{dip}(A)/n^c$	$A_{dip}(B)/n^c$
$n_A^c=n_B^c>0$	-38	-38	65	65
$n_A^c>0; n_B^c=0$	135	-173	116	-52
$n_A^c=-n_B^c>0$	308	-308	168	-168

to zero: a contribution due to the NN spin-polarization effect is negative in this case. The degree of rehybridization m of the π states ($s^m p$) can be described using a local bond angles analysis [247]. For the case of large curvature radii the original expression for m can be reformulated in a more convenient form, $m=d_{cc}^2/8(1/R_1+1/R_2)^2$, where d_{cc} is the C–C distance, R_1 and R_2 are the principal curvature radii. The curvature-induced contribution to the Fermi contact ^{13}C HFCC is then $A_{iso}^{curv}=\frac{8\pi}{3}\gamma_e\gamma_I\hbar^2nm\phi_{2s}^2(0)$, where $\phi_{2s}(0)$ is the magnitude of the carbon atomic $2s$ wavefunction at the point of nucleus. For a 1.4 nm diameter carbon nanotube $A_{iso}^{curv}/n^c\approx 8.7$ MHz, a value that is smaller than the spin-polarization contributions for all scenarios given in Table 6.2. However, the curvature-induced direct coupling grows as R^{-2} with decreasing R and becomes significant, e.g. in the case of ultranarrow ($d<1$ nm) carbon nanotubes [238].

Table 6.3: Parameters (in MHz) describing the HFIs of nuclei of substitutional impurities (^{11}B and ^{14}N), monoatomic functional groups (^1H and ^{19}F) and rehybridized carbon atoms (^{13}C) at the edges.

Nucleus	Position	A_{iso}		A_{dip}	
		a	c	a	c
^{11}B	subst. impurity	43	-31	60	5
^{14}N	subst. impurity	150	-22	130	-10
^1H	C_{sp^2} edge	-118	20		
^{19}F	C_{sp^2} edge	240	-40		
^1H	C_{sp^3} edge		350		
^{19}F	C_{sp^3} edge		750		
^{13}C	C_{sp^3} edge		-68		

Since the natural abundance of the “HFI-active” ^{13}C isotope is small ($\approx 1\%$), consideration of the nuclei of other elements is important for a complete description of HFIs in carbon nanostructures. The common substitution impurities are boron and nitrogen with all natural isotopes having nuclear spins. Graphene edges can be terminated by hydrogen and fluorine atoms with both ^1H and ^{19}F spin-1/2 nuclei (99.9885% and 100% natural abundance, respectively) having high gyromagnetic ratios ($\gamma(^1\text{H})/\gamma(^{13}\text{C})\approx\gamma(^{19}\text{F})/\gamma(^{13}\text{C})\approx 4$). We consider HFIs in a reduced set of molecular fragments (only 3- and 4-ring structures included) with impurities and edge functionalizations in all possible positions. The calculated HFCCs have been fitted to the Karplus-Fraenkel relation, with no Δr terms included (Table 6.3). Both Fermi contact and dipolar HFCCs of the impurity nuclear spins show a monotonic increase along the ^{11}B – ^{13}C – ^{14}N series when compared to the results for ^{13}C HFCCs (Table 6.1). The NN relative spin-polarization effects (a/c ratio) on the Fermi contacts HFCCs tend to decrease along the series. While the HFIs of the nuclear spins in substitution impurities are highly anisotropic, the hyperfine couplings of the edge nuclei show small anisotropy due to the sp^3 character of bonding. When ^1H and ^{19}F edge nuclei are bound to the C_{sp^2} atoms, the isotropic HFCCs are of the same order of magnitude as those of the ^{13}C spins in the graphene lattice. The influence of the NN carbon atoms (second NNs to the terminating atom) is very similar for ^1H and ^{19}F nuclei and smaller than in the case of ^{13}C HFCCs ($a_H/c_H\approx a_F/c_F\approx -6$). The spin polarization effect on ^{19}F HFCCs is stronger and of opposite sign compared to that of protons ($a_F/a_H\approx c_F/c_H\approx -2$). When edge atoms are bound to the rehybridized (sp^3) carbon atoms, n^c is zero but the NN contribution is significantly enhanced. The NN contribution to the ^{13}C hyperfine coupling of the sp^3 edge carbon atom itself ($c=-68$ MHz) has a similar magnitude as that of the sp^2 edge atoms ($c=-57$ MHz). HFIs with the boundary spins (H-terminated edges are often obtained in experiments [260]) have to be taken into account when designing carbon-based nanoscale devices for spintronics or quantum computing. A chemical modification of the graphene edges (e.g. substitution of the hydrogen atoms by alkyl-groups) can be suggested to reduce unwanted effects from the HFIs with boundary spins.

To conclude, the results of first principles calculations show that the hyperfine interactions in graphene and related nanostructures are defined by the local distribution of the conduction electron spins and by the local atomic structure. A complete set of parameters describing the hyperfine interactions with the extended Karplus-Fraenkel expression was determined for the ^{13}C and other common nuclear spins. These results will permit

control of the magnetic interactions between the spins of electrons and nuclei by tailoring the chemical and isotopic compositions, local atomic structures, and strain fields in sp^2 carbon nanostructures. Some practical recipes for minimizing interactions with nuclear spins are given.

Chapter 7

Point defects in carbon nanostructures

7.1 Introduction

In the previous Chapter, we discussed the subject of magnetic interactions in carbon nanostructures in the light of their possible applications. At this stage, it is fairly difficult to avoid the question of a possibility of long-ranged magnetic order in such systems. In fact, magnetic correlations in carbon materials have been reported recently by several experimental groups [261] for different graphenic systems. Although in most of these observations the origin of magnetic ordering still remains obscure and even some experiments are questioned, the topic of carbon magnetism has attracted enormous attention. Since in current technological applications magnetic materials are based exclusively on *d* and *f* elements, new carbon-based magnetic materials would greatly extend the limits of technologies relying on magnetism. These materials may have low density, unusual properties (e. g. plasticity or transparency) and, eventually, can be made environment friendly. Even more promising is the application of such materials in the design of nanoscale magnetic and spin electronics devices.

While ideal graphite and carbon nanotubes are in itself nonmagnetic, experimental observations of magnetic ordering are often explained by the presence of impurities [262], boundaries [263, 264] or defects [265, 266]. Defects in nanographites [267] can be created intentionally by irradiating material with electrons or ions [39, 41, 42, 268]. By manipulating the conditions of irradiation it is possible to tune, in a flexible way, the properties of the carbon-based materials [40, 43, 269, 270]. In the first part of this Chap-

ter, we investigate the defect-induced itinerant magnetism in graphene. Afterwards, we study the mechanisms of radiation-induced defect formation in carbon nanostructures. Understanding these mechanisms is also important in some other contexts. Radiation resistance of graphite has been one of the major concerns of nuclear industry [271, 272]. Nowadays, radiation treatment by high-energy electrons or ions is also viewed as a versatile tool for the design of new materials. The formation of irradiation-induced defects in graphite-like layered carbon nanostructures (multiwalled and bundled carbon nanotubes, nanooxions, etc.) changes their mechanical [43] and electronic properties [40, 270] and may even trigger dramatic structural changes [273, 274]. However, the structure and dynamics of defects in graphite and carbon nanostructures as well as the mechanisms underlying their creation and transformation remain elusive. This knowledge is crucial for a defect-assisted engineering of nanostructures with applications in, e. g., manufacturing of nanoelectromechanical systems [275–278].

7.2 Magnetism induced by single atom defects

Defects in carbon nanostructures exhibit spectacular diversity. In this study we concentrate on simple prototypical defect structures. Examples of simple defects in nanographites are single atom vacancies and hydrogen chemisorption defects. The former defect type is produced upon irradiation with high energy particles [266] while the latter is the major outcome of the hydrogen plasma treatment [268]. The common feature of both types of defects is that only one carbon atom is removed from the π conjugation network of the graphene sheet. The single-atom defects on the graphene lattice give rise to quasilocalized states at the Fermi level [268, 279–281]. When a defect is created in one sublattice of the graphene bipartite lattice, only the p_z orbitals of carbon atoms in the complementary sublattice contribute to the quasilocalized state. These states extend over several nanometers around the defects forming characteristic $(\sqrt{3} \times \sqrt{3})R30^\circ$ superstructures recognized in STM images. Analyzing the position and the orientation of the superstructures one can precisely locate the defect and determine the sublattice to which it belongs [258, 279]. The fact that quasilocalized states lie at the Fermi level suggests that magnetism can be induced by the electron exchange instability. It has been argued recently, that the Stoner ferromagnetism with high Curie temperatures T_c can be expected for sp electron systems [282]. On the other hand, the Ruderman-Kittel-Kasuya-Yoshida (RKKY) coupling [283–285] of localized magnetic moments in graphene is too

weak to result in high T_c [286].

By using first principles approaches we investigate magnetism originating from the quasilocalized states induced by single-atom point defects in graphene. The results obtained can eventually be extended, with some precautions, to defects in other nanographites. The model system consists of a periodic two-dimensional superlattice of defects in graphene (Fig. 7.1a). The supercell size can be varied resulting in different distances d between the neighbor defects on the superlattice and, thus, in different defect concentrations. The results can be further extrapolated to the cases of low defect concentrations. For the chosen supercell, the resulting distance between neighbor defects is about $3na_{cc}$ where $a_{cc}=1.42 \text{ \AA}$ is the carbon-carbon distance in graphene. The corresponding number of carbon atoms per unit cell is $6n^2$. Our investigation is restricted to the cases with $n=2-6$. The largest system considered ($n=6$) is characterized by about 25 \AA separation between neighbor defects, which corresponds to a defect concentration of 0.5%.

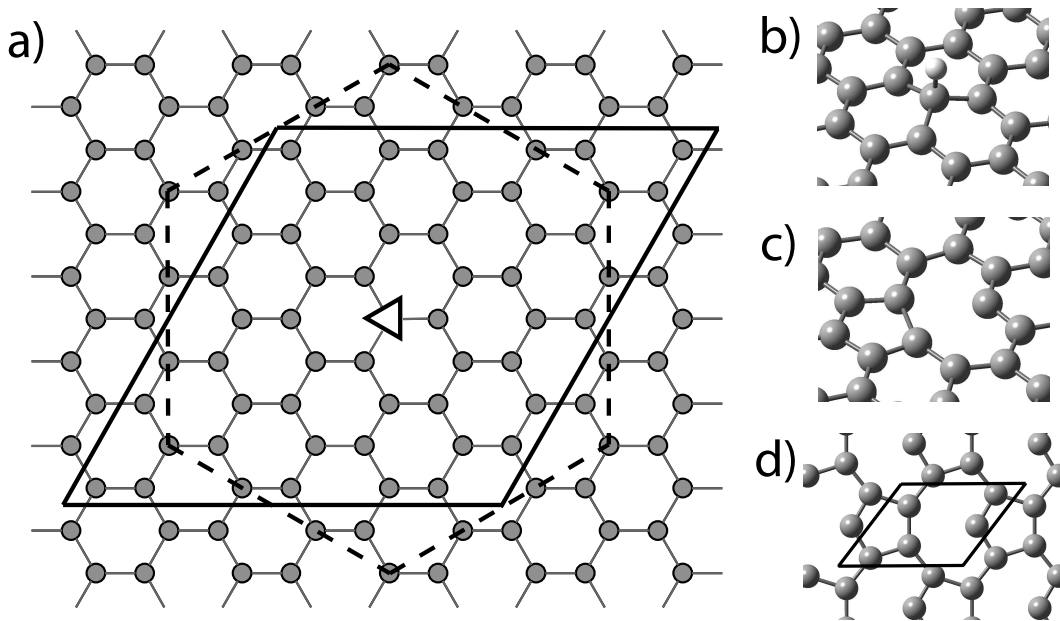


Figure 7.1: (a) Definition of the extendable two-dimensional hexagonal lattice of defects in the graphene sheet. The unit cell and the Wigner-Seitz cell are shown as full and dashed lines, respectively. The defective atom is labeled by the triangle according to the orientation of the defect state $\sqrt{3} \times \sqrt{3}$ superstructure. The size of the supercell shown here corresponds to $9a_{cc}$ separation between neighbor defects ($n=3$). (b) Structure of the hydrogen chemisorption defect. (c) Structure of the vacancy defect. (d) Hexagonal closest packing ($n=1$) of vacancy defects with the corresponding unit cell.

Density functional theory calculations were performed using the **SIESTA** code [287]. The generalized gradient approximation exchange-correlation density functional of Perdew, Burke and Ernzerhof (PBE) [153] was employed. All calculations were performed in the spin-unrestricted manner using the diagonalization-based method for solving Kohn-Sham equations. The shifted Monkhorst-Pack grids [288] corresponding to a cutoff of 100 Bohr were used to sample the Brillouin zone in two dimensions. Atomic positions and cell dimensions were relaxed. The numerical atomic orbital basis set of single- ζ plus one polarization function (SZP) quality was used for the whole range of models studied. All calculations for the models with $n=2-4$ were reproduced using the basis set of double- ζ plus one polarization function (DZP) quality. For all electronic structure quantities discussed in this study (magnetic moment, Fermi levels and band maxima), there is a good agreement between the results of the two basis sets, despite the slight overestimation of the C–C bond length found in the SZP calculations.

In the following we present our results for the two types of defects. The structure of the hydrogen chemisorption defect is shown in Fig. 7.1b. This defect is characterized by the slight protrusion of the hydrogenated carbon atom and the very small displacement of all other neighbor carbon atoms [289, 290]. The single atom vacancy defect in graphene is nearly planar (Fig. 7.1c). The local three-fold symmetry breaks down due to the Jahn-Teller distortion induced by the reconstruction of two dangling bonds left after removing the carbon atom. This gives rise to the in-plane displacement of other carbon atoms in the graphene lattice [266, 291]. The third dangling bond is left unsaturated providing a contribution of magnitude $1 \mu_B$ to the intrinsic magnetic moment of the defect. For the case of the vacancy type defect (Fig. 7.1d) in the closest packing geometry ($n=1$) no single six-membered ring remains. This interesting structure can be considered as yet another hypothetical allotropic modification of carbon for which one may expect a high specific magnetic moment.

Magnetism induced by the presence of quasilocalized defect states $\psi_d(\mathbf{r})$ has been observed in the case of both defect types. The hydrogen chemisorption defect gives rise to the strong Stoner ferromagnetism [292] with a magnetic moment of $1 \mu_B$ per defect at all studied concentrations (Fig. 7.2a). The flat defect bands give rise to the very narrow peaks ($W < 0.2$ eV) at the Fermi level (Fig. 7.3a) which are necessary for the stability of magnetic ordering at high temperatures [282]. The defect band maxima for the majority spin and the minority spin components lie, respectively, lower and higher than the Fermi levels for both defective and ideal graphene. This leads to the conclusion that

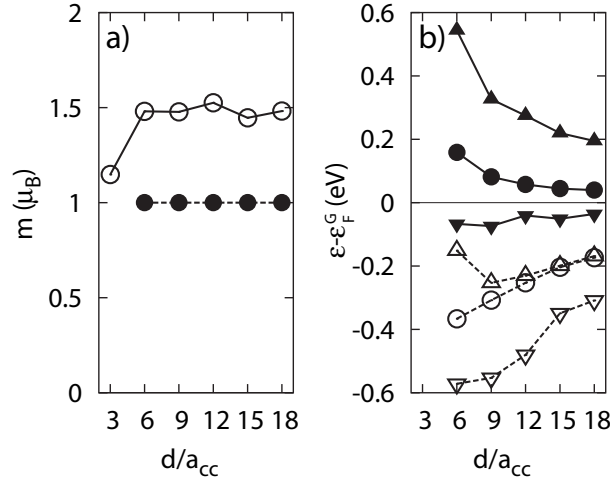


Figure 7.2: (a) Calculated magnetic moment per defect vs. the separation d between the neighbor hydrogen chemisorption defects (\bullet) and the neighbor vacancy defects (\circ). (b) Fermi energies (\bullet, \circ), majority spin ($\blacktriangle, \triangle$) and minority spin ($\blacktriangledown, \triangledown$) bands maxima versus the defect separation d for the hydrogen chemisorption defects (filled symbols) and the vacancy defects (open symbols).

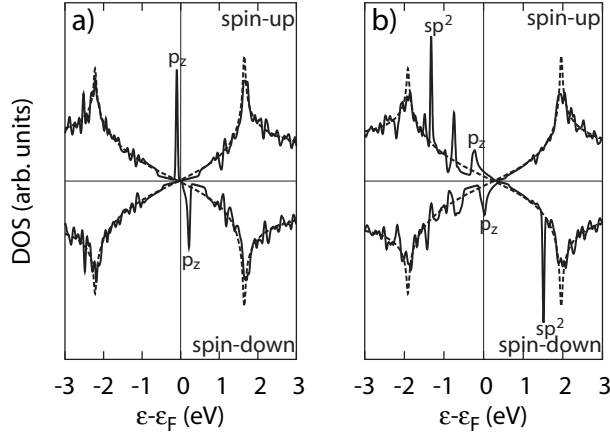


Figure 7.3: Density of states plots for the systems with the hydrogen chemisorption defects (a) and with the vacancy defects (b) ($n = 4$). The dashed line shows the density of states of the ideal graphene. Labels indicate the character of the defect states.

the hydrogen chemisorption motif is charge neutral and spin-polarized in the wide range of defect concentrations. On contrary, fractional magnetic moments and weak Stoner ferromagnetism [292] have been observed for the vacancy-type defect models. A magnetic moment of $1.15 \mu_B$ has been predicted for the closest packing of vacancy type defects ($n=1$) (Fig. 7.1d), while for smaller defect concentrations the magnetic moment was found to vary in the range of $1.45\text{--}1.53 \mu_B$ per defect (Fig. 7.2a). For the vacancy-type defect, the total magnetic moment is determined by the contribution ($1 \mu_B$) of the localized sp^2 dangling bond state (atom 1 in Fig. 7.4b) and the contribution ($<1 \mu_B$) of the extended defect state, $\psi_d(\mathbf{r})$ (labeled p_z in Fig. 7.3). The width of the defect state bands and the overall modification of the band structure are larger in the case of the vacancy type defects (Fig. 7.3b). The partial spin polarization of $\psi_d(\mathbf{r})$ (filled majority spin band and half-filled minority spin band) is explained by the self-doping (charge transfer from the bulk to $\psi_d(\mathbf{r})$), which arise from the stabilization of the defect state.

The stabilization of vacancy defect extended states is possible in the case of a significant coupling between the second nearest neighbor atoms belonging to the same sublattice [281]. In the case of the vacancy defect, the indirect coupling is justified by the formation of the covalent bond between the two carbon atoms 1' (Fig. 7.4b) that follows the defect reconstruction. No such bond is possible in the case of hydrogen chemisorption. Thus, the character of the defect-induced magnetism depends on the possibility of bonding between the second nearest neighbor atoms due to the reconstruction. This provides an interesting opportunity for tailoring magnetic properties of materials. The defect state exchange splitting $d\epsilon_x$, defined as the difference between the corresponding majority spin and minority spin band maxima, decreases as the defect concentration decreases. This is not surprising since the degree of the localization of the defect states depends on the defect concentration [281]. At the lowest studied defect concentration of 0.5%, the exchange splittings were found to be 0.23 eV and 0.14 eV for the hydrogen chemisorption and vacancy defects, respectively. In the latter case, the splitting is smaller due to the partial spin polarization of the defect band. Since in both cases $d\epsilon_x > k_B T$ for $T \approx 300$ K, the Stoner theory predicts T_c above room temperature for defect concentrations of the order of 1%. The decrease of the Stoner theory T_c due to spin wave excitations is expected to be ineffective for the case of carbon based materials [282]. At low concentrations the magnetism in defective nanographites is expected to be sensitive to the variations of the Fermi energy resulting from self-doping, presence of other defects or applied bias, and to the disorder-induced broadening.

The distributions of the electron spin magnetization density in the vicinity of both types of defects clearly show the characteristic $\sqrt{3} \times \sqrt{3}$ patterns also observed for the charge density in the STM experiments. For the hydrogen chemisorption defect the projection of the spin density (Fig. 7.4a) on the graphene plane clearly shows three-fold symmetry. For the vacancy type defect the symmetry is broken due to the Jahn-Teller distortion (Fig. 7.4b). The localized magnetic moment associated to the dangling bond of atom 1 can also be observed. The simulated STM images (Fig. 7.4c and 7.4d) based on our calculations agree with experimental observations [268, 279, 280]. The distribution of the electron spin density is represented in Fig. 7.5 ($n=6$ model) by means of the Mulliken spin populations averaged over i th nearest neighbors to the defect atom. The spin populations show a damped oscillation behavior as a function of the nearest neighbor index and, therefore, of the distance to the defect. The magnetization pattern is explained by the fact that the defect state is distributed over the sites of the sublattice complementary

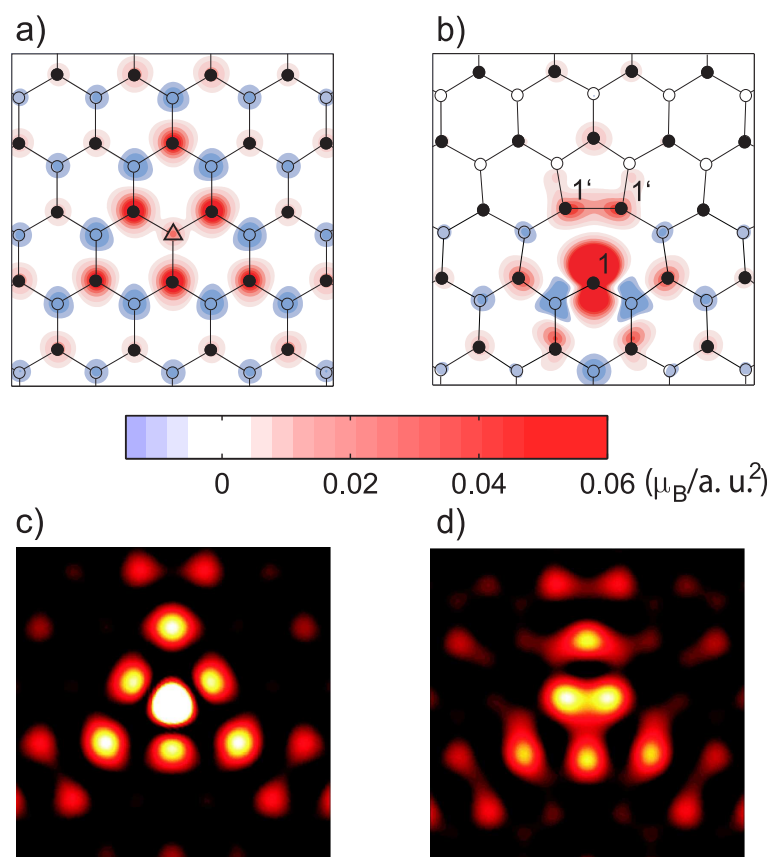


Figure 7.4: Spin density projection (in $\mu_B/a.u.^2$) on the graphene plane around (a) the hydrogen chemisorption defect (Δ) and (b) the vacancy defect in the α sublattice. Carbon atoms corresponding to the α sublattice (\circ) and to the β sublattice (\bullet) are distinguished. Simulated STM images of the defects are shown in (c) and (d).

to the one in which the defect was created (i. e. over the odd nearest neighbors), and shows a power law decay [281]. The major positive contribution to the electron spin density is defined by the exchange splitting of the defect states. In addition, the exchange spin-polarization effect (i.e. the response of the fully populated valence bands to the magnetization of the defect states) results in a negative spin density on the even nearest neighbor sites (blue in Fig. 7.4) and in the enhancement of a positive spin density on the odd nearest neighbor sites (red in Fig. 7.4). A similar phenomenon takes place in the case of the neutral bond length alternation defect states in one-dimensional polyene chains [293, 294]. The calculated magnitude of the negative spin-polarization is $\approx 1/3$ of the positive spin populations on the neighbor sites in the vicinity of the defect site. This is close to the ratio observed for the *trans*-polyacetylene [293]. The magnitudes of the

spin populations are lower in the case of the vacancy defect because of the fractional spin-polarization of the defect band.

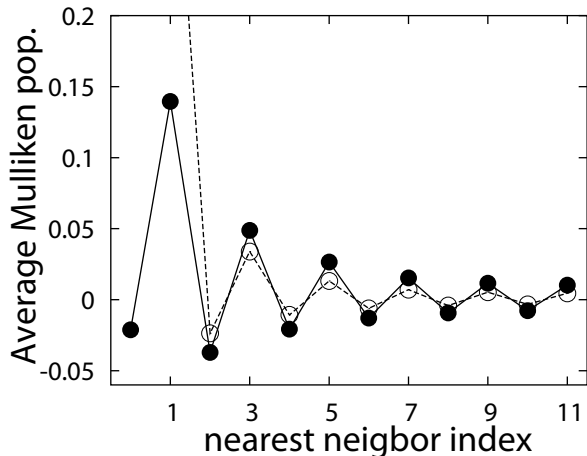


Figure 7.5: Dependence of the spin populations averaged over i th nearest neighbors of the hydrogen chemisorption defects (●) and the vacancy defects (○). The spin population for the first nearest neighbor atoms of the vacancy defect (0.39) are out of scale due to the contribution of the localized sp^2 dangling bond state.

According to the Stoner picture, the magnetic ordering is driven by the exchange energy $E_x \sim -\sum_i M_j^2$ with M_j being the magnetization of the p_z orbital of the j th carbon atom [292]. Ferromagnetic ordering is the only possibility for the magnetism originating from quasilocated states induced by defects in the same sublattice because of the non-oscillating behavior of both (i) M_j within the same sublattice and (ii) the indirect (RKKY) coupling due to the semimetallic properties of graphene [286]. On the contrary, for the case of defect states in different sublattices, E_x is minimized when the coupling is antiferromagnetic. In this case, the mechanism of the exchange coupling is defined by the indirect spin-polarization effect. The strength of the coupling between the defect-induced magnetic moments located in different sublattices depends on the defect concentration since $E_x \sim -\sum_i M_j^2$. The contribution of the magnetic moment associated with a single defect is $\sum_i M_j^2 \sim \sum_j |\psi_d(\mathbf{r}_j)|^4 \sim \log^{-2}(N)$, where $1/N$ is the defect concentration [281]. To further illustrate this point, we calculated the ground state magnetic configuration of the system with three close hydrogen chemisorption defects using the DFT approach. We found that in the ground state configuration two defects in the α sublattice are coupled ferromagnetically with each other and antiferromagnetically with the third defect in the β sublattice (Fig. 7.6). The resulting magnetic moment of this system amounts to $1 \mu_B$, and the characteristic $\sqrt{3} \times \sqrt{3}$ superstructure patterns of the magnetization density associated with individual defects can be recognized. In nanographite materials with defects present with an equal probability in both sublattices, the overall correlation of the magnetic moments is expected to be antiferromagnetic. The

antiferromagnetic ordering was experimentally observed in carbon nanohorns [295, 296].

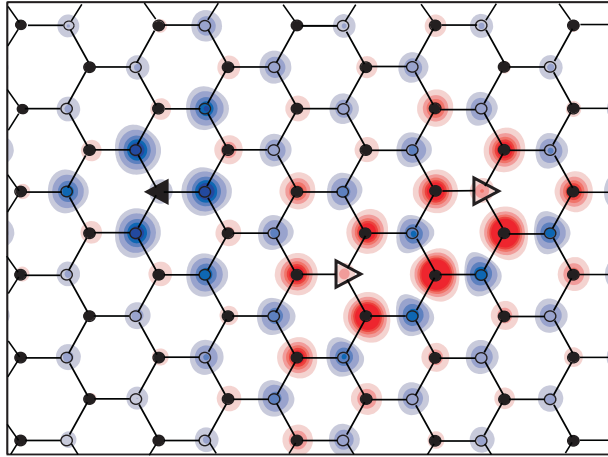


Figure 7.6: Spin density distribution in the system with three hydrogen chemisorption defects (two defects in sublattice α (\triangleright) and one in sublattice β (\blacktriangleleft)).

In conclusion, our calculations reveal the itinerant magnetism triggered by simple defects in graphene and stable over the wide range of concentrations. It is notable, that the itinerant magnetism does not require the presence of highly reactive unsaturated dangling bonds. Both ferromagnetic and antiferromagnetic scenarios of the magnetic correlation are possible with the second being more probable for truly disordered systems. The reconstruction of vacancy defects was found to be responsible for the partial suppression of magnetic moments and for the broadening of defect bands.

7.3 Radiation-induced defect formation

Radiation damage of matter is governed by the displacement of atoms from their equilibrium positions due to electronic excitations and direct collisions of high-energy particles with the nuclei. In metals and narrow band gap semiconductors electronic excitations quench instantaneously, leaving collisions with nuclei as the sole mechanism responsible for the creation of defects in graphite and related carbon materials [269]. If the kinetic energy transferred from a high-energy electron or ion to the nucleus is higher than the displacement threshold T_d , a carbon atom can leave its initial position to form a metastable defect structure on a sub-picosecond time scale. Such events are called knock-on displacements. For highly anisotropic layered carbon materials the threshold of the off-plane displacement is $T_d^\perp \approx 15\text{-}20$ eV [273], while a creation of defect due to the in-plane knock-on collision requires higher transferred energies, $T_d^\parallel \geq 30$ eV. Possible defects produced by radiation damage include separated and intimate pairs [297] of interstitial

atoms and vacancies, and in-plane topological defects involving non-sixmembered rings, e.g., Stone-Wales defect [298, 299]. The existence of defects in carbon nanostructures has been confirmed by direct observations [41, 42].

Upon knock-on events a large amount of energy is transferred to only a few degrees of freedom. The resulting defect structures formed on a picosecond time scale depend on the magnitude and on the direction of the transferred momentum and determine the fate of the system at longer time scales. Therefore gaining control over the early stages of defect formation by tuning the irradiation conditions will make the paradigm of the defect-assisted engineering feasible. Molecular dynamics (MD) simulations performed with empirical potentials [300] or tight-binding models [301–303] have been used for the studies of radiation damage of various carbon materials. Below, we report a *systematic first principles* study of the early stages of radiation damage of graphite, a general model for closely related layered carbon nanostructures.

7.3.1 Simulations

By using *ab initio* molecular dynamics we simulate the process of defect formation after the initial transfer of a momentum \mathbf{T} to one of the carbon atoms in the system. The periodic model system consists of a unit cell with 108 carbon atoms, which contains two graphene sheets with stacking ABAB. The dimension of the unit cell in the direction perpendicular to the graphene planes was fixed to 6.7 Å in accordance with the experimental interlayer distance 3.35 Å [304]. The in-plane distance between two periodic images is 12.7 Å which is large enough to ensure localization of the defect within the unit cell. A coarse sampling of the irreducible wedge of the space spanned by the magnitude of transferred energy T and the pair of angles $\phi \in [0^\circ; 90^\circ]$ and $\theta \in [0^\circ; 60^\circ]$ (Fig. 7.7, inset) has been performed. The *ab initio* MD simulations were carried out using the CPMD [132] plane wave density functional theory (DFT) code and the Perdew, Burke, and Ernzerhof exchange-correlation density functional [153]. A plane wave kinetic energy cutoff of 60 Ry and norm-conserving pseudopotentials [151] have been used. The simulations were performed within the spin-unrestricted formulation of DFT starting from an initial guess asymmetric with respect to the spin components. Such a starting configuration is required in order to ensure a broken-symmetry path of bond breaking events [305]. The first 100 fs of each MD simulation were performed using the Born-Oppenheimer scheme. The initial simulation was followed by a Car-Parrinello simulation [131] with

Nosé-Hoover thermostat [306] (350 K) until a stable defect structure was reached which typically required less than 1 ps. Finally, the obtained defect structures were relaxed by slow annealing of both ionic and electronic degrees of freedom. The formation energies were evaluated using the SIESTA code [287] by relaxing the ionic coordinates and the in-plane cell dimensions. The same norm-conserving pseudopotentials and density functional as in the plane wave calculations together with an optimized DZP basis set were used. A $2 \times 2 \times 2$ k -point grid was employed in order to obtain accurate defect formation energies [307].

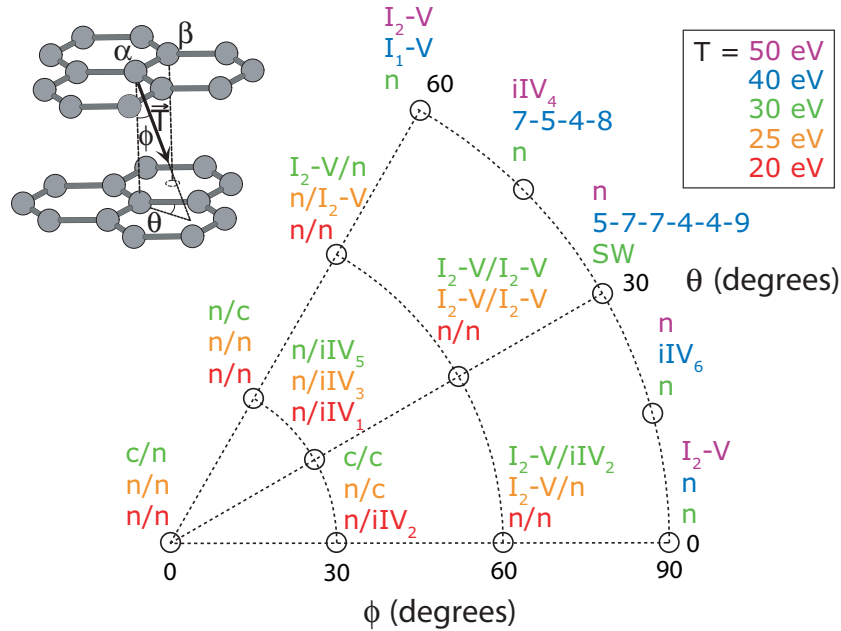


Figure 7.7: Polar coordinates representation of the simulation outcomes as a function of T , ϕ , and θ . The labels indicate formation of defect structures (Fig. 7.8 and 7.9). Other labels correspond to: “n” - no defect formation, and “c” - displacement cascade. The outcomes for α/β carbon atoms are distinguished for off-plane displacements. Color codes correspond to the magnitudes of transferred kinetic energy. The convention for the direction of knock-on displacement is shown on the inset.

7.3.2 Off-plane recoils

The outcomes of our simulations are summarized in Figure 7.7. We first discuss the simulation results for the off-plane displacements ($\phi \in \{0^\circ; 30^\circ; 60^\circ\}$) of carbon atoms in inequivalent positions α and β . The outcomes can be divided into four major classes: (i)

no defect formation due to insufficient transferred momentum or due to instantaneous recombination of the recoil atom with the vacancy (“n”); (ii) separated interstitial-vacancy pairs (I-V); (iii) intimate interstitial-vacancy pairs (iIV); (iv) displacement cascades (“c”) in which the recoil atom is able to displace other atoms in the lattice. The later case can be viewed as a series of elementary events of types (i)–(iii). The simulation of displacement cascades is beyond the scope of this study and would require a larger unit cell than the one used here.

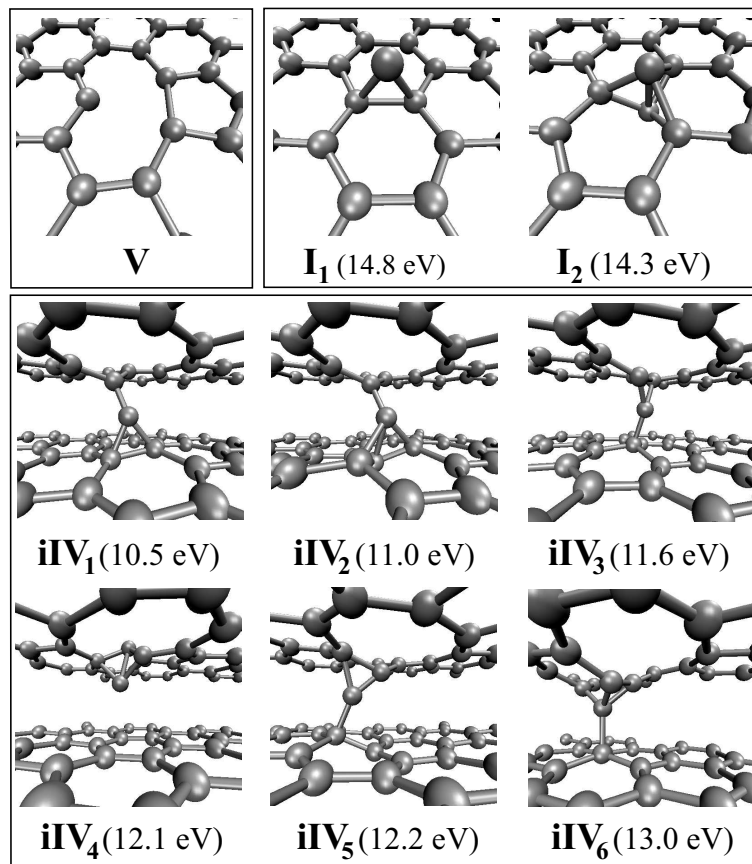


Figure 7.8: Perspective views of the atomic structures of the vacancy (top, left), interstitial (top, right), and intimate Frenkel pair (bottom) defects observed in our simulations. The formation energies are given in parentheses. The values given for interstitial defects refer to the formation energies of corresponding Frenkel pairs. For iIV defects the created vacancy is situated in the upper graphene layer.

The formation of well-separated Frenkel pairs was observed for atoms in both α and β positions at $T \geq 25$ eV. Surprisingly, the interstitial defects were produced only

in the form of a symmetric “dumbbell” structure (I_2) [308,309] where the two carbon atoms are symmetrically displaced from the graphene plane (Fig. 7.8, top). Despite the highly distorted coordination sphere of these atoms, the C-C distance of 1.58 Å is close to the one of a typical σ bond. The core atomic structure is the same as for the [1.1.1]propellane molecule for which a very similar C-C bond length (1.60 ± 0.02 Å) has been observed experimentally [310]. No single off-plane recoil led to the “bridge” structure (I_1) [300,308,311] with the interstitial atom situated between two graphene planes. The formation energy of I_2 ($E_f=14.3$ eV, the value refers to the formation energy of the corresponding I-V pair) is only 0.5 eV lower than the one of I_1 ($E_f=14.8$ eV) where the “bridge” interstitial defect is bonded only to the neighbor atom in the same layer. In this case, a steric repulsion with the opposite graphene layer contributes to the destabilization of the I_1 defect. However, bonding to the opposite layer leads to more stable shared interstitial defect structures [272,308]. In the ylid ($E_f=14.1$ eV) and spiro ($E_f=13.1$ eV) configurations, the shared interstitial atom is additionally bound to one and, respectively, to two carbon atoms of the adjacent layer. These structures have not been observed in our MD simulations. The observed preference for the I_2 configuration in graphite may have the following origin. In the “dumbbell” configuration the recoil atom is able to transfer its excess kinetic energy to the other atoms more efficiently than in the case of the “bridge” configuration. At the same time, the formation of shared interstitials requires the improbable collective motion of a number of atoms in the two adjacent graphene layers in the direction of the recoil atom. This explains the observed high probability for the formation of the I_2 defect structure in the early stages of the radiation-induced defect formation. For the isolated graphene sheet, I_1 is 0.2 eV more stable than I_2 due to the absence of the steric repulsion with the adjacent graphene layer. In curved graphenic structures, like carbon nanotubes, the “bridge” interstitial defect undergoes further stabilization. The “dumbbell” interstitial can also be viewed as a stable intermediate of the self-diffusion process in graphite along the c -axis, occurring via the substitution of a carbon atom in the graphene layer [312]. Our first principles calculations predict that the transition from the defect structure I_2 to the structure I_1 in graphite is characterized by an activation barrier of 0.9 eV.

Formation of intimate interstitial-vacancy pairs (iIV) requires lower transferred kinetic energies. At $T=20$ eV we observed the formation of two low energy iIV pairs, iIV_1 ($E_f=10.5$ eV) and iIV_2 ($E_f=11.0$ eV) (Fig. 7.8, bottom). The displaced atom bridges the defect vacancy with two, respectively, three neighbor atoms in the opposite layer,

which undergo rehybridization. A fine scan of the transferred momentum space indicates a T_d value of 18 eV for graphite, in agreement with other reported values [273, 313]. As a consequence, the use of a particle beam energy capable of achieving a maximum kinetic energy transfer just above T_d will *selectively* create iIV defects. This value for T_d would correspond to the maximum kinetic energy transferred by an electron beam of 90 keV [313]. In the case of carbon nanotubes, T_d is expected to be lower due to curvature effects [42]. This proves the crucial role of the iIV defects in the reinforcement of carbon nanotube bundles [43, 314] produced by 80 keV electron irradiation. Our results suggest the optimal conditions for the modification of mechanic and electronic properties of carbon-based layered nanostructures by means of the formation of iIV defects. Such modifications are nondestructive since iIV defects tend to self-recombine without producing extensive damage of the nanostructure [42]. This is also supported by the fact that the barriers for iIV₁ defect recombination [297] and for the transformation of iIV₁ into iIV₂ (0.9 eV in this study) lie below the formation energies of I-V pairs.

Our computed formation energy for the previously proposed iIV₁ structure [297] is in good agreement with the values reported in other studies [297, 308, 314]. However, MD simulations on a longer time scale (1 ps) indicate that the asymmetric iIV₁ defect in graphite is not stable against recombination if shear of graphene layers is allowed. By contrast, the symmetric iIV₂ defect is stable throughout our MD simulations. Two other intimate Frenkel pairs, iIV₃ ($E_f=11.6$ eV) and iIV₅ ($E_f=12.2$ eV) have been obtained upon off-plane recoils caused by larger transferred momenta. In both structures the displaced carbon atom is linked to two carbon atoms in its host layer and one atom in the neighboring layer. It is notable that the formation of iIV defects has been observed *only* upon recoil of the β carbon atom.

7.3.3 In-plane recoils

The formation of defects after displacement in the graphene plane ($\phi=90^\circ$) requires higher transferred energies $T \geq 30$ eV. At $T=30$ eV ($\theta=30^\circ$) we observed the formation of a Stone-Wales (SW) defect [298], which is the lowest energy ($E_f=4.8$ eV) defect in graphite. The mechanism of its formation involves the cyclic permutation of three carbon atoms occurring during the first 100 fs after the knock-on collision (Fig. 7.9, top). A much lower activation barrier of ≈ 10 eV is required when the SW defect is formed upon simultaneous rotation of two neighboring carbon atoms about the axis perpendicular to the graphene

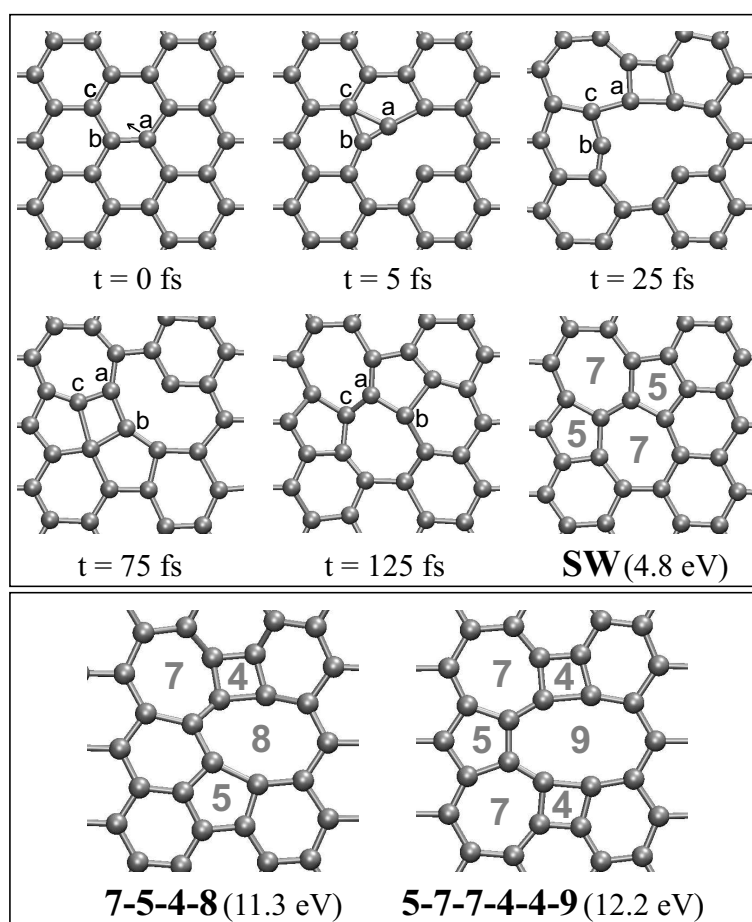


Figure 7.9: Top: The mechanism of formation of a Stone-Wales defect upon in-plane knock-on displacement ($T=30$ eV). The carbon atoms involved in the rearrangement are marked with letters. Bottom: Atomic structures of 7-5-4-8 and 5-7-7-4-4-9 topological defects. Non-sixmembered rings are indicated by arabic numbers.

plane [299]. However, this mechanism *cannot* be realized upon knock-on collisions because in this case the kinetic energy is transferred to a single atom. Irradiation of graphene-based materials, using an electron beam of energy just above 150 keV and oriented along the graphene plane, will result in an *increase* of yield of SW defects. This can be used for tuning electronic properties of materials [315]. However, because of the high energy transfer required for their formation, SW defects will be accompanied by the formation of Frenkel pairs, which form upon low energy ($T < 30$ eV) off-plane recoils.

For $T > 30$ eV two possible general mechanisms of defect formation have been identified. The first one involves the formation of strained structures containing non-sixmembered

red rings, which have formation energies higher than the formation energy of the SW defect. Two such structures, 7-5-4-8 ($E_f=11.3$ eV) and 5-7-7-4-4-9 ($E_f=12.2$ eV) have been observed in our simulations (Fig. 7.9, bottom). The second mechanism involves the expulsion of one carbon atom from the graphene plane shortly after the collision. In this case interstitial-vacancy pairs are formed. We observed formation of the “bridge” interstitial defect I_1 caused by the expulsion of a carbon atom with low kinetic energy. In addition, two new intimate interstitial-vacancy pairs, iIV_4 ($E_f=12.1$ eV) and iIV_6 ($E_f=13.0$ eV) have been characterized. In the iIV_4 structure the defect is localized in the graphene layer where the collision took place. On the contrary, the displaced carbon atom in the iIV_6 structure bridges three atoms of its host layer with one of the neighboring layers. The formation energies of all six iIV structures found in our simulations lie within a narrow interval of 2.5 eV, and they are all below the formation energies of separated I-V pairs.

In conclusion, our *ab initio* molecular dynamics study reveals a variety of different defects, including structures which have never been discussed previously, were observed in our simulations. The produced defects depend strongly upon the direction and magnitude of the transferred momentum, resulting in the selective formation of certain defect structures. We showed the crucial role played by the early stage dynamics, and we identified the conditions at which selective creation of defects can be achieved. The results are of practical importance for radiation-assisted manufacturing of carbon materials and nanostructures with new desired properties and functions.

Chapter 8

Conclusions

8.1 Overview of results

In this work we have studied magnetic properties of paramagnetic aqua ions and carbon nanostructures. Application of paramagnetic complexes as contrast agents for magnetic resonance imaging is a mature branch of the industry of medical diagnostics. Systematic research in the field of MRI contrast media focuses on the development of complexes with higher efficiency (relaxivity) and new functions. The phenomenon of paramagnetic relaxation enhancement is a complicated interplay of interactions involving electron and nuclear spins and molecular dynamics in solution. In our work we assessed some of these interactions parameters and tried to understand their structure-property relations.

In particular, we determined a complete set of coupling parameters between the nuclear spins of an inner coordination sphere water molecule of gadolinium(III) aqua complexes with electron surrounding. The physical interactions behind these parameters are the hyperfine interactions, magnetic interactions between the spins of nuclei and electrons in paramagnetic systems, and the quadrupolar interactions, interactions between nuclear electric quadrupoles (in the case of ^{17}O nucleus) and local electric field gradients. We found that the hyperfine interactions are due to the spin-polarization of water molecules by the localized f -electrons of gadolinium. This spin-polarization enables Fermi contact coupling of proton and ^{17}O nuclear spins to the electron spins of gadolinium. The same physical mechanism is responsible for the deviation of the dipolar (through space) hyperfine interaction from the simple point-dipole model. This deviation can be corrected. We also found that the ^{17}O quadrupolar interactions on the inner coordination sphere water molecule are very similar to those of a water molecule in the hydrogen bond net-

work of neat water. Our finding resolves the long-standing debate about the value of this parameter. The results of our study can be directly applied within the actual model of relaxation of nuclear spins enhanced by the presence of gadolinium(III) complexes.

We also performed first principles molecular dynamics simulations of two paramagnetic metal ions, Cr^{3+} and Gd^{3+} , in aqueous solutions. The main goal of this study was the assessment of the hyperfine interactions in the outer coordination sphere of paramagnetic metal ions. A realistic periodic supercell model was required for reliable simulation conditions. The outer sphere ^{17}O Fermi contact hyperfine couplings are known experimentally for an aqueous solution of the Cr^{3+} ion; the values are about 1/10 of the values for the inner sphere ^{17}O nuclei and have an opposite sign. The results of our calculations are in remarkable agreement with experimental data. This makes us confident in density functional theory as a tool for studying spin-polarization in extended system. In the case of the Gd^{3+} ion, the spin-polarization of the outer-sphere water molecules was found to be smaller in magnitude. We attributed this observation to a lower degree of organization of the second coordination sphere of the gadolinium(III) ion as compared to the chromium(III) ion. In order to enable calculations of hyperfine coupling constants within the first principles molecular dynamics scheme we developed a novel computational technique. It takes into account spin-polarization of core electrons which is missing in pseudopotential electronic structure methods used in the vast majority of first principles molecular dynamics codes. Our benchmark tests showed that the accuracy of our approach is close to the accuracy of all-electron calculations which are typically performed on molecular systems.

The scientific research in the field of carbon nanostructures is more likely a technological revolution rather than a gradual improvement of existing technologies. Recent discoveries of novel carbon nanostructures and their extraordinary properties continuously motivate the scientific community to search for applications in all possible fields of human activity. We were looking for unusual magnetic properties of these materials, in particular, hyperfine interactions. We predicted from first principles that the isotropic Knight shift, a hyperfine contribution to the nuclear magnetic resonance chemical shift, in metallic carbon nanotubes depends on the nanotube diameter. This can be practically used in nuclear magnetic resonance studies of these nanostructures. The knowledge of hyperfine interactions has some implications for possible future applications of these materials in spintronics and quantum computing devices. Using a more general approach based on accurate calculations of small graphenic fragments, we found that the hyperfine

interactions can be described in local variables. This approach was also generalized to hyperfine couplings of nuclear spins of impurities and boundary functional groups. Such knowledge will permit the design of nanoscale structures with predefined hyperfine fields.

We also found that an itinerant magnetism in graphene is triggered by the presence of point defects. It originates from the defect-induced quasilocalized states and does not require the presence of highly reactive unsaturated dangling bonds. The overall magnetic correlation may have both ferromagnetic and antiferromagnetic character depending on the distribution of the defects over graphene sublattices. We believe that the defect-induced itinerant magnetism is responsible for experimental observations of ferromagnetism in irradiated graphite. Magnetic materials based on light elements like carbon may find important applications in technology. Finally, we investigated the mechanisms of the irradiation defect formation in layered carbon nanostructure. Using first principles molecular dynamics we performed simulations of knock-on displacements in a prototype model – graphite. We showed the crucial role played by the early stage dynamics, and we identified the conditions at which selective creation of defects can be achieved. In particular, we identified an interval of electron beam energies in which only low-energy intimate Frenkel pair defects bridging adjacent graphene layers are produced. We also concluded that Stone-Wales defects, characterized by the lowest formation energy, can not be produced selectively upon irradiation. Our results are of practical importance for radiation-assisted manufacturing of carbon materials and nanostructures with new desired properties and functions.

8.2 Perspectives

Scientific research as an area of human activity possess one unusual property: an answer to a question gives birth to new questions. This property is responsible for an accelerating technological progress of human society. Below I will provide only a few problems related to this thesis that will probably be solved in the near future.

We have successfully applied density functional theory to predict the hyperfine and quadrupolar components of the effective spin-Hamiltonian. There is another important term, the zero-field splitting - an effective interaction within the $S > 1/2$ electron spin system, which is responsible for the relaxation of electron spins in MRI contrast agents. Predicting this property accurately from molecular structure is a challenging (but not impossible) task.

Computer power available for scientific community grows continuously. Performing first principles molecular dynamics simulations on larger systems (MRI contrast agents in solution) and covering longer time scales (on the order of nanoseconds) will become possible in several years. This will bring computer aided design of MRI contrast agents to a new level of accuracy.

Although various mechanisms responsible for magnetism in carbon nanostructures have been predicted, there is no definitive proof in favor of one of them due to the lack of experimental observations. A reliable methodology for accurate predictions of Curie temperatures in such systems is also missing. One can foresee that this gap in knowledge will be closed in future.

Explaining the high efficiency of Gd-loaded carbon nanotubes as MRI contrast agents [316] is another priority problem. Both electronic interactions and molecular dynamics in such systems are unexplored. Understanding the underlying mechanisms of the high efficiency will initiate a rational search for even more efficient MRI contrast agents in new classes of chemical compounds and nanostructures.

Appendix A

Si $2p$ photoelectron spectra at silicon surfaces and interfaces

In this Appendix, we refer to the subject of X-ray photoelectron spectroscopy probing core-level electrons, a widely used experimental technique for studying the chemical composition of semiconductor surfaces and interfaces. At a glance, this topic seems to be loosely related to the subject of magnetism and hyperfine interactions. However, probing hyperfine interactions in “low-energy” magnetic resonance experiments and exciting core electrons with “high-energy” X-rays share an important property - a property of locality. As we will see below, due to the extreme degree of localization of core electrons, the X-ray photoemission spectroscopy provides an information about the vicinal electronic structure and, thus, about the local covalent neighborhood.

The increasing availability of synchrotron radiation facilities is bearing X-ray photoemission spectra of unprecedented resolution characterizing surfaces and interfaces [317]. The achieved sensitivity is sufficient to distinguish inequivalent subsurface atoms with identically composed first-neighbor shells (oxidation states). Hence, the interpretation of such core-level spectra can no longer be achieved with simple electronegativity arguments, but requires the consideration of the interplay between local strain fields and electronegativity effects of second-nearest neighbors. Thus, the challenges for theory not only involve the accuracy of computer simulations, but also the search for new paradigms to analyze the origin of the observed shifts.

These difficulties are strikingly illustrated for the Si(100) 2×1 surface, which has been the object of numerous highly resolved X-ray photoemission investigations [319, 321–323]. While the shifts pertaining to the first-layer dimer atoms have been identified [321, 324],

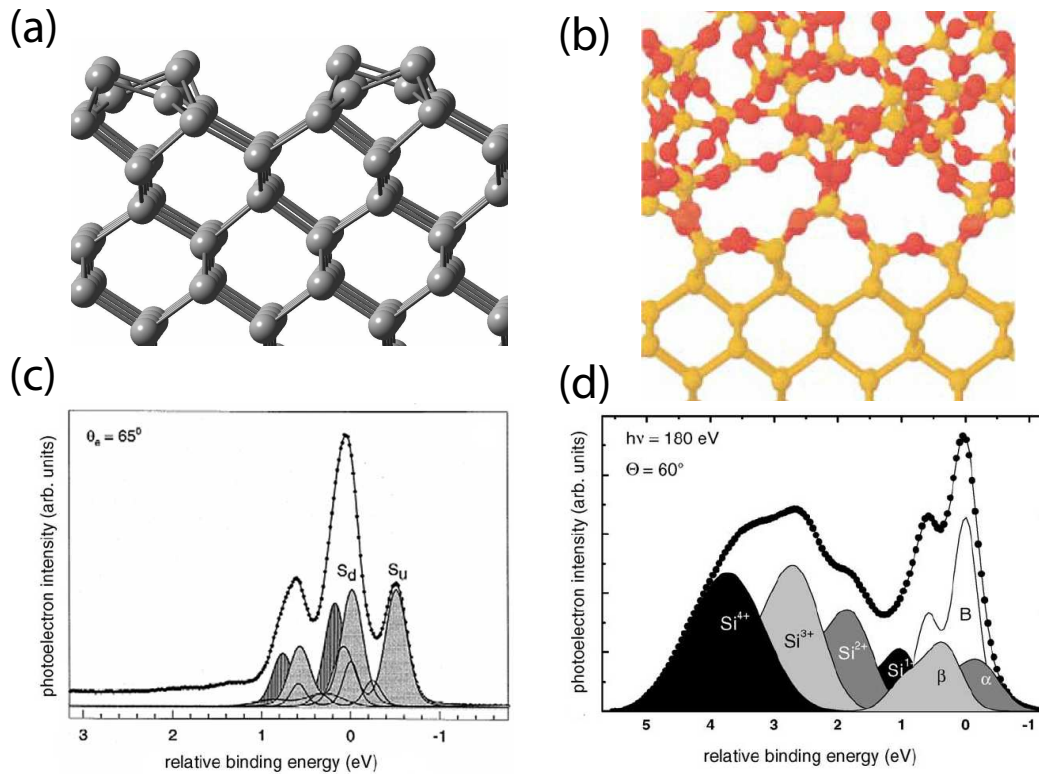


Figure A.1: Top: atomic structure of the Si(100)-*c*(4×2) surface (a) and one of the proposed models of Si(100)-SiO₂ interface (b) (O – red, Si – yellow) [318]. Bottom: Experimental XPS spectra of the Si(100) surface [319] and the Si(100)-SiO₂ interface [320]. Assigned signals corresponding to the surface dimer atoms and interface atoms with intermediate oxidation states (+1,+2,+3) as well as unassigned signals are shown.

the other lines appearing in highly resolved Si 2*p* spectra (Fig. A.1c) still lack a consensual assignment [319], despite the detailed knowledge of the surface reconstruction [325–327]. Even more interesting is the case of the Si(100)-SiO₂ interface, where the atomic structure connecting the crystalline Si with the amorphous oxide remains a debated issue [328–331]. While the partial oxidation states of Si [332] are by now well understood [333], highly resolved spectra show fine structure in the nonoxidized Si line, with extra components at lower (Si^α) and higher binding energy (Si^β) with respect to the Si bulk line (Fig. A.1d) [320, 334, 335]. These lines result from substrate Si atoms in the neighborhood of the interface, but the cause of their appearance has remained obscure. Understanding their origin might shed light on the bonding pattern at this technologically relevant interface [320, 330, 331].

We here investigate the origin of the fine structure in Si $2p$ photoemission spectra at silicon surfaces and interfaces. At the Si(100) 2×1 surface, our calculated shifts account for the experimental data and show that at least three Si layers are detected. Our interpretation highlights a linear relation between shifts and bond lengths. Adopting a recently generated model structure [328], we calculate Si $2p$ shifts at the Si(100)-SiO₂ interface and find quantitative agreement with experimental data, for both oxidized (Si^{+ n} , with $n=1,\dots,4$) and nonoxidized Si atoms (Si ^{α} , Si ^{β}). Having recourse to maximally localized Wannier functions [336], we clarify the origin of the fine structure, identifying the respective roles of second-neighbor O atoms and of local strain. The shift associated to the Si ^{β} line is found to give a direct measure of substrate distortions at the Si(100)-SiO₂ interface.

Electronic-structure calculations and structural relaxations were performed within the local density approximation (LDA) to density functional theory. Only valence electrons were explicitly described and core-valence interactions were accounted for through pseudopotentials (PPs) [131, 132]. We used a normconserving PP for Si [151] and an ultrasoft one for O [186]. The electron wave functions were described by plane-wave basis sets determined by an energy cutoff of 25 Ry. The cutoff was increased to 35 Ry for systems with O atoms. The Brillouin zone could be sampled at the only Γ point, since all the investigated systems are of sufficiently large size.

Table A.1: Silicon $2p$ core-level shifts associated to the central Si atom in SiO _{n} (SiH₃)₄, as calculated with pseudopotential (PP) and all-electron (AE) schemes. The shifts (in eV) are given with respect to the central Si atom in Si(SiH₃)₄.

n	1	2	3	4
PP	0.83	1.50	2.10	2.85
AE	0.82	1.48	2.08	2.82

To interpret the Si $2p$ photoelectron spectra at silicon surfaces and interfaces, it is necessary to evaluate core-level *shifts* with respect to the Si bulk line. Since these shifts mainly result from the relaxation of *valence* electron states, their accurate determination is possible within a PP scheme, which does not treat core electrons explicitly [324, 333, 337, 338]. We calculated Si $2p$ shifts including the effect of core-hole relaxation by taking total energy differences between two separate self-consistent calculations. First, the ground-state energy is determined; then the PP of a given Si atom is replaced by

another PP which simulates the presence of a screened 2p hole in its core [324]. Upon electron excitation, the atomic positions are not allowed to relax in accordance with the sudden approximation [324], and a neutralizing background is used to ensure overall charge neutrality. Test calculations showed that *relative* Si 2p binding energies are negligibly affected when considering spin-polarized core holes or using generalized gradient approximations for the exchange-correlation energy [338]. Hence, all the shifts in this work were consistently determined in the LDA.

To illustrate the accuracy of our scheme, we focused on model molecules containing Si in various oxidation states [333], for which all electron (AE) calculations could be performed (we performed all-electron calculations with the code ADF [89] using the triple-zeta doubly polarized STO basis set). In our AE calculations, the electronic state in the presence of a core hole was obtained by enforcing the occupation of the corresponding core orbital. We found deviations of at most 0.03 eV between PP and AE core-level shifts, over an energy range extending up to 3 eV (Table A.1). This comparison indicates that the PP scheme can give impressively accurate shifts for a series of similarly bonded atoms [338].

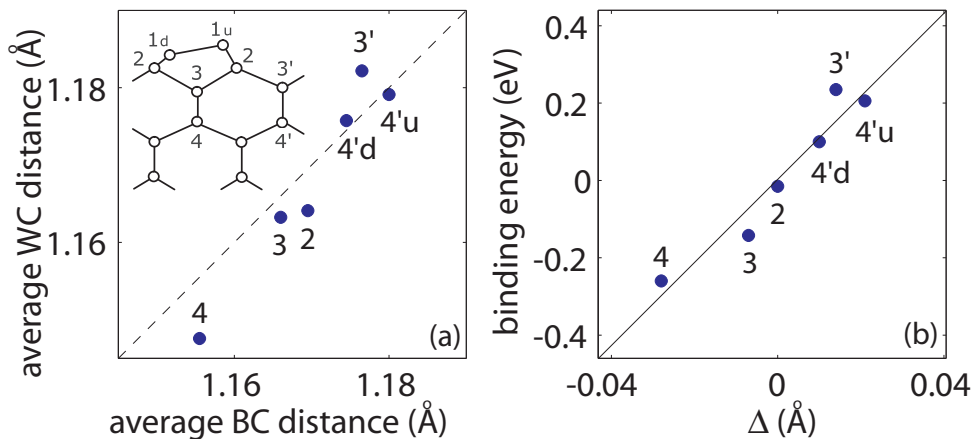


Figure A.2: Correlations for subsurface Si atoms at the Si(001)- $c(4\times 2)$ surface: (a) average distance to the Wannier center (WC) vs average distance to the Si-Si bond center (BC); (b) Si 2p shift vs average Si-Si bond length given as deviation (Δ) with respect to the bulk (2.34 Å). The inset gives the adopted labeling. The 4' atoms can be further separated into inequivalent up (4'u) and down (4'd) atoms (the projections of 4'u (4'd) atoms on the surface plane lie between 1d (1u) atoms of different dimer rows).

To understand the behavior of core-level shifts in absence of important electroneg-

ativity effects, we first modeled the Si(100)- $c(4\times 2)$ surface. We used a slab geometry in a periodically repeated simulation cell, consisting of 14 Si layers with a 4×4 repeat unit in the surface plane. The distance (8 Å) between the slab and its periodic images was taken sufficiently large to neglect spurious interactions. The eight lowest layers were kept fixed in bulk positions and their extremities were saturated with H atoms. Through structural relaxation, we recovered the well-known surface reconstruction consisting of alternating buckled dimers. The tilt angle in our calculation (19°) agrees well with both experimental measurements [326] and previous theoretical work [327]. The notation that we adopted to distinguish the Si atoms is given in Fig. A.2.

Table A.2: Calculated and measured Si $2p$ shifts at the Si(001)- $c(4\times 2)$ surface. The shifts (in eV) are given with respect the Si bulk line. The theoretical reference is obtained from an average of deep Si atoms (5th–10th layer).

	Theory		Experiment	
	Present	Ref. [321]	Ref. [322]	Ref. [319]
$1u$	-0.49	-0.49	-0.49	-0.50
$1d$	0.02	0.06	0.06	0.06
2	-0.01			
3	-0.14	-0.21	-0.20	-0.21
4	-0.26			
$3'$	0.24	0.22	0.20	0.23
$4'u$	0.21			
$4'd$	0.10			

In Table A.2 we give calculated binding energies for this surface structure, together with experimental data from various sources [319, 321, 322]. The calculated shifts for the dimer atoms agree well with experimental values and confirm previous assignments [324]. The second-layer atoms are found to yield very small shifts (-0.01 eV), noticeably smaller than in a previous calculation (0.13 eV) [324]. Third- and fourth-layer atoms give shifts to both lower (3, 4) and higher binding energies ($3'$, $4'$) with respect to the Si bulk line. Shifts of deeper layers are negligible.

These results lead us to propose a different interpretation than adopted so far in the literature (Table A.2). Second-layer atoms with their small shift are indistinguishable from the bulk. The clear experimental signatures at about 0.2 eV and -0.2 eV [319,

321, 322] then correspond to the two inequivalent atoms in the third layer, possibly with a contribution of fourth-layer atoms that behave similarly. The absence of shifts higher than 0.3 eV in our clean surface model is consistent with the experimental assignment of the high-binding-energy features to defects or surface loss structures [319, 323].

In order to elucidate the origin of core-level shifts of subsurface atoms, we carried out an analysis in terms of maximally localized Wannier functions (MLWFs) [336], which conveniently represent the local electronic structure in a compact form. We focus on the initial state because core-hole relaxation effects are expected to scale linearly with the full shift for atoms in similarly bonded environments [333]. For a nonpolar Si-Si bond, the center of mass of the corresponding MLWF coincides with the center of the bond (Fig. A.3a). Therefore, a deviation between the positions of these two centers is an indicator of polarity in the bond. For each subsurface Si atom, we correlate in Fig. A.2(a) the distances to these two centers and find overall good correspondence. Hence, the polarity induced by ionic surface dimers is minor in subsurface layers.

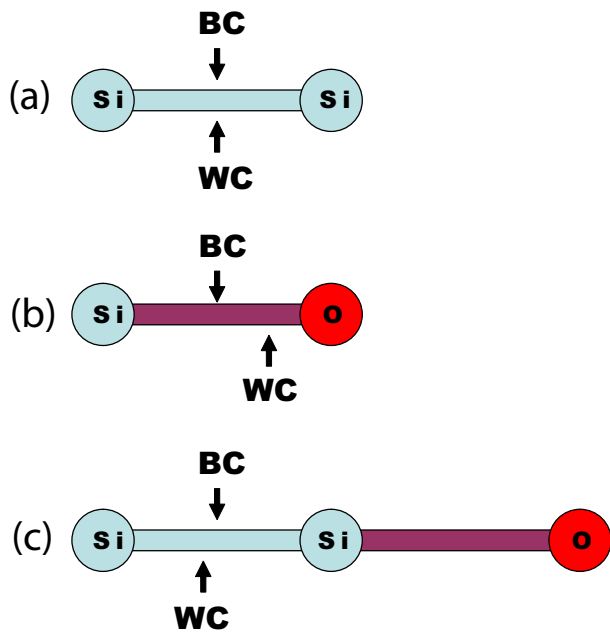


Figure A.3: Relative positions of Wannier centers (WC) and bond centers (BC) of the homopolar Si-Si bond (a), the heteropolar Si-O bond (b) and the Si-Si bond with second neighbor O atom (c).

The behavior of core-level shifts of subsurface atoms is understood through a simple correlation with Si-Si bond distances. For a given Si atom, the elongation of its bond distances leads to a decrease of the local electron density, resulting in a higher binding energy. This reasoning should also apply to other covalently bonded systems. An opposite dependence on strain is found for 3*d*-metal clusters due to hybridization effects [339]. The

validity of this correlation is demonstrated in Fig. A.2(b), which gives the calculated shifts vs. the average Si-Si distance to the four neighbor atoms. Therefore, the measured shift provides a direct indication of the local strain induced by the surface reconstruction. These considerations are general and also apply to other systems. As/Sb covered Si(100) surfaces show subsurface strain patterns and core-level shifts qualitatively similar to the clean surface studied here [340]. From experimental work on strained Si layers deposited on Ge(100) and SiGe alloys, one derives that the Si $2p$ binding energy increases with tensile strain [341, 342], in accord with the present analysis.

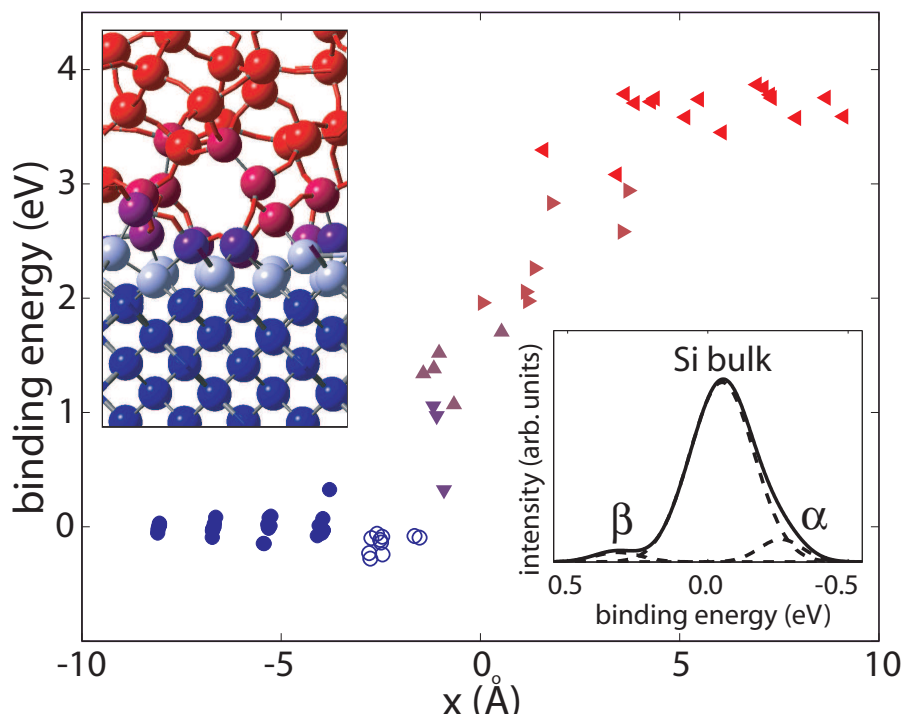


Figure A.4: Calculated Si $2p$ shifts at the Si(100)-SiO₂ interface along an orthogonal direction to the interface. The Si^{+ n} correspond to oxidized Si atoms with n O neighbors ($n=1$ - \blacktriangledown , 2 - \blacktriangle , 3 - \blacktriangleright , 4 - \blacktriangleleft) and are color-coded in the atomistic model. Nonoxidized Si atoms (Si⁰) with (\circ) and without (\bullet) second-neighbor O atoms are distinguished. Inset: simulated spectrum for Si⁰ (Gaussian broadened: $\sigma=0.08$ eV) and its decomposition in three components.

We now turn to the Si(100)-SiO₂ interface where the presence of highly electronegative O atoms might additionally affect the shifts of nonoxidized Si atoms [334]. As interface structure, we adopted model C' from Ref. [328], which incorporates several experimentally identified features, including a displacement pattern in the substrate consistent with ion-scattering measurements. Calculated binding energies are given in Fig. A.4 along

the direction orthogonal to the interface plane. The binding energies of oxidized Si atoms increase almost linearly with oxidation state [332, 333, 337], and show quantitative agreement with experimental values (Table A.3). The focus of the present investigation is on nonoxidized Si atoms, which give shifts with a significant spread near the interface. The simulated spectrum associated to these Si atoms could be decomposed into three components (Fig. A.4, inset), yielding shifts for Si^α and Si^β in very good agreement with experimental data (Table A.3).

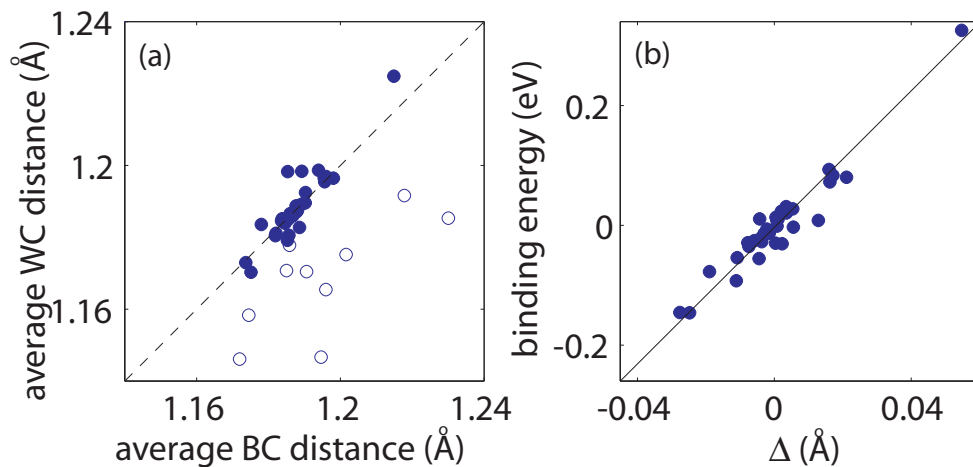


Figure A.5: Correlations for nonoxidized Si atoms at the Si(100)-SiO₂ interface: (a) average distance to the Wannier center (WC) vs average distance to the Si-Si bond center (BC); (b) Si 2p shift vs average Si-Si bond length given as deviation (Δ) from the bulk value. Closed (open) symbols indicate Si atoms without (with) second-neighbor O atoms.

Following the same analysis as for the Si(100)2 \times 1 surface, we identify second-neighbor electronegativity effects at the interface by monitoring deviations between the positions of bond centers and Wannier centers. For each nonoxidized Si atom, we correlate in Fig. A.5(a) the distances to these two centers, distinguishing nonoxidized Si atoms with and without second-neighbor O atoms. In absence of second-neighbor O atoms the Wannier center almost coincides with the Si-Si bond center, indicating that the electronegativity of O atoms does not affect third-neighbor bonds. However, for Si* atoms with second-neighbor O atoms, the Wannier center systematically moves closer to the Si* atom. This behavior is understood by considering that the central Si atom in a Si*-Si-O unit requires a contribution from its 4s atomic orbital in order to accommodate the polarity in its Si-O bond, which in turn displaces the Wannier center of the Si*-Si bond towards Si* (Fig.

Table A.3: Calculated and measured Si 2*p* shifts (in eV) at the Si(100)-SiO₂ interface. The Si bulk line is taken as reference.

	Theory		Experiment	
	Present	Ref. [335]	Ref. [320]	
α	-0.21	-0.25	-0.22	
β	0.32	0.20	0.34	
+1	0.78	1.00	0.95	
+2	1.40	1.82	1.78	
+3	2.37	2.62	2.60	
+4	3.64	3.67	3.72	

A.3c). In an equivalent way, this effect can be explained within the back-donation picture [343].

The displacement of the electron density towards the Si atom causes a decrease of its binding energy as can clearly be seen in Fig. A.4, where all the Si atoms with second-neighbor O atoms show negative shifts. Hence, a highly electronegative atom in the *second*-neighbor shell causes an *opposite* effect on the shift as compared to such an atom in the *first*-neighbor shell [333,337]. Consequently, Si atoms with second-neighbor O atoms contribute to the Si ^{α} line on the low binding energy side of the Si bulk line.

We now focus on nonoxidized Si atoms without second-neighbor O atoms. Figure A.5(b) shows that for these atoms a linear relation holds between their core-level shift and their average Si-Si bond distance, in a similar way as for the Si(100)2 \times 1 surface. We deduce that these shifts are the result of bond length variations induced in the substrate by the disordered oxide. Contracted bonds give negative shifts and contribute to the Si ^{α} component, in addition to second-neighbor electronegativity effects. On the contrary, bond elongations cause shifts towards higher binding energies, being at the origin of the Si ^{β} component. From the experimental shift of about 0.3 eV, we infer the occurrence of Si atoms with an average bond length elongation of ~ 0.05 Å.

Our analysis suggests that Si atoms contributing to the Si ^{α} line should on average be closer to the oxide than those contributing to Si ^{β} , at variance with a recent photodiffraction measurement favoring the opposite ordering [320]. However, the different sources of the Si ^{α} line together with the nonabrupt nature of the interface might lead to intermixing of Si ^{α} and Si ^{β} atoms, resulting in depth profiles at the limit of experimental resolution.

In conclusion, we revealed the mechanisms underlying the fine structure in Si $2p$ photoelectron spectra at silicon surfaces and interfaces. A key result of our work is that photoelectron spectroscopy when combined with first-principles calculations can provide an atomic-scale probe of structural strain, resulting in a new functionality in addition to the detection of chemical composition.

Bibliography

- [1] F. Bloch, Phys. Rev. **70**, 460 (1946).
- [2] F. Bloch, W. W. Hansen, and M. Packard, Phys. Rev. **70**, 474 (1946).
- [3] E. M. Purcell, H. C. Torrey, and R. V. Pound, Phys. Rev. **69**, 37 (1946).
- [4] R. V. Damadian, Science **171**, 1151 (1971).
- [5] P. G. Lauterbur, Nature **242**, 190 (1973).
- [6] P. Mansfield and P. K. Grannell, J. Phys. C **6**, L422 (1973).
- [7] P. Mansfield, J. Phys. C **10**, L55 (1977).
- [8] R. Damadian, M. Goldsmith, and L. Minkoff, Physiol. Chem. Phys. **9**, 97 (1977).
- [9] A. Kumar, D. Welti, and R. R. Ernst, J. Magn. Reson. **18**, 69 (1975).
- [10] C. Weiller, A. May, M. Sach, C. Buhmann, and M. Rijntjes, J. Magn. Reson. Imaging **23**, 840 (2006).
- [11] R. A. De Graaf and D. L. Rothman, J. Magn. Reson. **13**, 32 (2001).
- [12] D. Le Bihan, J.-F. Mangin, C. Poupon, C. A. Clark, S. Pappata, N. Molko, and H. Chabriat, J. Magn. Reson. Imaging **13**, 534 (2001).
- [13] P. Caravan, J. J. Ellison, T. J. McMurry, and R. B. Lauffer, Chem. Rev. **99**, 2293 (1999).
- [14] I. Solomon, Phys. Rev. **99**, 559 (1955).
- [15] I. Solomon and N. Bloembergen, J. Chem. Phys. **25**, 261 (1956).

- [16] N. Bloembergen, *J. Chem. Phys.* **27**, 572 (1957).
- [17] N. Bloembergen and L. Morgan, *J. Chem. Phys.* **34**, 842 (1961).
- [18] D. H. Powell, O. M. N. Dhubhghaill, D. Pubanz, L. Helm, Y. S. Lebedev, W. Schlaepfer, and A. E. Merbach, *J. Am. Chem. Soc.* **118**, 9333 (1996).
- [19] H. W. Kroto, J. R. Heath, S. C. O'Brien, R. F. Curl, and R. E. Smalley, *Nature* **318**, 162 (1985).
- [20] S. Iijima, *Nature* **354**, 56 (1991).
- [21] S. H. Baughman, A. A. Zakhidov, and W. A. de Heer, *Science* **297**, 787 (2002).
- [22] K. S. Novoselov, A. K. Geim, S. V. Morozov, D. Jiang, Y. Zhang, S. V. Dubonos, I. V. Grigorieva, and A. A. Firsov, *Science* **306**, 666 (2004).
- [23] C. Berger, Z. Song, T. Li, X. Li, A. Y. Ogbazghi, R. Feng, Z. Dai, A. N. Marchenkov, E. H. Conrad, P. N. First, and W. A. d. Heer, *J. Phys. Chem. B* **108**, 19912 (2004).
- [24] K. S. Novoselov, A. K. Geim, S. V. Morozov, D. Jiang, M. I. Katsnelson, I. V. Grigorieva, S. V. Dubonos, and A. A. Firsov, *Nature* **438**, 197 (2005).
- [25] Y. B. Zhang, Y. W. Tan, H. L. Stormer, and P. Kim, *Nature* **438**, 201 (2005).
- [26] P. R. Wallace, *Phys. Rev.* **71**, 622 (1947).
- [27] J. W. Mintmire and C. T. White, *Phys. Rev. Lett.* **81**, 2506 (1998).
- [28] B. Obradovic, R. Kotlyar, F. Heinz, P. Matagne, T. Rakshit, M. D. Giles, M. A. Stettler, and D. E. Nikonov, *Appl. Phys. Lett.* **88**, 142102 (2006).
- [29] P. C. Collins, M. S. Arnold, and P. Avouris, *Science* **292**, 706 (2001).
- [30] C. Berger, Z. Song, X. Li, X. Wu, N. Brown, C. Naud, D. Mayou, T. Li, J. Hass, A. N. Marchenkov, E. H. Conrad, P. N. First, and W. A. d. Heer, *Science* **312**, 1191 (2006).
- [31] Z. Chen, Y.-M. Lin, M. J. Rooks, and P. Avouris, *cond-mat/0701599*.
- [32] I. Žutić, J. Fabian, and S. Das Sarma, *Rev. Mod. Phys.* **76**, 323 (2004).

- [33] K. Tsukagoshi, B. W. Alphenaar, and H. Ago, *Nature* **401**, 572 (1999).
- [34] E. W. Hill, A. K. Geim, K. Novoselov, F. Schedin, and P. Blake, *IEEE Transaction on Magnetics* **42**, 2694 (2006).
- [35] L. E. Hueso, J. M. Pruneda, V. Ferrari, G. Burnell, J. P. Valdés-Herrera, B. D. Simons, P. B. Littlewood, E. Artacho, A. Fert, and N. D. Mathur, *Nature* **445**, 410 (2007).
- [36] M. Takahashi, P. Turek, Y. Nakazawa, M. Tamura, K. Nozawa, D. Shiomi, M. Ishikawa, and M. Kinoshita, *Phys. Rev. Lett.* **67**, 746 (1991).
- [37] T. L. Makarova, B. Sundqvist, R. Hohne, P. Esquinazi, Y. Kopelevich, P. Scharff, V. A. Davydov, L. S. Kashevarova, and A. V. Rakhmanina, *Nature* **413**, 716 (2001).
- [38] T. L. Makarova, B. Sundqvist, R. Höhne, P. Esquinazi, Y. Kopelevich, P. Scharff, V. Davydov, L. S. Kashevarova, and A. V. Rakhmanina, *Nature* **440**, 707 (2006).
- [39] P. Esquinazi, D. Spemann, R. Höhne, A. Setzer, K.-H. Han, and T. Butz, *Phys. Rev. Lett.* **91**, 227201 (2003).
- [40] K.-H. Han, D. Stepmann, P. Esquinazi, R. Höhne, V. Riede, and T. Butz, *Adv. Mater.* **15**, 1719 (2003).
- [41] A. Hashimoto, K. Suenaga, A. Gloter, K. Urita, and S. Iijima, *Nature* **430**, 870 (2004).
- [42] K. Urita, K. Suenaga, T. Sugai, H. Shinohara, and S. Iijima, *Phys. Rev. Lett.* **94**, 155502 (2005).
- [43] A. Kis, G. Csányi, J.-P. Salvetat, T.-N. Lee, E. Couteau, A. J. Kulik, W. Benoit, J. Brugger, and L. Forró, *Nat. Mater.* **3**, 153 (2004).
- [44] I. Bertini, Y.-M. Lee, C. Luchinat, M. Piccioli, and L. Poggi, *CHEMBIOCHEM* **2**, 550 (2001).
- [45] E. Tóth, L. Helm, and A. E. Merbach, in *The Chemistry of Contrast Agents in Medical Magnetic Resonance Imaging*, edited by E. Tóth and A. E. Merbach (Wiley, Chichester, 2001).

- [46] E. Tóth, L. Helm, and A. E. Merbach, in *Topics in Current Chemistry*, edited by W. Krause (Springer-Verlag, Berlin, 2002), Vol. 221, pp. 62–101.
- [47] L. Helm, E. Tóth, and A. E. Merbach, *Lanthanide ions as magnetic resonance imaging agents. Nuclear and electronic relaxation properties. Applications.*, Vol. 40 of *Metal Ions in Biological Systems* (M. Dekker, New York, 2003).
- [48] E. Tóth, L. Helm, and A. E. Merbach, in *In Comprehensive Coordination Chemistry II*, edited by J. A. McCleverty and T. Y. Meyer (Elsevier, Oxford, UK, 2004), Vol. 9, pp. 841–881.
- [49] I. Bertini, C. Luchinat, and G. Parigi, *Concepts Magn. Reson.* **14**, 259286 (2002).
- [50] M. Allegrozzi, I. Bertini, M. B. L. Janik, Y.-M. Lee, G. Liu, and C. Luchinat, *J. Am. Chem. Soc.* **122**, 4154 (2000).
- [51] S. Aime, N. DAmelio, M. Fragai, Y.-M. Lee, C. Luchinat, E. Terreno, and G. Valensin, *J. Biol. Inorg. Chem.* **7**, 617622 (2002).
- [52] G. Pintacuda and G. Otting, *J. Am. Chem. Soc.* **124**, 372 (2002).
- [53] J. Iwahara, C. D. Schwieters, and G. M. Clore, *J. Am. Chem. Soc.* **126**, 5879 (2004).
- [54] J. Kowalewski, A. Laaksonen, L. Nordenskiöld, and M. Blomberg, *J. Chem. Phys.* **74**, 2927 (1981).
- [55] L. Nordenskiöld, A. Laaksonen, and J. Kowalewski, *J. Am. Chem. Soc.* **104**, 379 (1982).
- [56] J. Kowalewski, L. Nordenskiöld, N. Benetis, and P.-O. Westlund, *Progr. NMR Spectrosc.* **17**, 141 (1985).
- [57] N. Sahoo and T. P. Das, *J. Chem. Phys.* **91**, 7740 (1989).
- [58] N. Sahoo and T. P. Das, *J. Chem. Phys.* **93**, 1200 (1990).
- [59] K. R. Lata, N. Sahoo, and T. P. Das, *J. Chem. Phys.* **94**, 3715 (1991).
- [60] S. J. Wilkens, B. Xia, B. F. Volkman, F. Weinhold, J. L. Markley, and W. M. Westler, *J. Phys. Chem. B* **102**, 8300 (1998).

- [61] L. Maron and O. Eisenstein, *J. Phys. Chem. A* **104**, 7140 (2000).
- [62] *Calculation of NMR and EPR parameters: Theory and Applications*, edited by M. Kaupp, M. Bühl, and V. G. Malkin (Wiley-VCH, Weinheim, 2004).
- [63] J. E. Harriman, *Theoretical Foundation of Electron Spin Resonance*, Vol. 37 of *Physical Chemistry, a Series of Monographs* (Academic Press, New York, 1987).
- [64] C. Adamo, V. Barone, and R. Subra, *Theor. Chem. Acc.* **104**, 207 (2000).
- [65] H. P. W. Gottlieb, M. Barfield, and D. M. Doddrell, *J. Chem. Phys.* **67**, 3785 (1977).
- [66] J. Mispelter, M. Momenteau, and J. Lhoste, in *Biological Magnetic Resonance: NMR of Paramagnetic Molecules*, edited by L. J. Berliner and J. Reuben (Plenum Press, New York, 1993), Vol. 12, pp. 299–355.
- [67] D. F. Hansen and J. J. Led, *J. Am. Chem. Soc.* **126**, 1247 (2004).
- [68] A. Borel, L. Helm, and C. A. E. Daul, *Chem. Phys. Lett.* **383**, 584 (2004).
- [69] H. Ohtaki and T. Radnai, *Chem. Rev.* **93**, 1157 (1993).
- [70] V. G. Malkin, O. L. Malkina, G. Steinebrunner, and H. Huber, *Chem. Eur. J.* **2**, 452 (1996).
- [71] R. Eggenberger, S. Gerber, H. Huber, D. Searles, and M. Welker, *J. Mol. Spectrosc.* **151**, 474 (1992).
- [72] H. Huber, *Z. Naturforsch.* **49a**, 103 (1994).
- [73] H. Takase and O. Kikuchi, *Chem. Phys.* **181**, 57 (1994).
- [74] J. R. Asher, N. L. Doltsinis, and M. Kaupp, *J. Am. Chem. Soc.* **126**, 9854 (2004).
- [75] W. L. Jorgensen, J. Chandrasekhar, and J. D. Madura, *J. Chem. Phys.* **79**, 926 (1983).
- [76] D. A. Case, D. A. Pearlman, J. W. Caldwell, T. E. Cheatham, W. S. Ross, C. L. Simmerling, T. A. Darden, K. M. Merz, R. V. Stanton, A. L. Cheng, J. J. Vincent, M. Crowley, V. Tsui, R. J. Radmer, Y. Duan, J. Pitera, I. Massova, G. L.

- Seibel, U. C. Singh, P. K. Weiner, and P. A. Kollman, AMBER 6.0, University of California, San Francisco, CA, 1999.
- [77] A. Borel, L. Helm, and A. E. Merbach, *Chem. Eur. J.* **7**, 600 (2001).
- [78] F. Yerly, A. Borel, L. Helm, and A. E. Merbach, *Chem. Eur. J.* **9**, 5468 (2003).
- [79] S. Aime, M. Botta, M. Fasano, M. P. M. Marques, C. Geraldes, D. Pubanz, and A. E. Merbach, *Inorg. Chem.* **36**, 2059 (1997).
- [80] P. Pyykkö, *Chem. Rev.* **88**, 563 (1988).
- [81] M. Dolg, H. Stoll, A. Savin, and H. Preuss, *Theor. Chim. Acta* **75**, 173 (1989).
- [82] T. R. Cundari and T. J. Stevens, *J. Chem. Phys.* **98**, 5555 (1993).
- [83] M. Dolg, W. Liu, and S. Kaldova, *Int. J. Quant. Chem.* **76**, 359 (2000).
- [84] C. Adamo and V. Barone, *J. Comput. Chem.* **21**, 1153 (2000).
- [85] M. Douglas and M. N. Kroll, *Ann. Phys. (N. Y.)* **82**, 89 (1974).
- [86] E. van Lenthe, E. J. Baerends, and J. G. Snijders, *J. Chem. Phys.* **99**, 4597 (1993).
- [87] E. van Lenthe, E. J. Baerends, and J. G. Snijders, *J. Chem. Phys.* **101**, 9783 (1994).
- [88] M. J. Frisch, G. W. Trucks, H. B. Schlegel, G. E. Scuseria, M. A. Robb, J. R. Cheeseman, J. A. Montgomery, T. V. Jr., K. N. Kudin, J. C. Burant, J. M. Millam, S. S. Iyengar, J. Tomasi, V. Barone, B. Mennucci, M. Cossi, G. Scalmani, N. Rega, G. A. Petersson, H. Nakatsuji, M. Hada, M. Ehara, K. Toyota, R. Fukuda, J. Hasegawa, M. Ishida, T. Nakajima, Y. Honda, O. Kitao, H. Nakai, M. Klene, X. Li, J. E. Knox, H. P. Hratchian, J. B. Cross, C. Adamo, J. Jaramillo, R. Gomperts, R. E. Stratmann, O. Yazyev, A. J. Austin, R. Cammi, C. Pomelli, J. W. Ochterski, P. Y. Ayala, K. Morokuma, G. A. Voth, P. Salvador, J. J. Dannenberg, V. G. Zakrzewski, S. Dapprich, A. D. Daniels, M. C. Strain, O. Farkas, D. K. Malick, A. D. Rabuck, K. Raghavachari, J. B. Foresman, J. V. Ortiz, Q. Cui, A. G. Baboul, S. Clifford, J. Cioslowski, B. B. Stefanov, G. Liu, A. Liashenko, P. Piskorz, I. Komaromi, R. L. Martin, D. J. Fox, T. Keith, M. A. Al-Laham, C. Y. Peng, A. Nanayakkara, M. Challacombe, P. M. W. Gill, B. Johnson, W. Chen, M. W. Wong, C. Gonzalez, and J. A. Pople, *Gaussian 03, Revision C.1*, 2004.

- [89] ADF2003.01, SCM, Theoretical Chemistry, Vrije Universiteit, Amsterdam, The Netherlands, <http://www.scm.com>.
- [90] F. Neese, *J. Chem. Phys.* **118**, 3939 (2003).
- [91] C. Remenyi, R. Reviakine, A. V. Arbuznikov, J. Vaara, and M. Kaupp, *J. Phys. Chem. A* **108**, 5026 (2004).
- [92] M. L. Munzarovà and M. Kaupp, *J. Phys. Chem. A* **103**, 9966 (1999).
- [93] M. L. Munzarovà, P. Kubáček, and M. Kaupp, *J. Am. Chem. Soc.* **122**, 11900 (2000).
- [94] T. Nakajima and K. Hirao, *J. Chem. Phys.* **116**, 8270 (2002).
- [95] W. Kutzelnigg, U. Fleischer, and M. Schindler, *NMR-Basic Principles and Progress* (Springer-Verlag, Heidelberg, 1990), Vol. 23.
- [96] D. B. Chesnut and K. D. Moore, *J. Comput. Chem.* **10**, 648 (1989).
- [97] F. Neese, *J. Phys. Chem. A* **105**, 4290 (2001).
- [98] A. D. Becke, *Phys. Rev. A* **38**, 3098 (1988).
- [99] J. P. Perdew and Y. Wang, *Phys. Rev. B* **45**, 13244 (1992).
- [100] A. D. Becke, *J. Chem. Phys.* **98**, 5648 (1993).
- [101] K. Micskei, D. H. Powell, L. Helm, E. Brcher, and A. E. Merbach, *Mag. Reson. Chem.* **31**, 1011 (1993).
- [102] J. Reuben and D. Fiat, *J. Chem. Phys.* **51**, 4909 (1969).
- [103] A. M. Raitsimring, A. V. Astashkin, D. Baute, D. Goldfarb, and P. Caravan, *J. Phys. Chem. A* **108**, 7318 (2004).
- [104] O. V. Yazyev, I. Tavernelli, L. Helm, and U. Röthlisberger, *Phys. Rev. B* **71**, 115110 (2005).
- [105] A. V. Astashkin, A. M. Raitsimring, and P. Caravan, *J. Phys. Chem. A* **108**, 1990 (2004).

- [106] R. DeBeer, F. Biesboef, and D. V. Ormondt, *Physica B* **83**, 314 (1976).
- [107] C. C. Bryden, C. N. Reilley, and J. F. Desreux, *Anal. Chem.* **53**, 1418 (1981).
- [108] C. A. Chang, L. C. Francesconi, M. F. Malley, K. Kumar, J. Z. Gougoutas, M. F. Tweedle, D. W. Lee, and L. J. Wilson, *Inorg. Chem.* **32**, 3501 (1993).
- [109] S. Bénazeth, J. Purans, M. Chalbot, M. K. Nguyen-van Duong, N. Louisette, F. Keller, and A. Gaudemer, *Inorg. Chem.* **37**, 3667 (1998).
- [110] L. G. Werbelow, *J. Chem. Phys.* **104**, 3457 (1996).
- [111] E. A. C. Lucken, *Nuclear Quadrupole Coupling Constants* (Academic, London, 1969).
- [112] A. Jerschow, *Progr. NMR Spectrosc.* **46**, 63 (2005).
- [113] H. G. Hertz, *Ber. Bunsenges. Phys. Chem.* **65**, 20 (1961).
- [114] H. G. Hertz, in *Water - A comprehensive treatise*, edited by F. Franks (Plenum, New York, 1973), Vol. 3, p. 301.
- [115] H. G. Hertz, *Ber. Bunsenges. Phys. Chem.* **77**, 531 (1973).
- [116] H. G. Hertz, *Ber. Bunsenges. Phys. Chem.* **77**, 688 (1973).
- [117] J. E. Gready, *J. Phys. Chem.* **88**, 3497 (1984).
- [118] D. M. Bishop and S. M. Cybulski, *J. Chem. Phys.* **100**, 6628 (1994).
- [119] H. Huber, *Chimia* **49**, 404 (1995).
- [120] R. Ludwig, F. Weinhold, and T. C. Farrar, *J. Chem. Phys.* **103**, 6941 (1995).
- [121] R. Ludwig, F. Weinhold, and T. C. Farrar, *J. Chem. Phys.* **105**, 8223 (1996).
- [122] W. C. Bailey, *Chem. Phys. Lett.* **292**, 71 (1998).
- [123] A. Rizzo, K. Ruud, T. Helgaker, and M. Jaszunski, *J. Chem. Phys.* **109**, 2264 (1998).
- [124] G. De Luca, N. Russo, A. M. Köster, P. Calaminici, and K. Jug, *Mol. Phys.* **97**, 347 (1999).

- [125] B. Kirchner, D. J. Searles, A. J. Dyson, P. S. Vogt, and H. Huber, *J. Am. Chem. Soc.* **122**, 5379 (2000).
- [126] L. Olsen, O. Christiansen, L. Hemmingsen, S. P. A. Sauer, and K. V. Mikkelsen, *J. Chem. Phys.* **116**, 1424 (2002).
- [127] E. H. Hardy, M. G. Müller, P. S. Vogt, C. Bratschi, B. Kirchner, H. Huber, and D. J. Searles, *J. Chem. Phys.* **119**, 6184 (2003).
- [128] T. S. Pennanen, J. Vaara, P. Lantto, A. J. Sillanpää, K. Laasonen, and J. Jokisaari, *J. Am. Chem. Soc.* **126**, 11093 (2004).
- [129] P. L. Cummins, G. B. Bacskay, and N. S. Hush, *J. Chem. Phys.* **87**, 416 (1987).
- [130] B. Meyer, K. Hummler, C. Elsasser, and M. Fähnle, *J. Phys.: Cond. Matter* **7**, 9201 (1995).
- [131] R. Car and M. Parrinello, *Phys. Rev. Lett.* **55**, 2471 (1985).
- [132] CPMD version 3.9.1, Copyright IBM Corp 1990-2004, Copyright MPI für Festkörperforschung Stuttgart 1997-2001, <http://www.cpmc.org>.
- [133] P. Pyykkö, *Z. Naturforsch.* **47a**, 189 (1992).
- [134] J. Verhoeven, A. Dynamus, and H. Bluysen, *J. Chem. Phys.* **50**, 3330 (1969).
- [135] I.-F. W. Kuo, C. J. Mundy, M. J. McGrath, J. I. Siepmann, J. VandeVondele, M. Sprik, J. Hutter, B. Chen, M. L. Klein, F. Mohamed, M. Krack, and M. Parrinello, *J. Phys. Chem. B* **108**, 12990 (2004).
- [136] Y. A. Mantz, B. Chen, and G. J. Martyna, *J. Phys. Chem. B* **110**, 3540 (2006).
- [137] C. Cossy, L. Helm, D. H. Powell, and A. E. Merbach, *New J. Chem.* **19**, 27 (1995).
- [138] T. Kowall, F. Foglia, L. Helm, and A. E. Merbach, *J. Phys. Chem.* **99**, 13078 (1995).
- [139] J. Ropp, C. Lawrence, T. C. Farrar, and J. L. Skinner, *J. Am. Chem. Soc.* **123**, 8047 (2001).
- [140] F. A. Dunand, A. Borel, and A. E. Merbach, *J. Am. Chem. Soc.* **124**, 710 (2002).

-
- [141] I. Bako, J. Hutter, and G. Palinkas, *J. Chem. Phys.* **117**, 9838 (2002).
- [142] B. Eliasson, K. M. Larsson, and J. Kowalewski, *J. Phys. Chem.* **89**, 258 (1985).
- [143] G. Gonzalez, D. H. Powell, V. Tissieres, and A. E. Merbach, *J. Phys. Chem.* **98**, 53 (1994).
- [144] R. P. W. J. Struis, J. d. Bleijser, and J. C. Layte, *J. Phys. Chem.* **91**, 6309 (1987).
- [145] W. E. Pickett, *Computer Physics Reports* **9**, 115 (1989).
- [146] W. Andreoni and A. Curioni, *Parallel Computing* **26**, 819 (2000).
- [147] C. G. Van de Walle and P. Blöchl, *Phys. Rev. B* **47**, 4244 (1993).
- [148] B. Hetényi, F. D. Angelis, P. Giannozzi, and R. Car, *J. Chem. Phys.* **115**, 5791 (2001).
- [149] D. Marx and J. Hutter, *Modern Methods and Algorithms in Quantum Chemistry* (NIC, Jülich, 2000), Vol. 1.
- [150] R. Declerck, E. Pauwels, V. Van Speybroeck, and M. Waroquier, *Phys. Rev. B* **74**, 245103 (2006).
- [151] N. Troullier and J. L. Martins, *Phys. Rev. B* **43**, 1993 (1991).
- [152] G. Arfken, *Mathematical Methods for Physicists, 3rd ed.* (Academic Press, Orlando, FL, 1985).
- [153] J. P. Perdew, K. Burke, and M. Ernzerhof, *Phys. Rev. Lett.* **77**, 3865 (1996).
- [154] D. M. Chipman, *Theor. Chim. Acta* **82**, 93 (1992).
- [155] E. Hirota and C. Yanada, *J. Mol. Spectrosc.* **96**, 175 (1985).
- [156] R. W. Fessenden, *J. Phys. Chem.* **71**, 74 (1967).
- [157] R. W. Fessenden and R. H. Schuler, *J. Chem. Phys.* **39**, 2147 (1963).
- [158] H. J. McManus, R. W. Fessenden, and D. M. Chipman, *J. Phys. Chem.* **92**, 3778 (1988).

- [159] H. J. McManus, R. W. Fessenden, and D. M. Chipman, *J. Phys. Chem.* **92**, 3781 (1988).
- [160] B. J. Boland, J. M. Brown, and A. Carrington, *Mol. Phys.* **34**, 453 (1977).
- [161] F. J. Adrian, B. F. Kim, and J. Bohandy, *J. Chem. Phys.* **82**, 1804 (1985).
- [162] E. L. Cochran, F. J. Adrian, and V. A. Bowers, *J. Chem. Phys.* **44**, 4626 (1966).
- [163] Z. Luz and A. Reuveni, *J. Chem. Phys.* **51**, 4017 (1969).
- [164] J. P. Perdew, *Phys. Rev. B* **33**, 8822 (1986).
- [165] D. Porezag, M. R. Pederson, and A. Y. Liu, *Phys. Rev. B* **60**, 14132 (1999).
- [166] S. G. Louie, S. Froyen, and M. L. Cohen, *Phys. Rev. B* **26**, 1738 (1982).
- [167] G. J. Martyna and M. E. Tuckerman, *J. Chem. Phys.* **110**, 2810 (1999).
- [168] S. Baroni, A. Dal Corso, S. de Gironcoli, P. Giannozzi, C. Cavazzoni, G. Balabio, S. Scandolo, G. Chiarotti, P. Focher, A. Pasquarello, K. Laasonen, A. Trave, R. Car, N. Marzari, and A. Kokalj, computer code **QUANTUM-ESPRESSO**, <http://www.quantum-espresso.org>, 2005.
- [169] L. M. Ramaniah, M. Bernasconi, and M. Parrinello, *J. Chem. Phys.* **111**, 1587 (1999).
- [170] D. J. Tobias, P. Jungwirth, and M. Parrinello, *J. Chem. Phys.* **114**, 7036 (2001).
- [171] A. Pasquarello, I. Petri, P. S. Salmon, O. Parisel, R. Car, E. Toth, D. H. Powell, H. E. Fischer, L. Helm, and A. E. Merbach, *Science* **291**, 856 (2001).
- [172] S. Raugei and M. L. Klein, *J. Chem. Phys.* **116**, 196 (2002).
- [173] J. Blumberger, L. Bernasconi, I. Tavernelli, R. Vuilleumier, and M. Sprik, *J. Am. Chem. Soc.* **126**, 3928 (2004).
- [174] A. Munoz-Paez and E. S. Marcos, *J. Am. Chem. Soc.* **114**, 6931 (1992).
- [175] A. Munoz-Paez, R. R. Pappalardo, and E. S. Marcos, *J. Am. Chem. Soc.* **117**, 11710 (1995).

- [176] S. Diáz-Moreno, A. Munoz-Paez, J. M. Martinez, R. R. Pappalardo, and E. S. Marcos, *J. Am. Chem. Soc.* **118**, 12654 (1996).
- [177] A. Bleuzen, F. Foglia, E. Furet, L. Helm, A. E. Merbach, and J. Weber, *J. Am. Chem. Soc.* **118**, 12777 (1996).
- [178] H. Sakane, A. Munoz-Paez, S. Diz-Moreno, J. M. Martinez, R. R. Pappalardo, and E. S. Marcos, *J. Am. Chem. Soc.* **120**, 10397 (1998).
- [179] P. Merkling, A. Munoz-Paez, J. M. Martinez, R. R. Pappalardo, and E. S. Marcos, *Phys. Rev. B* **64**, 12201 (2001).
- [180] P. Merkling, A. Munoz-Paez, and E. S. Marcos, *J. Am. Chem. Soc.* **124**, 10911 (2002).
- [181] J. M. Martinez, R. R. Pappalardo, E. S. Marcos, K. Refson, S. Diz-Moreno, and A. Munoz-Paez, *J. Phys. Chem. B* **102**, 3272 (1998).
- [182] J. M. Martinez, R. R. Pappalardo, and E. S. Marcos, *J. Am. Chem. Soc.* **121**, 3175 (1999).
- [183] C. Lee, W. Yang, and G. R. Parr, *Phys. Rev. B* **37**, 785 (1988).
- [184] T. W. Swaddle and M. K. S. Mak, *Can. J. Chem.* **61**, 473 (1983).
- [185] F. H. Spedding, P. F. Cullen, and A. Habenschuss, *J. Phys. Chem.* **78**, 1106 (1974).
- [186] D. Vanderbilt, *Phys. Rev. B* **41**, R7892 (1990).
- [187] M. C. Read and M. Sandström, *Acta Chem Scand.* **46**, 1177 (1992).
- [188] W. Bol and T. Welzen, *Chem. Phys. Lett.* **49**, 189 (1977).
- [189] R. Caminiti, G. Licheri, G. Piccagula, and G. Pinna, *J. Chem. Phys.* **69**, 1 (1978).
- [190] M. Magini, *J. Chem. Phys.* **73**, 2499 (1980).
- [191] R. D. Broadbent, G. W. Neilson, and M. Sanström, *J. Phys.: Condens. Matter* **4**, 639 (1992).
- [192] B. F. Melton and V. L. Pollak, *J. Chem. Phys.* **73**, 3669 (1969).

- [193] R. R. Pappalardo, J. M. Martinez, and E. S. Marcos, *J. Phys. Chem.* **100**, 11748 (1996).
- [194] J. M. Martinez, J. Hernandez-Cobos, R. R. Pappalardo, I. Ortega-Blake, and E. S. Marcos, *J. Chem. Phys.* **112**, 2339 (2000).
- [195] C. Kritayakornupong, K. Plankensteiner, and B. M. Rode, *J. Comp. Chem.* **25**, 1576 (2004).
- [196] J. M. Martinez, R. R. Pappalardo, and E. S. Marcos, *J. Chem. Phys.* **109**, 1445 (1998).
- [197] W. L. Earl, Ph.d. thesis, University of California, 1975.
- [198] A. D. Hugi, L. Helm, and A. E. Merbach, *Inorg. Chem.* **26**, 1763 (1987).
- [199] R. Golding and L. Stubbs, *J. Magn. Reson.* **33**, 627 (1979).
- [200] T. Ikeda, M. Hirata, and T. Kimura, *J. Chem. Phys.* **122**, 024510 (2005).
- [201] T. Ikeda, M. Hirata, and T. Kimura, *J. Chem. Phys.* **122**, 244507 (2005).
- [202] C. H. Pennington and V. A. Stenger, *Rev. Mod. Phys.* **68**, 855 (1996).
- [203] F. Gerson and W. Huber, *Electron Spin Resonance Spectroscopy of Organic Radicals* (Wiley-VCH, Weinheim, 2003).
- [204] J. W. Mintmire and C. T. White, *Appl. Phys. A* **67**, 65 (1998).
- [205] Y. Maeda, W. Wang, S.-Y. Xie, Y. Lin, K. A. S. Fernando, X. Wang, L. Qu, B. Chen, and Y.-P. Sun, *J. Am. Chem. Soc.* **127**, 10287 (2005).
- [206] X.-P. Tang, A. Kleinhammes, H. Shimoda, L. Fleming, K. Y. Bennoune, S. Sinha, C. Bower, O. Zhou, and Y. Wu, *Science* **288**, 492 (2000).
- [207] A. Kitaygorodskiy, W. Wang, S.-Y. Xie, Y. Lin, K. A. S. Fernando, X. Wang, L. Qu, B. Chen, and Y.-P. Sun, *J. Am. Chem. Soc.* **127**, 7517 (2005).
- [208] D. Loss and D. P. DiVincenzo, *Phys. Rev. A* **57**, 120 (1998).
- [209] B. E. Kane, *Nature* **393**, 133 (1998).

- [210] Z. H. Xiong, D. Wu, Z. V. Vardeny, and J. Shi, *Nature* **427**, 821 (2004).
- [211] S. D. Bader, *Rev. Mod. Phys.* **78**, 1 (2006).
- [212] S. Sahoo, T. Kontos, J. Furer, C. Hoffmann, M. Gräber, A. Cottet, and C. Schönenberger, *Nature Physics* **1**, 99 (2005).
- [213] S. Sahoo, T. Kontos, C. Schönenberger, and C. Sürgers, *Appl. Phys. Lett.* **86**, 112109 (2005).
- [214] M. Bockrath, W. Liang, D. Bozovic, J. H. Hafner, C. M. Lieber, M. Tinkham, and H. Park, *Science* **291**, 283 (2001).
- [215] M. R. Buitelaar, A. Bachtold, T. Nussbaumer, M. Iqbal, and C. Schönenberger, *Phys. Rev. Lett.* **88**, 156801 (2002).
- [216] Y. G. Semenov, K. W. Kim, and G. J. Iafrate, *cond-mat/0602425*.
- [217] A. V. Khaetskii, D. Loss, and L. Glazman, *Phys. Rev. Lett.* **88**, 186802 (2002).
- [218] J. M. Taylor, C. M. Marcus, and M. D. Lukin, *Phys. Rev. Lett.* **90**, 206803 (2003).
- [219] R. J. Epstein, F. M. Mendoza, Y. K. Kato, and D. D. Awschalom, *Nature Physics* **1**, 94 (2005).
- [220] L. Childress, M. V. G. Dutt, J. M. Taylor, A. S. Zibrov, F. Jelezko, J. Wrachtrup, P. R. Hemmer, and M. D. Lukin, *Science* **314**, 281 (2006).
- [221] W. D. Knight, *Phys. Rev. B* **76**, 1259 (1949).
- [222] S. Latil, L. Henrard, C. G. Bac, P. Bernier, and A. Rubio, *Phys. Rev. Lett.* **86**, 3160 (2001).
- [223] C. G. Bac, S. Latil, P. Laudinie, V. Jourdain, J. Conard, L. Duclaux, A. Rubio, and P. Bernier, *Carbon* **40**, 1825 (2002).
- [224] V. Jaccarino and Y. Yafet, *Phys. Rev.* **133**, A1630 (1964).
- [225] G. D. Gaspari, W.-M. Shyu, and T. P. Das, *Phys. Rev.* **134**, A852 (1964).
- [226] J. Conard, H. Estrade, P. Lauginie, H. Fuzellier, G. Furdin, and R. Vasse, *Physica B* **99**, 521 (1980).

- [227] M. Machón, S. Reich, C. Thomsen, D. Sánchez-Portal, and P. Ordejón, *Phys. Rev. B* **66**, 155410 (2002).
- [228] I. Cabria, J. W. Mintmire, and C. T. White, *Phys. Rev. B* **67**, 121406(R) (2003).
- [229] P. Delaney, H. J. Choi, J. Ihm, S. G. Louie, and M. L. Cohen, *Phys. Rev. B* **60**, 7899 (1999).
- [230] M. Ouyang, J.-L. Huang, C. L. Cheung, and C. M. Lieber, *Science* **292**, 702 (2001).
- [231] S. Reich, C. Thomsen, and P. Ordejón, *Phys. Rev. B* **65**, 155411 (2002).
- [232] S. Okada and A. Oshiyama, *Phys. Rev. Lett.* **91**, 216801 (2003).
- [233] J. Conard, M. G. le Brun, P. Lauginie, H. Estrade-Szwarckopf, and G. Hermann, *Synth. Met.* **2**, 227 (1980).
- [234] K. N. Kudin and G. E. Scuseria, *Phys. Rev. B* **61**, 16440 (2000).
- [235] M. Weinert and A. J. Freeman, *Phys. Rev. B* **28**, 6262 (1983).
- [236] C. Herring, in *Magnetism*, edited by G. T. Rado and h. Suhl (Academic, New York, 1966), Vol. 4, pp. 273–297.
- [237] P. J. Hay and T. H. Dunning Jr., in *Modern Theoretical Chemistry*, edited by H. F. Schaefer III (Plenum, New York, 1976), Vol. 3, pp. 1–28.
- [238] O. V. Yazyev and L. Helm, *Phys. Rev. B* **72**, 245416 (2005).
- [239] D. M. Chipman, *Theor. Chim. Acta* **82**, 93 (1992).
- [240] O. Jepsen and O. K. Andersen, *Solid State Commun.* **9**, 1763 (1971).
- [241] P. E. Blöchl, O. Jepsen, and O. K. Andersen, *Phys. Rev. B* **49**, 16223 (1994).
- [242] O. V. Yazyev, K. N. Kudin, and G. E. Scuseria, *Phys. Rev. B* **65**, 205117 (2002).
- [243] O. V. Yazyev, E. N. Brothers, K. N. Kudin, and G. E. Scuseria, *J. Chem. Phys.* **121**, 2466 (2004).
- [244] J. T. Frey and D. J. Doren, TUBEGEN 3.1, 2003.

- [245] O. Gülseren, T. Yildirim, and S. Ciraci, *Phys. Rev. B* **65**, 153405 (2002).
- [246] C. L. Kane and E. J. Mele, *Phys. Rev. Lett.* **78**, 1932 (1997).
- [247] R. C. Haddon, *J. Am. Chem. Soc.* **108**, 2837 (1986).
- [248] E. T. Mickelson, C. B. Huffman, A. G. Rinzler, R. E. Smalley, R. H. Hauge, and J. L. Margrave, *Chem. Phys. Lett.* **296**, 188 (1998).
- [249] H. F. Bettinger, K. N. Kudin, and G. E. Scuseria, *J. Am. Chem. Soc.* **123**, 12849 (2001).
- [250] M. Karplus and G. K. Fraenkel, *J. Chem. Phys.* **35**, 1312 (1961).
- [251] N. Rega, M. Cossi, and V. Barone, *J. Chem. Phys.* **105**, 11060 (1996).
- [252] L. Hermosilla, P. Calle, J. M. García de la Vega, and C. Sieiro, *J. Phys. Chem. A* **109**, 1114 (2005).
- [253] J. R. Bolton and G. K. Fraenkel, *J. Chem. Phys.* **40**, 3307 (1964).
- [254] D. J. M. Fassaert and E. de Boer, *Recl. Trav. Chim. Pays-Bas* **91**, 273 (1972).
- [255] R. F. Claridge, C. M. Kirk, and B. M. Peake, *Aust. J. Chem.* **26**, 2055 (1973).
- [256] K. Nakada, M. Fujita, G. Dresselhaus, and M. S. Dresselhaus, *Phys. Rev. B* **54**, 17954 (1996).
- [257] H. Overhof and U. Gerstmann, *Phys. Rev. Lett.* **92**, 087602 (2004).
- [258] K. Kelly and N. Halas, *Surf. Sci.* **416**, L1085 (1998).
- [259] O. V. Yazyev and L. Helm, *Phys. Rev. B* **75**, 125408 (2007).
- [260] Y. Kobayashi, K.-i. Fukui, T. Enoki, and K. Kusakabe, *Phys. Rev. B* **73**, 125415 (2006).
- [261] *Carbon-Based Magnetism: An Overview of Metal Free Carbon-Based Compounds and Materials*, edited by T. Makarova and F. Palacio (Elsevier, Amsterdam, 2005).
- [262] J. M. D. Coey, M. Venkatesan, C. B. Fitzgerald, A. P. Douvalis, and I. S. Sanders, *Nature* **420**, 156 (2002).

- [263] S. Okada and A. Ohiyama, Phys. Rev. Lett. **87**, 146803 (2001).
- [264] H. Lee, Y.-W. Son, N. Park, S. Han, and J. Yu, Phys. Rev. B **72**, 174431 (2005).
- [265] Y.-H. Kim, J. Choi, K. J. Chang, and D. Tománek, Phys. Rev. B **68**, 125420 (2003).
- [266] P. Lehtinen, A. S. Foster, Y. Ma, A. Krasheninnikov, and R. M. Nieminen, Phys. Rev. Lett. **93**, 187202 (2004).
- [267] J.-C. Charlier, Acc. Chem. Res. **35**, 1063 (2002).
- [268] P. Ruffieux, O. Gröning, P. Schwaller, L. Schlapbach, and P. Gröning, Phys. Rev. Lett. **84**, 4910 (2000).
- [269] F. Banhart, Rep. Prog. Phys. **62**, 1181 (1999).
- [270] C. Mikó, M. Milas, J. W. Seo, E. Couteau, N. Barisic, R. Gaál, and L. Forró, Appl. Phys. Lett. **83**, 4622 (2003).
- [271] J. H. W. Simmons, *Radiation Damage in Graphite* (Pergamon, London, 1965).
- [272] R. H. Telling, C. P. Ewels, A. A. El-Barbary, and M. I. Heggie, Nat. Mater. **2**, 333 (2003).
- [273] F. Banhart, J. Appl. Phys. **81**, 3440 (1997).
- [274] M. Terrones, H. Terrones, F. Banhart, J.-C. Charlier, and P. M. Ajayan, Science **288**, 1226 (2000).
- [275] J. Cummings and A. Zettl, Science **289**, 602 (2000).
- [276] A. M. Fennimore, T. D. Yuzvinsky, W. Q. Han, M. S. Fuhrer, J. Cumings, and A. Zettl, Nature **424**, 408 (2003).
- [277] K. Jensen, c. Girit, W. Mickelson, and A. Zettl, Phys. Rev. Lett. **96**, 215503 (2006).
- [278] A. Kis, K. Jensen, S. Aloni, W. Mickelson, and A. Zettl, Phys. Rev. Lett. **97**, 025501 (2006).
- [279] H. A. Mizes and J. S. Foster, Science **244**, 559 (1989).

- [280] P. Ruffieux, M. Melle-Franco, O. Gröning, M. Biemann, F. Zerbetto, and P. Gröning, *Phys. Rev. B* **71**, 153403 (2005).
- [281] V. M. Pereira, F. Guinea, J. M. B. Lopes dos Santos, N. M. R. Peres, and A. H. C. Neto, *Phys. Rev. Lett.* **96**, 036801 (2006).
- [282] D. M. Edwards and M. I. Katsnelson, *J. Phys.: Condens. Matter* **18**, 7209 (2006).
- [283] M. A. Rudermann and C. Kittel, *Phys. Rev.* **96**, 99 (1954).
- [284] T. Kasuya, *Progr. Theor. Phys. (Japan)* **16**, 45 (1965).
- [285] K. Yoshida, *Phys. Rev.* **106**, 106 (1958).
- [286] M. A. H. Vozmediano, M. P. López-Sancho, T. Stauber, and F. Guinea, *Phys. Rev. B* **72**, 155121 (2005).
- [287] J. M. Soler, E. Artacho, J. D. Gale, A. García, J. Junquera, P. Ordejón, and D. Sánchez-Portal, *J. Phys.: Condens. Matter* **14**, 2745 (2002).
- [288] H. J. Monkhorst and J. D. Pack, *Phys. Rev. B* **16**, 5188 (1976).
- [289] P. Ruffieux, O. Gröning, M. Biemann, P. Mauron, L. Schlapbach, and P. Gröning, *Phys. Rev. B* **66**, 245416 (2002).
- [290] E. J. Duplock, M. Scheffler, and P. J. D. Lindan, *Phys. Rev. Lett.* **92**, 225502 (2004).
- [291] A. J. Lu and B. C. Pan, *Phys. Rev. Lett.* **92**, 105504 (2004).
- [292] P. Mohn, *Magnetism in the solid state* (Springer-Verlag, Berlin Heidelberg, 2003).
- [293] H. Thomann, L. R. Dalton, Y. Tomkiewicz, N. S. Shiren, and T. C. Clarke, *Phys. Rev. Lett.* **50**, 533 (1983).
- [294] B. Kirtman, M. Hasan, and D. M. Chipman, *J. Chem. Phys.* **95**, 7698 (1991).
- [295] S. Garaj, L. Thien-Nga, R. Gaal, L. Forró, K. Takahashi, F. Kokai, M. Yudasaka, and S. Iijima, *Phys. Rev. B* **62**, 17115 (2000).
- [296] H. Imai, P. K. Babu, E. Oldfield, A. Wieckowski, D. Kasuya, T. Azami, Y. Shimakawa, M. Yudasaka, Y. Kubo, and S. Iijima, *Phys. Rev. B* **73**, 125405 (2006).

-
- [297] C. P. Ewels, R. H. Telling, A. A. El-Barbary, M. I. Heggie, and P. R. Briddon, *Phys. Rev. Lett.* **91**, 025505 (2003).
- [298] A. J. Stone and D. J. Wales, *Chem. Phys. Lett.* **128**, 501 (1986).
- [299] E. Kaxiras and K. C. Pandey, *Phys. Rev. Lett.* **61**, 2693 (1988).
- [300] K. Nordlund, J. Keinonen, and T. Mattila, *Phys. Rev. Lett.* **77**, 699 (1996).
- [301] V. H. Crespi, N. G. Chopra, M. L. Cohen, A. Zettl, and S. G. Louie, *Phys. Rev. B* **54**, 5927 (1996).
- [302] P. M. Ajayan, V. Ravikumar, and J.-C. Charlier, *Phys. Rev. Lett.* **81**, 1437 (1998).
- [303] A. V. Krasheninnikov, F. Banhart, J. X. Li, A. S. Foster, and R. M. Nieminen, *Phys. Rev. B* **72**, 125428 (2005).
- [304] M. Hanfland, H. Beister, and K. Syassen, *Phys. Rev. B* **39**, 12598 (1989).
- [305] O. Gunnarsson and B. I. Lundquist, *Phys. Rev. B* **13**, 4279 (1976).
- [306] S. Nosé, *J. Chem. Phys.* **81**, 511 (1984).
- [307] C. G. Van de Walle and J. Neugebauer, *J. Appl. Phys.* **95**, 3851 (2004).
- [308] L. Li, S. Reich, and J. Robertson, *Phys. Rev. B* **72**, 184109 (2005).
- [309] Y. Ma, A. S. Foster, A. V. Krasheninnikov, and R. M. Nieminen, *Phys. Rev. B* **72**, 205416 (2005).
- [310] K. B. Wiberg, W. P. Dailey, F. H. Walker, S. T. Waddell, L. S. Cracker, and M. Newton, *J. Am. Chem. Soc.* **107**, 7241 (1985).
- [311] P. Lehtinen, A. S. Foster, A. Ayuela, A. Krasheninnikov, K. Nordlund, and R. M. Nieminen, *Phys. Rev. Lett.* **91**, 017202 (2003).
- [312] C. H. Xu, C. L. Fu, and D. F. Pedraza, *Phys. Rev. B* **48**, 13273 (1993).
- [313] B. W. Smith and D. E. Luzzi, *J. Appl. Phys.* **90**, 3509 (2001).
- [314] A. J. R. da Silva, A. Fazzio, and A. Antonelli, *Nano Lett.* **5**, 1045 (2005).

- [315] V. H. Crespi, M. L. Cohen, and A. Rubio, *Phys. Rev. Lett.* **79**, 2093 (1997).
- [316] B. Sitharaman, K. R. Kissell, K. B. Hartman, L. A. Tran, A. Baikalov, I. Rusakova, Y. Sun, H. A. Khant, S. J. Ludtke, W. Chiu, S. Laus, E. Toth, L. Helm, A. E. Merbach, and L. J. Wilson, *Chem. Commun.* **2005**, 3915 (2005).
- [317] F. J. Himpsel, B. S. Meyerson, F. R. McFeely, J. F. Morar, A. Taleb-Ibrahimi, and J. A. Yarmoff, in *Proceedings of the International School of Physics Enrico Fermi*, edited by M. Campagna and R. Rosei (Elsevier, Amsterdam, 1990), pp. 203–236.
- [318] Y. Tu and J. Tersoff, *Phys. Rev. Lett.* **84**, 4393 (2000).
- [319] H. Koh, J. W. Kim, W. H. Choi, and H. W. Yeom, *Phys. Rev. B* **67**, 073306 (2003).
- [320] S. Dreiner, M. Schürmann, M. Krause, U. Berges, and C. Westphal, *J. Electron Spectrosc. Relat. Phenom.* **144-147**, 405 (2005).
- [321] E. Landemark, C. J. Karlsson, Y.-C. Chao, and R. I. G. Uhrberg, *Phys. Rev. Lett.* **69**, 1588 (1992).
- [322] P. De Padova, R. Larciprete, C. Quaresima, C. Ottaviani, B. Ressel, and P. Perfetti, *Phys. Rev. Lett.* **81**, 2320 (1998).
- [323] T.-W. Pi, C.-P. Cheng, and I.-H. Hong, *Surf. Sci.* **418**, 113 (1998).
- [324] E. Pehlke and M. Scheffler, *Phys. Rev. Lett.* **71**, 2338 (1993).
- [325] G. Jayaram, P. Xu, and L. D. Marks, *Phys. Rev. Lett.* **71**, 3489 (1993).
- [326] E. L. Bullock, R. Gunnella, L. Patthey, T. Abukawa, S. Kono, C. R. Natoli, and L. S. O. Johansson, *Phys. Rev. Lett.* **74**, 2756 (1995).
- [327] J. E. Northrup, *Phys. Rev. B* **47**, 10032 (1993).
- [328] A. Bongiorno, A. Pasquarello, M. S. Hybertsen, and L. Feldman, *Phys. Rev. Lett.* **90**, 186101 (2003).
- [329] S. Dreiner, M. Schürmann, and C. Westphal, *Phys. Rev. Lett.* **93**, 126101 (2004).
- [330] A. Bongiorno and A. Pasquarello, *Phys. Rev. Lett.* **94**, 189601 (2005).

-
- [331] S. Dreiner, M. Schürmann, and C. Westphal, Phys. Rev. Lett. **94**, 189602 (2005).
- [332] F. J. Himpsel, F. R. McFeely, A. Taleb-Ibrahimi, J. A. Yarmoff, , and G. Hollinger, Phys. Rev. B **38**, 6084 (1988).
- [333] A. Pasquarello, M. S. Hybertsen, and R. Car, Phys. Rev. Lett. **64**, 1024 (1995).
- [334] F. Jolly, F. Rochet, G. Dufour, C. Grupp, and A. Taleb-Ibrahimi, J. Non-Cryst. Solids **280**, 150 (2001).
- [335] J. H. Oh, H. W. Yeom, Y. Hagimoto, K. Ono, M. Oshima, N. Hirashita, M. Nywa, and A. Toriumi, Phys. Rev. B **63**, 205310 (2001).
- [336] N. Marzari and D. Vanderbilt, Phys. Rev. B **56**, 12847 (1997).
- [337] A. Pasquarello, M. S. Hybertsen, and R. Car, Phys. Rev. B **53**, 10942 (1996).
- [338] D. R. Hamann and D. A. Muller, Phys. Rev. Lett. **89**, 126404 (2002).
- [339] B. Richter, H. Kuhlenbeck, H.-J. Freund, and P. S. Bagus, Phys. Rev. Lett. **93**, 026805 (2004).
- [340] J.-H. Cho, M.-H. Kang, and K. Terakura, Phys. Rev. B **55**, 15464 (1997).
- [341] E. T. Yu, E. T. Croke, T. C. McGill, and R. H. Miles, Appl. Phys. Lett. **56**, 569 (1990).
- [342] L. D. Laude, F. H. Pollak, and M. Cardona, Phys. Rev. B **3**, 2623 (1971).
- [343] J. A. Pople and M. Gordon, J. Am. Chem. Soc. **89**, 4253 (1967).

CURRICULUM VITAE

Oleg YAZYEV

Date of Birth: January 15, 1981 in Simferopol, Ukraine

Nationality: Ukrainian (Swiss permit B)

Marital Status: Married

2003–2007 Ph.D. in Chemistry and Chemical Engineering,
Ecole Polytechnique Fédérale de Lausanne (EPFL), Switzerland

2002–2003 Software Engineer, Advanced Chemistry Development Inc.,
Moscow R&D Department, Moscow, Russian Federation

2001, 2002 Summer Research Associate, Rice University,
Chemistry Department, Houston, United States

1998–2003 Diploma in Chemistry (*cum laude*), Moscow State University,
Chemistry Department, Moscow, Russian Federation

Languages: english, french, russian, ukrainian

Awards: George Soros Foundation Fellow, 1999-2002
Silver Medal, XXX International Chemistry Olympiad (Melbourne, 1998)
Silver Medal, XXIX International Chemistry Olympiad (Montreal, 1997)

PUBLICATIONS*

20. O. V. Yazyev and L. Helm, *Carbon nanotubes spin-polarized by magnetic impurities, in preparation*
19. † O. V. Yazyev, *Hyperfine interactions in graphene and related carbon nanostructures, submitted*
18. † O. V. Yazyev and L. Helm, *Gadolinium(III) ion in liquid water: structure, dynamics and magnetic interactions from first principles, submitted*
17. A. Mourachkine, O. V. Yazyev, and J.-P. Ansermet, *The smallest spintronics nano-oscillator functioning in zero applied magnetic field, submitted*
16. † O. V. Yazyev, I. Tavernelli, U. Röthlisberger and L. Helm, *Early stages of radiation damage of graphite and carbon nanostructures: A first-principles molecular dynamics study*, Phys. Rev. B **75**, 115418/1-5 (2007)
15. † O. V. Yazyev and L. Helm, *Defect-induced magnetism in graphene*, Phys. Rev. B **75**, 125408/1-5 (2007)
14. † O. V. Yazyev and L. Helm, *^{17}O nuclear quadrupole coupling constants of water bound to a metal ion: a gadolinium(III) case study*, J. Chem. Phys. **125**, 054503/1-8 (2006)
13. † O. V. Yazyev and A. Pasquarello, *Origin of fine structure in Si 2p photoelectron spectra at silicon surfaces and interfaces*, Phys. Rev. Lett. **96**, 157601/1-4 (2006)
12. † O. V. Yazyev and L. Helm, *Magnetism induced by single-atom defects in nanographites*, Proceedings of the International Conference on Nanoscience and Technology, Basel, 2006, J. Phys.: Conf. Series, *in press*
11. † O. V. Yazyev and A. Pasquarello, *Core-Level Photoelectron spectroscopy probing local strain at silicon surfaces and interfaces, to appear in the Proceedings of the 28th International Conference on the Physics of Semiconductors, Vienna, 2006*

*Including 1 manuscript in preparation, 2 conference proceedings and a citable computer code references.

†Publications related to the thesis.

-
10. † O. V. Yazyev and L. Helm, *Hyperfine interactions in aqueous solution of Cr^{3+} : an ab initio molecular dynamics study*, Theor. Chem. Acc. **115**, 190-195 (2006)
 9. P. V. Grundler, O. V. Yazyev, N. Aebischer, L. Helm, G. Laurency and A. E. Merbach, *Kinetic studies on the first dihydrogen aquacomplex, $[\text{Ru}(\text{H}_2)(\text{H}_2\text{O})_5]^{2+}$: Formation under H_2 pressure and catalytic H/D isotope exchange in water*, Inorg. Chim. Acta. **259**, 1795-1806 (2006)
 8. † O. V. Yazyev and L. Helm, *Isotropic Knight shift of metallic carbon nanotubes*, Phys. Rev. B **72**, 245416/1-5 (2005)
 7. † O. V. Yazyev, L. Helm, V. G. Malkin, and O. L. Malkina, *Quantum chemical investigation of hyperfine coupling constants on first coordination sphere water molecule of Gd(III) aquacomplexes*, J. Phys. Chem. A **109**, 10997-11005 (2005)
 6. † O. V. Yazyev, I. Tavernelli, L. Helm, and U. Röthlisberger, *Core spin-polarization correction in pseudopotential-based electronic structure calculations*, Phys. Rev. B **71**, 115110/1-5 (2005)
 5. O. V. Yazyev, E. N. Brothers, K. N. Kudin, and G. E. Scuseria, *A finite temperature linear tetrahedron method for electronic structure calculations of periodic systems*, J. Chem. Phys. **121**, 2466-2470 (2004)
 4. Gaussian 03, Revision C.02, M. J. Frisch, G. W. Trucks, H. B. Schlegel, G. E. Scuseria, M. A. Robb, J. R. Cheeseman, J. A. Montgomery, Jr., T. Vreven, K. N. Kudin, J. C. Burant, J. M. Millam, S. S. Iyengar, J. Tomasi, V. Barone, B. Mennucci, M. Cossi, G. Scalmani, N. Rega, G. A. Petersson, H. Nakatsuji, M. Hada, M. Ehara, K. Toyota, R. Fukuda, J. Hasegawa, M. Ishida, T. Nakajima, Y. Honda, O. Kitao, H. Nakai, M. Klene, X. Li, J. E. Knox, H. P. Hratchian, J. B. Cross, V. Bakken, C. Adamo, J. Jaramillo, R. Gomperts, R. E. Stratmann, O. Yazyev, A. J. Austin, R. Cammi, C. Pomelli, J. W. Ochterski, P. Y. Ayala, K. Morokuma, G. A. Voth, P. Salvador, J. J. Dannenberg, V. G. Zakrzewski, S. Dapprich, A. D. Daniels, M. C. Strain, O. Farkas, D. K. Malick, A. D. Rabuck, K. Raghavachari, J. B. Foresman, J. V. Ortiz, Q. Cui, A. G. Baboul, S. Clifford, J. Cioslowski, B. B. Stefanov, G. Liu, A. Liashenko, P. Piskorz, I. Komaromi, R. L. Martin, D. J. Fox, T. Keith, M. A. Al-Laham, C. Y. Peng, A. Nanayakkara, M.

Challacombe, P. M. W. Gill, B. Johnson, W. Chen, M. W. Wong, C. Gonzalez, and J. A. Pople, Gaussian, Inc., Wallingford CT, 2004

3. O. V. Yazyev, K. N. Kudin, and G. E. Scuseria, *Efficient algorithm for band connectivity resolution*, Phys. Rev. B **65**, 205117/1-8 (2002)
2. A. Yu. Chernyadyev, Yu. A. Ustynyuk, O. V. Yazyev, E. A. Kataev, M. D. Reshetova, A. A. Sidorov, G. G. Aleksandrov, V. N. Ikorskii, V. M. Novotortsev, S. E. Nefedov, I. L. Eremenko, and I. I. Moiseev, *Binuclear and polynuclear transition metal complexes with macrocyclic ligands 1. Synthesis and the structure of an antiferromagnetic binuclear nickel complex prepared by the reaction of o-phenylenediamine with pyrrole-2,5-dicarbaldehyde and nickel pivalate*, Russ. Chem. Bull., Int. Ed **50**, 2445-2450 (2001)
1. O. V. Yazyev and Yu. A. Ustynyuk, *Theoretical investigation of structure and properties of tetraaminoethylene by ab initio and density functional theory methods*, Moscow University Chemistry Bulletin **41**, 315-318 (2000)